

High-resolution 3D direct-write prototyping for healthcare applications

A thesis submitted for the degree of
Doctor of Philosophy
at University College London (UCL)

Saja Aabith
Department of Mechanical Engineering
University College London
Torrington Place, London WC1E 7JE

October 2019

Declaration

I, Saja Aabith confirm that the work presented in this thesis is my own and an editor has also not been used. Where information has been derived from other sources, I confirm that this has been indicated in the thesis.

Saja Aabith

Date: 15/10/2019

Abstract

The healthcare sector has much to benefit from the vast array of novelties erupting from the manufacturing world. 3D printing (additive manufacturing) is amongst the most promising recent inventions with much research concentrated around the various approaches of 3D printing and applying this effectively in the health sector. Amongst these methods, the direct-write assembly approach is a promising candidate for rapid prototyping and manufacturing of miniaturised medical devices/sensors and in particular, miniaturised flexible capacitive pressure sensors. Microstructuring the dielectric medium of capacitive pressure sensors enhances the sensitivity of the capacitive pressure sensor. The structuring has been predominantly achieved with photolithography and similar subtractive approaches.

In this project high-resolution 3D direct write printing was used to fabricate structured dielectric mediums for capacitive pressure sensors. This involved the development and rheological characterisation of printability-tuned water soluble polyvinyl pyrrolidone (PVP) based inks (10%-30% polymer content) for stable high-resolution 3D printing. These inks were used to print water soluble micromoulds that were filled and cured with otherwise difficult to structure low G' materials like PDMS. Our approach essentially decouples ink synthesis from printability at the micrometre scale.

The developed micro moulding approach was employed for printing pyramidal micro moulds, that were used as templates for fabricating pyramid structured dielectric mediums for capacitive pressure sensing. The power of the approach was used to alter the microstructures and reap enhanced pressure sensing characteristics for effective miniaturised capacitive pressure sensors. A pressure sensing ring – that could be worn by doctors and surgeons – was

prototyped with our approach and employed successfully to monitor in real-time the radial pulse signal of a 29 year old male volunteer. The print resolution of the inks was enhanced by formulating and rheologically characterising a PVP/PVDF polymer blend ink that would wet the printing nozzle less due to the hydrophobicity of the PVDF.

Research Impact Statement

1. The thesis will capture the interest of a broad scientific community working on micrometre scale (high-resolution) manufacturing, since it helps avoid the need for cleanroom based lithographic techniques that are common in soft lithography based prototyping of silicones.
2. The systematic investigation of our developed PVP ink and the viscoelastic properties of it will serve as a guide for other ink formulations (e.g. solvent based inks).
3. Our developed approach of rationally micromoulding dielectric mediums via direct-write printing for enhanced capacitive pressure sensing has opened up the door to further investigate and structure-to-control the dielectric medium of capacitive pressure sensors.
4. Additionally, our developed fabrication approach of water soluble micromoulds is more environmentally friendly than fabricating via photolithography, which has been the main go to fabrication approach for microstructured capacitive pressure sensors.
5. Our developed device, the pressure sensing ring, will be further enhanced by adding wireless readout capabilities to it. So that it can be worn by doctors and surgeons.
6. Future work that can be built up from this work includes significant benefit for the medical, microelectronics and microfluidics sector.
7. A book chapter has been published and a paper has been submitted to the Additive Manufacturing journal (Elsevier).

Contents

PUBLICATIONS	10
ACKNOWLEDGEMENTS.....	11
NOMENCLATURE.....	12
LIST OF FIGURES.....	13
CHAPTER 1 - INTRODUCTION	20
1.1 BACKGROUND.....	20
1.2 THE INTERNET OF THINGS (IoT).....	21
1.3 MINIATURISED DEVICES	22
1.4 ENHANCED CAPACITIVE PRESSURE SENSING	23
1.5 ADDITIVE MANUFACTURING	25
1.6 AIMS AND OBJECTIVES.....	26
CHAPTER 2 – HEALTHCARE DEVICES THAT ARE FLEXIBLE.....	28
2.1 INTRODUCTION	28
2.2 FLEXIBLE SENSORS	37
2.3 FLEXIBLE PRESSURE SENSORS	39
2.3.1 <i>Fundamentals</i>	39
2.3.2 <i>Piezoresistive sensing</i>	41
2.3.3 <i>Piezoelectric and triboelectric pressure sensing</i>	44
2.4 CAPACITIVE PRESSURE SENSORS	47
2.4.1 <i>Fundamentals</i>	47
2.4.2 <i>Nanoparticles dispersed dielectric</i>	50
2.4.3 <i>Porous dielectric</i>	51
2.4.4 <i>Structured dielectric</i>	54
2.5 METHODS OF MANUFACTURE	66

2.5.1 Photolithography.....	66
2.5.2 3D printing.....	67
CHAPTER 3 - HIGH-RESOLUTION 3D PRINTING.....	68
3.1 ADDITIVE INSTEAD OF SUBTRACTIVE MANUFACTURING.....	68
3.2 FORMS OF HIGH-RESOLUTION 3D PRINTING	68
3.2.1 3D direct laser writing	68
3.2.2 Focused ion beam.....	69
3.2.3 Direct-write printing.....	71
3.3 INK PROPERTIES.....	73
CHAPTER 4 - EXPERIMENTAL METHODS	75
4.1 DIRECT-WRITE ASSEMBLY FOR HIGH-RESOLUTION PRINTING	76
4.1.1 Nozzle fabrication.....	76
4.1.2 Direct-write printing.....	78
4.2 CAPACITIVE PRESSURE SENSING.....	81
4.2.1 PCB design & Cjig.....	81
4.2.2 Measurement setup	82
CHAPTER 5 – DECOUPLING PRINTABILITY FROM INK SYNTHESIS FOR RAPID PROTOTYPING.....	84
5.1 EXPERIMENTAL PROCEDURE	84
5.1.1 Polyvinylpyrrolidone (PVP) ink.....	84
5.1.2 Polydimethylsiloxane (PDMS) and EcoFlex inks	85
5.1.3 Dispersing carbon black in PDMS	86
5.1.4 Rheological studies of PVP	87
5.1.5 Mould printing.....	88
5.2 RESULTS & DISCUSSIONS	90
5.2.1 Rheology of PVP	90
5.2.2 Printability of PVP.....	94

5.2.3 Mouldings.....	95
5.3 CONCLUSIONS.....	96
CHAPTER 6 – MICRO MOULDING APPROACH FOR MICROSTRUCTURED CAPACITIVE PRESSURE SENSORS.....	98
6.1 EXPERIMENTAL PROCEDURE	98
6.1.1 Arrays as printed moulds.....	98
6.1.2 Rectangular based pyramid micro mould printing.....	102
6.1.3 Filling the entire micro mould simultaneously using vacuum	105
6.2 RESULTS & DISCUSSIONS	111
6.2.1 Structured dielectric	111
6.2.2 Enhancement of base capacitance via carbon black nanoparticles.....	112
6.2.3 Higher structures for a bigger sensing range	116
6.2.4 Increased electrode area for enhanced sensitivity.....	117
6.2.5 Response and relaxation time	121
6.2.6 A pressure sensing ring.....	125
6.2.7 Change in dimensions from mould to moulding	128
6.3 CONCLUSIONS.....	130
CHAPTER 7 - IMPROVING PRINT RESOLUTION	133
7.1 EXPERIMENTAL PROCEDURE	133
7.1.1 Silver nanoparticle ink	133
7.1.2 PVP/PVDF ink.....	134
7.2 RESULTS & DISCUSSIONS	134
7.2.1 Nozzle functionalisation	134
7.2.2 Rheology of PVP/PVDF blend	138
7.2.3 Exemplar prints	141
7.2.4 Array printing	143

7.3 CONCLUSIONS.....	144
CHAPTER 8 – SUMMARY OF ACHIEVEMENTS & FUTURE WORK.....	146
8.1 SUMMARY OF ACHIEVEMENTS	146
8.1.1 Decoupling printability from ink synthesis for rapid prototyping	146
8.1.2 Micro moulding approach for microstructured capacitive pressure sensors	147
8.1.3 Improving print resolution.....	148
8.2 FUTURE WORK	148
8.2.1 Moulding flexible interconnects and microfluidic channels	148
8.2.2 Improving carbon black nanoparticle dispersion in elastomer matrix.....	149
8.2.3 Effect of altering carbon black nanoparticle concentration.....	150
8.2.4 Inter-pyramid material.....	150
8.2.5 Going wireless with the pressure sensing ring	151
8.2.6 Simulating micropyramid deformation	152
8.2.7 Filling micro moulds with different elastomers.....	153
8.2.8 Varying sidewall angle of the pyramids	153
8.2.9 Imaging the micropyramids during deformation	154
8.2.10 Dynamic studies of the developed capacitive pressure sensors.....	154
APPENDIX	155
REFERENCES.....	162

Publications

Feihuang Fang and Saja Aabith, Shervanthi Homer-Vanniasinkam, Manish K. Tiwari, 'High-resolution 3D printing for healthcare underpinned by small-scale fluidics', 3D Printing in Medicine, Elsevier, 2017

Saja Aabith, Richard Caulfield, Anastasia Papadopoulou, Shervanthi Homer-Vanniasinkam, Manish K. Tiwari, '3D direct-write printing of safe, water soluble micro moulds for precision rapid prototyping' (Submitted to Additive Manufacturing journal, Elsevier)

Acknowledgements

Firstly, I praise and thank the Lord of the universe, who has given humans the ability to explore and understand some of His majestic design.

I am grateful to my parents for guiding me and looking after me throughout my life. I am also grateful to my wife and her continuous support throughout this journey.

I would like to thank both my supervisors Prof. Manish K. Tiwari and Prof. Shervanthi Homer-Vanniasinkam for taking me under their wings and giving me this opportunity to pursue a PhD under two esteemed academics.

I would like to thank the Nanoengineered Systems Lab members for giving me great companionship and good times. I would also like to thank the Mechanical Engineering Workshop and its ever helpful team and also the electronic and electrical engineering teaching lab team for their help and advice.

Nomenclature

C	Capacitance
AM	Additive Manufacturing
CB	Carbon black
Cjig	Capacitor jig
Da	Dalton
DMF	N,N-Dimethylformamide
D-pattern	Diamond pattern
ϵ_0	Dielectric constant of free space
ϵ_r	Relative dielectric constant of medium
G'	Storage modulus
G''	Loss modulus
PDMS	Polydimethylsiloxane
PVDF	Poly(vinylidene fluoride)
PVP	Polyvinylpyrrolidone
rpm	revolutions per minute
RT	Room temperature
SDA	Semiconductor Device Analyzer
SEM	Scanning electron microscopy
WEISS	Wellcome/EPSRC Centre for Interventional and Surgical Sciences
wt	weight

List of Figures

- Figure 1.1: Overview of the general trend of development in enhanced flexible capacitive pressure sensors
- Figure 2.1: The Samsung Galaxy Fold is a foldable phone (Samsung, 2019)
- Figure 2.2: Graphene nanosensor a.) Biotransfer of graphene nanosensor onto the surface (enamel) of the tooth b.) Schematic of the graphene nanosensor with illustration of wireless readout c.) Schematic showing binding of pathogenic bacteria by peptides self-assembled on the graphene biosensor d.) electrical resistance (upper) and fluorescence (lower) data recorded simultaneously versus time showing binding/unbinding of a single E.coli bacterium on a bare graphene nanosensor, images are $12\ \mu\text{m} \times 12\ \mu\text{m}$ e.) data recorded simultaneously versus time showing binding of a single E.coli bacterium on a peptide-functionalised graphene nanosensor, images are $20\ \mu\text{m} \times 20\ \mu\text{m}$ (Mannoor et al., 2012)
- Figure 2.3: Wearable textile battery a.) Photograph and schematic of a watch with a wearable textile battery strap. (Left) 6 LEDs (1 yellow=42 mW, 1 blue=62 mW & 4 whites=62 mW) were lit up as a demonstration of a functioning watchstrap battery b.) Schematic of woven battery electrode yarns, where each yarn consisting of multiple strands is coated with nickel and a battery composite c.) Schematic comparing the electrode based on a standard flat metal foil and the textile battery electrode is based on the woven yarn during repeated folding tests (Lee et al., 2013)
- Figure 2.4: Self-healable and multifunctional e-tattoo a.) Schematic illustration of the Gr/SF/Ca²⁺ E-tattoo b.) Relative resistance changes of ECG response, image shows the corresponding enlargement of a single signal waveform c.) Temperature response performance d.) Relative resistance change of humidity response of (inset) moustache tattoo attached directly beneath the nose to monitor respiration e.) Schematic illustrations showing a visible fracture and healing process of the LED circuit interconnected with a Gr/SF/Ca²⁺ film f.) Electrical measurements of the films during five cutting and healing cycles and the zoomed image shows that the film heals within 0.3 s (Qi Wang et al., 2019)
- Figure 2.5: Electrotactile finger glove (Ying et al., 2012) and steerable cannula robots (Wei and Simaan, 2012) a.) Electrotactile array on freestanding finger tube b.) Voltage needed for electrotactile sensation as a function of stimulation frequency, image shows electrotactile array on a human finger during the experiment c.) Resistance change of a representative gauge during bending cycles (black) and side to side motion (red), images of strain gauge array on a finger-tube mounted on thumb in (I) straight and (II) bent positions d.) Illustration of flexible surgical tool and its setup e.) experimental image for microstent delivery in an agar-based artificial blood vessel channel model
- Figure 2.6: A flexible gas sensor – Nanowire on a plastic gas sensor for detecting environmental pollutants (Mcalpine et al., 2007)
- Figure 2.7: Example of sensor performance indicators a.) schematic of a capacitive pressure sensor based on a silver nanowires embedded PDMS with a microarray structure b.) relative capacitance change over a pressure range of 0-6.7 kPa with a sensitivity of $2.94 \pm 0.25\ \text{kPa}^{-1}$ and $0.75 \pm 0.06\ \text{kPa}^{-1}$ for pressure ranges 0 to 2 kPa and 2 kPa to 6.7 kPa respectively c.) sensor response time and relaxation time d.) sensor response stability for a repeated compression test for 1000 cycles (Shuai et al., 2017a)
- Figure 2.8: Piezoresistive sensors and their stability tests (a) Schematic illustration of the fabrication steps of the MXene nanosheets based flexible pressure sensor (b) Relative current change as a function of applied pressure (c) Durability test by applying a pressure of 3036 Pa repeatedly (Ying Guo et al., 2019) (d) Photograph of a nanoporous polymer composite, inset shows the side of the specimen in bent form and the zoomed image shows a schematic of the nanoscale pore with exposed carbon nanotubes (e) compressive stress-strain curves of the nanoporous polymer composites with increasing volume fraction of added sacrificial ZnO NP, inset shows the loading and unloading of the NPCs fabricated from 15.8 vol% ZnO NPs under different loading frequencies (Li et al., 2019)
- Figure 2.9: PVDF fabric based piezoresistive sensor (a) 4-part setup for characterising the developed PVDF sensors, inset showing SEM of PVDF fabric (b) Piezoelectric characteristics of the different sensor samples (c) Sensor response applying a 3 and 5 N load, where the upper figure shows the load force and the lower figure shows the corresponding electrical signal of the sensor (Wang et al., 2011)

- Figure 2.10: a.) Capacitor circuit symbol and schematic of a parallel plate capacitor with the fundamental formula for capacitance b.) Schematic of a capacitor employed as a pressure sensor
- Figure 2.11: a.) Schematic of a capacitive pressure sensor with solid dielectric medium and its compressed state with applied pressure b.) Schematic of a capacitive pressure sensor with a porous dielectric medium and its compressed state (showing increased compression due to micropores) c.) Enhanced relative capacitance change for a porous dielectric medium in contrast to a solid dielectric d.) Applied pressure VS compression strain showing that a porous dielectric medium is more compressible than the solid dielectric medium e.) Enhanced relative capacitance change for a porous dielectric medium in contrast to a solid dielectric medium (Kwon et al., 2016a)
- Figure 2.12: Microstructuring PDMS film into lines and pyramids a.) Schematic process for the fabrication of microstructured PDMS films. (i) A dilute solution of the PDMS mixture of base and cross-linker in hexane is drop cast onto a Si wafer mould (ii) containing arrays of the inverse of the features to be replicated (iii) The PDMS film is vacuum-degassed and partially cured. An ITO-coated PET substrate is laminated to the mould, and the PDMS film is cured under pressure at a temperature of 70 °C for at least 4 hours (iv) Peeling the cured flexible substrate off the mould b.) Pressure response curves for 3 types of PDMS films, one being an unstructured film and the other 2 types being structured with (i) pyramids and (ii) lines c.) Response and relaxation time for the 3 types of PDMS films after loading and unloading of 15 kPa for 4 seconds d.) Response and relaxation time for loading and unloading a bluebottle fly on the 8 x 8 mm² sensor (Mannsfield et al., 2010)
- Figure 2.13: PDMS soft mould and all biodegradable pressure sensor a.) Schematic of a soft lithographic process for making PDMS soft mould (i) Treating the surface of PDMS mould after the first feature replication step from silicon (ii) Pouring PDMS over the treated surface of PDMS mould and cure to complete (iii) Removing the PDMS soft mould and treating with fluorosilane again to use for subsequent feature replications b.) Sensitivity values plotted with spacing distance of the microstructures for pressure values less than 4 kPa (i) Scanning Electron Microscope (SEM) of 182 µm spacing and (ii) 41 µm spacing c.) Simulation data showing the predicted stress-strain relationship of different sidewall angled microstructures (Tee et al., 2014) d.) Schematic of a fully biodegradable and flexible pressure sensor array from microstructured poly(glycerol sebacate) PGS films e.) Measuring a wrist pulse wave when the sensor is placed on top of (i) dry skin, (ii) wet skin and (iii) when the skin is fully covered with artificial sweat (Boutry et al., 2015)
- Figure 2.14: Microarray dielectric layer and microstructured flexible electrodes a.) Fabrication process of the micro-array dielectric layer capacitive pressure sensor. The AgNW's embedded PDMS electrode is laminated onto the micro-array dielectric layer (Shuai et al., 2016) b.) A flexible pressure sensor integrates the top electrode, dielectric layer, and microarray electrode in a sandwich structure c.) Effect of PVDF dielectric layer thickness on the sensor response d.) Relative capacitance response of flat sensor and microarray electrode sensor for the same applied pressure (Shuai et al., 2017a) e.) Schematic of flexible capacitive pressure sensor with a dielectric layer consisting of polystyrene (PS) microspheres (i) Schematic side view of the sensor without any force applied and (ii) with a force applied (Cui et al., 2017)
- Figure 2.15: 3D printing of a microstructured mould a.) Image of printhead of the 3D printer (UP Plus 2 from Tiertime) being used for fabricating an acrylonitrile butadiene styrene (ABS) based mould b.) Schematic of the fabricated capacitive pressure sensor c.) Photograph of the sensor (i) SEM showing the surface structure of the PDMS moulding d.) Relative capacitance response of the developed sensor e.) The whole sensor system, composed of the pressure sensor and the self-designed data acquisition (DAQ) circuit board, is placed on the radial artery at the wrist, and fixed by transparent adhesive tape for real-time monitoring of wrist pulse. The sensor has dimension 0.7 cm x 0.7 cm (i) The real-time measured wrist pulse waveform with relative capacitance change (upper), and the details of the pulse wave in one period (bottom), which contains the percussion wave (P-wave), the tidal wave (T-wave), and the diastolic wave (D-wave) (Zhuo et al., 2017) f.) Fabrication of conductive microstructured PDMS thin films using a 3D printed structured mould (Peng et al., 2018)

- Figure 2.16: Lamination layer for stability and porous pyramids a.) A 3D printed microstructured mould a.) Partially cured PDMS layer which will be the lamination layer of the sensor b.) Slightly anchoring the cured microstructures with the tips facing the partially cured PDMS layer c.) Curing the entire sensor d.) comparison between the previous method which had no lamination layer and e.) the current method f.) Scanning electron microscope (SEM) cross-sectional image shows the microstructured pyramids and lamination layers (Ruth et al., 2019) g.) Schematic diagram of the porous pyramid dielectric layer h.) SEM of the top view of the porous pyramid and base layer i.) relative capacitance response to pressure for a porous pyramid dielectric layer and a solid (non-porous) pyramid dielectric layer j.) relative capacitance response to 5000 cycles of applying 400 Pa (Yang et al., 2019)
- Figure 2.17: Photolithography and 3D printing of pyramidal moulds
- Figure 3.1: a.) Schematic illustration of 3D direct laser writing. b.) Direct laser written protein-repellent PEG-DA framework and c.) photoresistOrmocomp cubes precisely placed (Klein et al., 2011)
- Figure 3.2: FIB setup with a gas injector for platinum deposition (Yao, 2007)
- Figure 3.3: Schematic of the direct-write assembly approach printing setup and the main printing parameters governing print resolution and print quality
- Figure 3.4: Summary of the main parameters (ink viscosity, evaporation of ink mainly based on the solvent used, wettability of the nozzle & substrate and diameter of tip) for stable printing with resolution control for direct-write printing
- Figure 4.1: a.) P-1000 micropipette puller from Sutter Instrument (Oesterle, 2017) b.) Schematic of the borosilicate glass capillary with inner and outer diameter dimensions c.) The front panel provides the user interface for navigating and programming the machine d.) The resulting nozzles after the machine has finished running the program. The program details can be found in the appendix (A.2 P-1000 Sutter Instrument parameter programs)
- Figure 4.2: a.) Microscope images of nozzle apertures from 1 to 35 μm b.) relationship between nozzle aperture (μm) and cooling time (minutes) between each consecutive pull for the same parameter program
- Figure 4.3: Direct-write assembly - 3D printer setup
- Figure 4.4: a.) Loading ink, inserting piston and forming a meniscus at the opening b.) Mounting nozzle to the syringe barrel c.) Mounting nozzle assembly to the printer
- Figure 4.5: a.) Nozzle close to the substrate b.) Parallel lines to make the nozzle-substrate gap constant (levelling) c.) Labview interface for the electronic pneumatic regulator
- Figure 4.6: a.) Capillary bridge formed between the nozzle and the glass substrate b.) Printing a 3D structure
- Figure 4.7: a.) Cjig made of acrylic b.) PCB design of 3 mm square contact pads c.) Schematic showing the printed dielectric on the designed PCB board d.) 3D printed raster pattern on contact pad e.) Flexible Espanex PCB inside Cjig
- Figure 4.8: a.) Photograph of the LCR meter (model LCR-821, Iso-tech) b.) Sensor connected through the Kelvin probes to LCR with acrylic plates (loads) placed above it c.) Schematic of capacitive pressure sensor with pyramidal structured elastomeric dielectric
- Figure 5.1: a.) Image showing carbon black nanoparticles 0.1 wt% immersed in curing agent and the probe sonication in process b.) Image showing a small amount of evaporated curing agent with carbon black nanoparticles on the probe
- Figure 5.2: Schematic overview of the mould process: a.) Printing PVP mould b.) Filling printed mould with PDMS via nozzle c.) Curing mould with PDMS content at RT for 48 hours or in oven at 125 $^{\circ}\text{C}$ for 20 minutes d.) Pipetting a few water droplets onto the mould in order to dissolve the PVP mould and leave behind the cured and structured PDMS moulding
- Figure 5.3: a.) Printed hexagonal structure b.) PDMS filled and cured mould c.) top view of the cured moulding without a mould d.) 3D view of the cured moulding
- Figure 5.4: Steady state response of PVP inks: Viscosity as a function of shear rate
- Figure 5.5: a.) Oscillation stress as a function of shear rate b.) Flow index number for different PVP ink concentrations
- Figure 5.6: Viscoelastic properties of PVP inks: a.) G' and G'' as a function of oscillation stress for the different PVP concentrations and other reported inks (García-Tuñón et al., 2017; Yuxiong Guo et al., 2019a; Valentine et al., 2017)
- Figure 5.7: Ratio of loss modulus to storage modulus as a function of PVP concentration in comparison to other inks (García-Tuñón et al., 2017; Yuxiong Guo et al., 2019a; Valentine et al., 2017), with the 3D printable inks highlighted in yellow

- Figure 5.8: Guide to achieving printability of different PVP ink concentrations with different nozzle sizes: a.) 'Not printable' meaning that the ink would just wet the surface without forming a surface adhering filament b.) 'Printable' meaning that the ink was able to form strands that were adhering to the surface, but it was unable to complete the initial layer due to either nozzle fracture, clogging or overflowing c.) 'Single layer printing' meaning that the ink was able to complete a single layer, but being then not able to complete the consecutive layer due to nozzle clogging or fracture d.) 'Multilayer printing' meaning that the ink was 3D printable and able to form self-standing structures without the nozzle clogging or fracturing at consecutive layers
- Figure 5.9: Star shaped logo of UCLs' Wellcome/EPSCRC Centre for Interventional and Surgical Sciences (WEISS logo) a.) Schematic of the mould, b.) the printed mould and c.) PDMS(10:1) moulding
- Figure 5.10: a.) Schematic of a pyramidal mould structure, b.) the printed mould and c.) Ecoflex moulding
- Figure 6.1: Micro moulding arrays a.) Schematic of path of printer in printing a 2.5D hexagonal micro mould array b.) Successfully printed hexagonal array on glass c-d.) Filling moulds with PDMS (10:1) followed by curing 125 °C for 20 min and letting cool down outside the oven at room temperature (RT) e.) After initial DI water droplet placement, there are still remnants of PVP f.) Repeated placement of DI water droplets completely washed away the PVP and left the moulded and cured PDMS structure
- Figure 6.2: a.) Successfully printed square based pyramid micro mould array of 25 b.) Side view of the printed micro mould array c.) Pyramid filling attempt, with tip being centred above each mould and then lowered into the mould. d-f.) This is followed by applying a back pressure of 0.3 bar into the nozzle. The overhanging droplet of the tip makes contact with the interior walls of the pyramid and thus helps to start filling the pyramid. However, as the ink fills up the upper part of the pyramid along the interior side walls, the bottom part of the pyramid has air bubbles trapped inside it, preventing the ink from reaching the bottom of the pyramid. (Scale bar: 100 µm)
- Figure 6.3: Rectangular (100 µm x 400 µm x 75 µm) based pyramid mould filling process a.) Lowering the tip into the centre of the mould b.) Applying sufficient pressure (0.1 - 0.3 bar) to force elastomer (PDMS_CB composite) out of the tip c-d.) Filling and moving to the right and then to the left hand side of the mould e.) Moving the tip to the surface of the filled mould f.) Turning off the pressure and raising the tip completely away from the filled mould
- Figure 6.4: a.) Example of a sufficiently filled mould with a maximum overfill of ~3 µm b.) Example of an underfilled mould
- Figure 6.5: a.) Schematic demonstrating continuous printing array of moulds with one tip b.) Rectangular based pyramid moulds printed continuously with one tip on glass c.) Top view of a printed array of rectangular based pyramid moulds
- Figure 6.6: Schematic of the pyramid mould printing nozzle demonstrating a.) nozzle fracture when the nozzle moves directly from the top of the printed mould to the surface and b.) successful continuation of the printing array of pyramid moulds by moving the printing nozzle from the top of the printed mould to the outside of the mould and then reaching the surface without nozzle fracture
- Figure 6.7: a.) Schematic showing the side view of the mould and the pipetted uncured PDMS above the mould b.) Schematic showing the side view of the degassing of the pyramidal moulds by placing moulds inside the vacuum chamber to force the trapped air bubbles out of the pyramidal moulds and force the uncured PDMS into the mould c.) Photo showing the PCB board above which the printed moulds and the pipetted PDMS_CB are located. The photo captures the moment when the air bubbles are coming out of the moulds
- Figure 6.8: a.) Schematic showing the side view of the mould completely filled with uncured PDMS_CB b.) Schematic showing the cured PDMS_CB encompassing the mould c.) Photo of the cured PDMS_CB film on the PCB
- Figure 6.9: a.) Schematic showing the side view of the mould and the cured PDMS_CB layer getting peeled off the mould b.) Photo of the tweezers holding peeled film c.) Photo of the peeled film, where the rectangular pyramidal indentations are visible
- Figure 6.10: a.) Schematic showing the side view of the printed mould with cured PDMS_CB filling b.) Schematic showing a cured PDMS_CB moulding after the mould is washed away with DI water droplets c.) Photo of the cured PDMS_CB mouldings on a copper electrode on PCB, forming the microstructured dielectric layer of the capacitive pressure sensor

- Figure 6.11: Overview of making an array of a pyramidal microstructured dielectric layer using direct-write printing for rapid prototyping water soluble micro moulds a.) Schematic showing a printed micro mould array on copper on a PCB: 1) Photo showing the top view of the mould on a copper PCB b.) Schematic showing filled mould: 1) Photo of peeled film and filled moulds on a copper PCB c.) Schematic showing cured structures with the PVP mould washed away: 1) Photo showing the side view of a cured rectangular based pyramidal moulding consisting of PDMS_CB(0.1%) and the 2) angled view. 3) Photo of a cured square based pyramid moulding consisting of PDMS d.) Schematic showing how the fabricated microstructured dielectric medium is incorporated in between two electrodes for capacitive pressure sensing, where a change in applied pressure represents a change in capacitance, which is measured using a LCR meter: 1) Photo of the Cjig measurement platform with flexible PCBs mounted
- Figure 6.12: Comparison of sensor response for structured dielectric (81 pyramids, each $200\text{ }\mu\text{m} \times 200\text{ }\mu\text{m}$ and $100\text{ }\mu\text{m}$ high) and unstructured dielectric (flat film, $100\text{ }\mu\text{m}$ high) layer made up of PDMS(10:1)
- Figure 6.13: Comparison of sensor response for the pure PDMS structured dielectric (81 pyramids, $100\text{ }\mu\text{m}$ high)
- Figure 6.14: Comparison of sensor response for a pure PDMS structured dielectric (81 pyramids, $100\text{ }\mu\text{m}$ high) and a PDMS with CB (0.1% filler concentration, 81 pyramids, $100\text{ }\mu\text{m}$ high)
- Figure 6.15: Higher structures for the bigger sensing range a.) Photo of 4 printed pyramidal moulds of dimensions $800\text{ }\mu\text{m}$ square base and height of $650\text{ }\mu\text{m}$ on 3 mm square copper electrode on top of FR4 (PCB). b.) SEM image of moulding top view and c.) angled view. d.) Schematic of capacitive pressure sensing with a 2×2 pyramid array e.) Relative capacitive pressure change as a function of applied pressure for dielectric layer consisting of 81 pyramidal structures that are $\sim 100\text{ }\mu\text{m}$ high (red line) and a dielectric layer consisting of 4 higher ($\sim 650\text{ }\mu\text{m}$) pyramidal structures (green line) Inset: Showing an expanded view of the graph for $<1\text{ kPa}$.
- Figure 6.16: Effect of varying electrode area a.) Schematic illustrating 4 identical pyramid moulds printed on the corners of each of the electrodes, which are of varying size of 49 mm^2 (7 mm square), 25 mm^2 (5 mm square) and 9 mm^2 (3 mm square) b.) Microscopic image of individual PDMS moulding on one of the corners of the 7 mm square electrode c.) Schematic illustrating capacitive pressure sensing concept for the developed sensor d.) Relative capacitance response of the three developed sensors with respect to the pressure experienced by the pyramidal structures e.) Corresponding gradient values of all three sensor responses for 2 regions of applied mass ($\leq 0.5\text{ g}$ and $\leq 2.5\text{ g}$) f.) Relative capacitance response of the three developed sensors with respect to the pressure experienced by the sensor g.) Corresponding gradient values of all three sensor responses for 2 regions of applied mass ($\leq 0.5\text{ g}$ and $\leq 2.5\text{ g}$)
- Figure 6.17: Response and relaxation time of the developed capacitive pressure sensor (Sensor size of 7 mm square base and $250\text{ }\mu\text{m}$ height) a.) Schematic illustrating water droplets being released from a micropipette ("Adjustable Micropipette 1 – 5 ml," 2018), where each water droplet is set to be $10\text{ }\mu\text{l}$, thereby applying a pressure of 2 Pa to the sensor b.) Graph of relaxation time VS response time for the developed sensor and other reported capacitive pressure sensors (Clementine M Boutry et al., 2015; Cho et al., 2017; Cui et al., 2017; Luo et al., 2018; Mannsfeld et al., 2010; Shuai et al., 2017a, 2016; Yang et al., 2019; Zhang et al., 2017; Zhuo et al., 2017). Response times of human touch (Chortos et al., 2016a), auditory and visual response (Shelton and Kumar, 2010) are shown for comparison
- Figure 6.18: Ratio 'S' as a function of pyramid height for recently reported pyramid structured capacitive pressure sensors (Clementine M Boutry et al., 2015; Cho et al., 2017; Luo et al., 2018; Mannsfeld et al., 2010; Ruth et al., 2019; Tee et al., 2014; Yang et al., 2019; Zhang et al., 2017) and our sensor (red)

- Figure 6.19: Fabricating the prototype of a pressure sensing ring a.) Direct-write printing pyramidal mould array 2 x 2 (each element having a 400 μm square base and being 250 μm high) on a 3 mm square electrode on a flexible PCB (Espanex, Holders Technology). In order to level the flexible PCB, a few water droplets ($\sim 40\ \mu\text{l}$) were placed between the glass slide and the flexible PCB. The printed moulds are then filled with PDMS(10:1) via vacuum filling and cured at 125 $^{\circ}\text{C}$ for 20 minutes. The film is peeled off and the mould is washed away so that the structured PDMS moulding remains behind on the flexible PCB. The flexible PCB is wrapped onto a 3D printed (UP mini 2 ES, Tiertime) hexagonal ring with the help of adhesives. b.) Image showing the complete sensor package integrated on one side of the hexagonal ring and the electrode trace paths being covered with black insulating tape to avoid external interferences. c.) Attached using copper tape to the ring are flexible wires and SMB coaxial cables leading to readout circuitry (Evaluation Board EVAL-AD7745/46EB, ANALOG DEVICES) d.) Schematic of the left hand showing the location of the radial artery (Roh and Lee, 2018) e.) Image showing the pressure sensing ring being employed on a wrist f.) to provide a real-time pulse signal from the radial artery. g.) Close-up of measured and detailed single pulse
- Figure 6.20: 81 pyramid mouldings a) SEM image of the angled side view of the microstructured PDMS(10:1) dielectric moulding layer (81 pyramids, each 200 μm x 200 μm , 100 μm high) on top of 3 mm square copper electrode on FR4 (PCB) b) SEM image of the angled side view of an individual pyramid moulding c) Schematic demonstrating the change in dimensions from the user programmed structure to the actual mean dimensions of the top, bottom and height of a trapezoidal pyramid measured across the 81 pyramid mouldings d.) Schematic demonstrating ink accumulation on the nozzle over printing duration
- Figure 7.1: Ag ink printing: a.) Applied back pressure leading to over wetting b.) Ag ink accumulating above the nozzle while printing thus affecting resolution c.) Printed S- pattern $\sim 27\ \mu\text{m}$ line width
- Figure 7.2: Ag ink droplet on pre-treated glass slides: a.) Wetting of Ag ink droplet on glass substrates pre-treated with different solvents b.) Ag ink droplet placed on the RainX pre-treated substrate after 1 hour
- Figure 7.3: Ag ink printing with the functionalised nozzle: a.) Nozzle functionalisation setup b.) stable printing achieved by removing the back pressure and functionalizing the nozzle with RainX c.) ink is not accumulating on the nozzle even after printing corners d.) S-pattern repeatedly printed with a single functionalized nozzle with 0 bar back pressure
- Figure 7.4: Nozzle cleaning stations: a.) nozzle printing on FR4 with a DI water droplet at the side of the substrate b.) PVP ink accumulated nozzle moving into a water droplet c.) printing nozzle after moving out of the water droplet
- Figure 7.5: a) Viscosity as a function of shear rate and b.) G' and G'' as a function of oscillation stress for the PVP/PVDF and PVP inks
- Figure 7.6: a.) A consecutive squares pattern printed with a $\sim 5\ \mu\text{m}$ nozzle on glass. b.) Same pattern printed on stainless steel with interline spacing of 100 μm and c.) with interline spacing of 200 μm
- Figure 7.7: a-c.) A D-pattern printed on polyimide and copper for varying layers/heights d.) A D-pattern with 100 layers zoomed in while the nozzle is printing. e.) Side view of the printed D-pattern under the microscope and f.) an angled view.
- Figure 7.8: a.) Hexagonal structure printed on polyimide up to 30 layers b.) Schematic overview of the printout showing that wall thickness and the diameters of the hexagon remain constant throughout c.) Schematic of the resulting 30 μm high hexagon with a constant wall thickness of 3 μm
- Figure 7.9: a-d.) Continuous array printing with PVP ink accumulating at the nozzle and clogging up the nozzle e-h.) Continuous array printing with PVP/PVDF ink successfully achieving >15 layers.
- Figure 8.1: Printed raster pattern on glass a.) top view and b.) angled side view
- Figure 8.2: Varying inter-pyramid material concept schematics. a.) Schematic showing side view of PDMS pyramids with air as the inter-pyramid material and b.) schematic showing side view of PDMS pyramids with a high dielectric constant material as the inter-pyramid material
- Figure 8.3: The next version of the pressure sensing ring consisting of 5 sensors and a wireless readout circuit
- Figure 8.4: Microwave-surface textured micropyramids a.) SEM image of micropyramid b.) Scaled SEM image showing the microwave-textured surface

- Figure 8.5: Simulation data showing a.) predicted stress-strain relationship for different sidewall angled micropylramids and b.) predicted effective modulus of the micropylramids as a function of the sidewall angle (Tee et al., 2014)

Chapter 1 - Introduction

1.1 Background

Life expectancy across most parts of the world has continuously risen over the last ~150 years (Clarfield, 2017). In some countries, women are expected to live to almost 85 years, whereas ~180 years ago, the record for life expectancy was held by Swedish women at just above ~45 years (Gross, 1992).

While there are many contributors to this progress, one of the main reasons is the major strides taken in the world of healthcare and medicine, and in particular major technological advances in clinical fields such as computed tomography scans (Hendee, 1989), surgical robots (Kehoe et al., 2014), etc. (Antiretroviral and Cohort, 2008), which have enabled better and wide reaching treatments.

However, attached to these progresses are high costs, at a time of increased healthcare cost cuts (Tricoli et al., 2017), making their fabrication and implementation challenging even in developed countries. Moreover, the high costs make translating these enhancements into developing countries challenging, with life expectancies in some developing countries being still below 60 years (Roser, 2019).

Even though people are living for longer, the elderly are also facing more chronic conditions, which require frequent hospital visits. They face long waiting times before and during hospital appointments for just routine check-ups, where a study has even associated longer waiting times between medical centre

appointments to negative health outcomes, even mortality (Prentice and Pizer, 2007).

All of this is screaming for the reduction of healthcare costs, in particular the manufacturing costs of medical devices (Gibson and Srinath, 2015), while preserving and advancing the functional benefits of such high-tech medical devices and approaches.

1.2 The Internet of Things (IoT)

By the same token the concept of an internet of things (IoT) is becoming a reality. The term was first coined by Ashton K. (Ashton, 2010), where he describes a world where just like we humans have the internet to communicate to other humans and devices, an internet of things would be an internet for other 'things' like computers that will be able to communicate and feedback – without human aid – with other computers and devices, based on data the computers would have gathered themselves using sensor systems (Gubbi et al., 2013; Miorandi et al., 2012; Zanella et al., 2014).

The IoT would enable futuristic medical devices to be programmed such that remote monitoring of patients – especially the elderly - is made possible irrespective of their location and without needing any expertise. This would lower the costs for the health sector and enable routine checks to be automated. This would enable clinicians and doctors to focus on the tasks that only they can do. However, in order to realise such a reality and for such devices to reach more places, the devices have to be miniaturised for high integrability into already existing expensive systems and tools.

1.3 Miniaturised devices

Miniaturisation of such devices and, in particular, miniaturisation of the many sensors making up large parts of these devices not only addresses component integrability, but enhances the sensors' functionality by opening up pathways for beneficially unique capabilities such as enhanced sensitivity (Chen et al., 2014, 2016; Mitrakos et al., 2017), operation speed, efficiency in space occupied per square unit area (Andelin and Curlin, 1991), material efficacy and more.

Many medical devices commercially available are non-flexible/rigid (Nokes, L.; Jennings, D.; Flint, T.; Turton, 1995; Webster, 1978) and used in a clinical setting. However, they are limited in terms of their integration for physiological measurements and long term monitoring reliability (Jog, 2013; Keum et al., 2011). Soft, stretchable and flexible electronic devices have led to a novel platform in healthcare (Liu et al., 2017). Flexible sensors enable unprecedented access in various aspects including physiological long term measurements. This is due to their ability to use their flexibility to match difficult to sense areas, such as the skin, where the conformity of the sensing element to the electronic-skin interface is crucial for the wearable medical device to provide effective measurements (Rogers, 2015; Wang et al., 2012). There are various types of flexible sensors, but the focus of this project lies in flexible pressure sensors. These flexible pressure sensors can convert the applied pressure into a useful signal for the user to characterise. The signal can be obtained in many forms including a change in charge/electric potential (piezoelectricity), a change in resistivity (piezo resistivity), a change in capacitance (piezo capacitive), etc. In this project the focus is on capacitive pressure sensors, due to their low hysteresis, high sensitivity and high integrability with other sensors, etc. (Huang

et al., 2019). Particularly useful for the clinical setting is the ease of integrating capacitive pressure sensors into wireless circuitry where the capacitor itself plays a key role for wireless transmission, as has been demonstrated previously (Chen et al., 2014).

1.4 Enhanced capacitive pressure sensing

Over the last decade, some groups have shown that a flexible dielectric medium can be enhanced in terms of pressure sensitivity by either introducing air voids (porosity) of random size and location into the elastomer (most commonly PDMS) (Chen et al., 2016; Kwon et al., 2016a) or actually structuring the elastomers into microstructures such as square-based pyramids (Clementine M Boutry et al., 2015; Chen et al., 2014; Mannsfeld et al., 2010; Tee et al., 2014), so that the air voids are not random, but rather engineered in place and size (Figure 1.1).

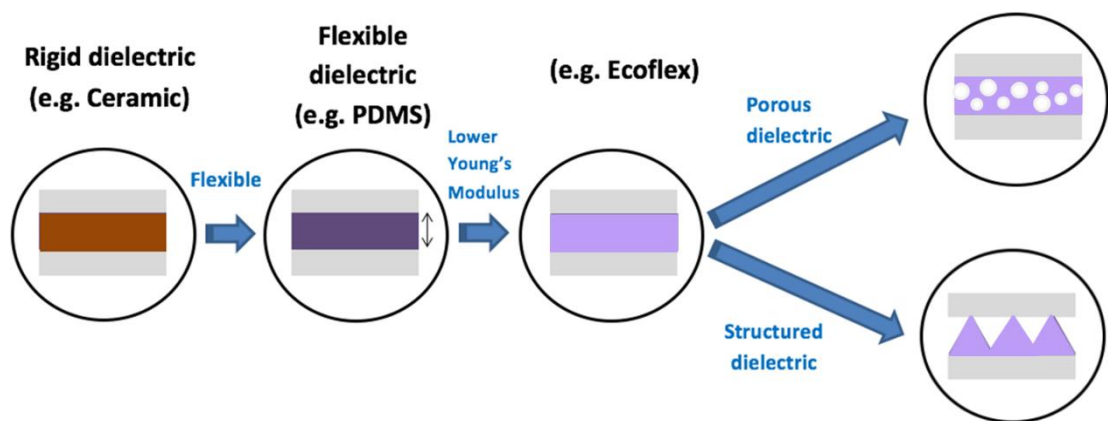


Figure 1.1: Overview of the general trend of development in enhanced flexible capacitive pressure sensors

Mannsfeld et al. (Mannsfeld et al., 2010) fabricated a novel capacitive pressure sensor and demonstrated the immense benefit of structuring the dielectric medium. For the microstructured dielectric medium the sensor sensitivity was

increased by 30-fold in contrast to an unstructured dielectric medium. In all cases the 'structuring' of the dielectric medium reduces the effective Young's modulus of the dielectric medium non-linearly. Since the capacitance is inversely related to the distance between the two electrodes of a capacitor, this corresponds to a non-linear increase in pressure sensitivity. Structured dielectric mediums have been fabricated mainly using photolithography (Chen et al., 2014; Mannsfeld et al., 2010; Mitrakos et al., 2017; Tee et al., 2014) and other microfabrication techniques (Kwon et al., 2016a; Shuai et al., 2017a).

A group from Shanghai Jiao Tong university (Zhuo et al., 2017) have shifted the fabrication of the dielectric layer mould from the clean room to the open air. The group 3D printed rectangular microgroove moulds for structuring the PDMS dielectric layer into rectangular microgrooves using a commercially available 3D printer (UP Plus 2 from Tiertime). But the printer is a fused deposition modelling (FDM) printer, which relies on heating the extruder ($> 80\text{ }^{\circ}\text{C}$) and thermally decomposing (usually) thermoplastics into the desired shapes. The group printed the microgroove moulds using acrylonitrile butadiene styrene (ABS) filament. The process of thermally decomposing thermoplastics like ABS has been reported to have toxic effects on rats (Zitting and Savolainen, 1980), mice (Michelle M. Schaper, 1994) and humans (Oberdörster et al., 2005). Additionally, the printer was limited by a resolution of $400\text{ }\mu\text{m}$ and the fabricated microstructures consisted of rectangular microgrooves, which offer lower deformation than micropylamids, resulting in lower sensor sensitivity.

However, Lewis (Lewis, 2000) demonstrated that with the direct-write assembly approach and carefully formulated inks, successful 3D fabrication at the

micrometre scale was possible. The carefully formulated inks are made such that they cure into filament shape upon exiting from the nozzle. The approach works at room temperature (RT) and does not require any heat extruder. This opened up the door for more materials that were previously not 3D printable.

1.5 Additive manufacturing

Additive manufacturing (AM) in essence consists of designing a 3 dimensional object in digital form – computer aided design (CAD) – and then to build up the object in the physical world layer by layer through depositing materials like metals, polymers or composites. 3D printing falls under the umbrella of AM, but is also now commonly used as a synonym for AM (Zhai et al., 2014).

In contrast to conventional subtractive manufacturing processes, which work by progressively removing material from blocks/objects (e.g. photolithography), 3D printing fabricates the objects by directly depositing the materials layer by layer, with the number of layers being based on the printing resolution of the system. Over the last decade (Fang and Aabith et al., 2017), multiple high-resolution (<10 μm) 3D printing systems have been developed to effectively tackle some of the many manufacturing challenges in various applications that require high-precision and complex-structure fabrication capability, like orthopaedics (Van Noort, 2012), tissue engineering (Yeong et al., 2004), nanoelectronics (Park et al., 2007) and more. Such developments and the like have made high-resolution 3D printing systems a progressively reliable option for rapid prototyping and rapid manufacturing of small-scale (micro/nanoscale) devices for various sectors including robotics, sensing, imaging, to name just a few.

1.6 Aims and objectives

The aim of this study is to develop safe, rheologically characterised, high-resolution 3D direct-write printable inks, particularly with an objective to decouple ink formulation from precision prototyping. Then to employ the inks for AM fabricating miniaturised sensors, in particular microstructured dielectric media of capacitive pressure sensors for healthcare oriented applications.

The thesis consists of 8 chapters. The second and third chapter form the literature review of the thesis, where the second chapter focuses on flexible sensors in healthcare and, in particular, on capacitive pressure sensors that have microstructured dielectric mediums. The third chapter focuses on forms of high-resolution ($<10\text{ }\mu\text{m}$) 3D printing and the importance of the careful tuning of ink properties to enable 3D direct-write printing.

The fourth chapter focuses on the main experimental methods used, which includes details of the direct-write printing setup for printing microstructured dielectric media and the characterisation setups used for the consequently developed capacitive pressure sensors.

The fifth chapter includes results on novel PVP inks formulated and rheologically characterised for open air high-resolution 3D printing. This is followed by examples of the subsequently developed rapid prototyping micromoulds.

The sixth chapter highlights the employment of the developed micro mould approach for fabricating pyramid structured dielectric media for capacitive

pressure sensing. The characterisation results of the developed sensors are also presented there.

The seventh chapter focuses on some ways of improving the print resolution. The chapter looks first at functionalising a glass nozzle to avoid ink accumulation during print out. The chapter then highlights how blending PVDF and PVP enables the printing nozzle to reduce wetting during print outs with smaller nozzle apertures.

The eighth and final chapter highlights the summary of achievements of the thesis and points towards the next steps that can be taken to build from this work.

Chapter 2 – Healthcare devices that are flexible

This chapter reviews and highlights the importance of flexible devices and flexible sensors in healthcare. Then it focuses on flexible pressure sensors and in particular on capacitive pressure sensors. The chapter then concludes by highlighting the different forms of enhancing capacitive pressure sensing and the methods currently employed in fabricating such enhanced capacitive pressure sensors. The chapter is sprinkled all over with important examples of flexible healthcare devices. This chapter forms the first part of the literature review of this thesis.

2.1 Introduction

Microelectronic circuits today consist of a complex plethora of carefully tuned and sensitive components that operate under specified conditions. While such silicon-based electronic systems are well established, they are restricted by their rigidity, that limits each etched silicon wafer to a particular application, without much or no flexibility. However, this has started to change, with some major initial strides taken almost two decades ago by the three Nobel laureates (Alan J. Heeger, Alan G. MacDiarmid & Hideki Shirakawa) in chemistry, ‘for the discovery and development of conductive polymers’ (Nobel Media AB, 2000). Such important advances have laid the foundation for the organic electronics sector to exist, blossom and boast about great flexibility and cost effectiveness in contrast to their rigid silicon based counterparts. The ‘curved’ or ‘shaped for the user’ devices available on the market all point towards this progress. The advancements made have generated a growing demand for portable but user specific devices, like smartphones, where the number of users with a

smartphone connection by the year 2017 was estimated to already be at 2.5 billion (Rashidi et al., 2014). Samsung Electronics have recently announced that they will be releasing before the end of this year (2019) a foldable smartphone, the Samsung Galaxy Fold (Figure 2.1).



Figure 2.1: The Samsung Galaxy Fold is a foldable phone (Samsung, 2019)

On the other hand, the healthcare sector has much to benefit from such developments, where wearable devices that started as trackers of physical exercise and activity (Kim et al., 2019) are now much sought after by doctors and clinicians (Dias and Cunha, 2018) for more challenging tasks like managing diabetes or remote monitoring of the elderly. This is further facilitated in a world where the cost of healthcare is rising (Savino J.A., 2019) and healthcare systems and their associates are overburdened.

The potential of such wearable devices in this sector are such that healthcare professionals could only be facing tasks that only they can do and not spending their valuable and much needed time on tasks that can be dealt with by patient friendly, non-invasive devices at home, away from hospitals. Devices that can monitor vital signs (heart rate, temperature, blood pressure, etc.) of the patient – especially patients with chronic conditions - and alert the relevant healthcare

professional when something is not right. It would be even better if the devices could be personalised to the specific user to provide tailored data. As in the case of heart rate monitoring, where the average athlete would have a lower rest pulse than the average non-athlete (Middleton, 2018).

Similarly, such devices should be tailorable for the application and its different conditions. The device developed by Mannoor et al. (Mannoor et al., 2012) demonstrated this. They developed a graphene nanosensor that was able to wirelessly detect bacteria in saliva and monitor respiration (Figure 2.2a-c). The graphene sensor was transfer printed onto a bioresorbable, flexible silk film, which facilitated the intimate biotransfer of the graphene sensor onto tooth enamel. The sensor was even tuneable via the self-assembly of antimicrobial peptides so that it could detect individual bacterium (single-cell levels) like E.coli and keep them bound longer than when the graphene sensor was not functionalised with a chemically synthesized bifunctional peptide. The noise level was varying across the signal between $\pm 0.05\%$ to $\pm 0.2\%$, but didn't affect the sensor performance since the bacterium detection resulted in a change of $\sim 0.6\text{-}0.7\%$ (Figure 2.2d,e). Experimental tests were conducted on bovine tooth and not human teeth that are smaller, that would require further miniaturisation of the sensor, which would make powering of the sensor more challenging.

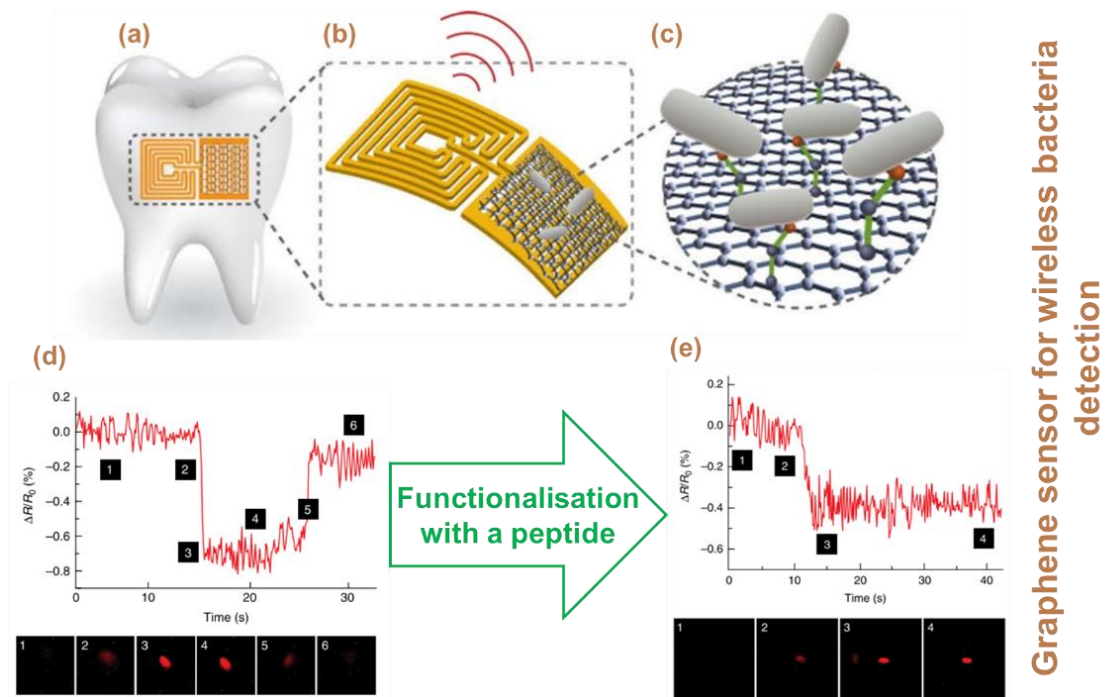


Figure 2.2: Graphene nanosensor a.) Biotransfer of graphene nanosensor onto the surface (enamel) of the tooth b.) Schematic of the graphene nanosensor with illustration of wireless readout c.) Schematic showing binding of pathogenic bacteria by peptides self-assembled on the graphene biosensor d.) electrical resistance (upper) and fluorescence (lower) data recorded simultaneously versus time showing binding/unbinding of a single *E.coli* bacterium on a bare graphene nanosensor, images are $12\ \mu\text{m} \times 12\ \mu\text{m}$ e.) data recorded simultaneously versus time showing binding of a single *E.coli* bacterium on a peptide-functionalised graphene nanosensor, images are $20\ \mu\text{m} \times 20\ \mu\text{m}$ (Mannoor et al., 2012)

Powering such devices is important, especially for long term use, which partly explains the tremendous amount of research that is happening in the electronic textiles (e-textiles) world (Atalay et al., 2018; Buechley and Eisenberg, 2009). Lee et al. (Lee et al., 2013) designed a fully functional wearable textile battery in the shape of clothes and watchstraps (Figure 2.3a), which showed that even under severe folding-unfolding motion - simulating physical wearing conditions - similar electrochemical performance to standard metal foil based cells could be achieved (Figure 2.3c). The fabric consisted of polyester yarn (current collector), where each yarn consists of multiple strands was coated with nickel (Ni) and battery composite (Figure 2.3b).

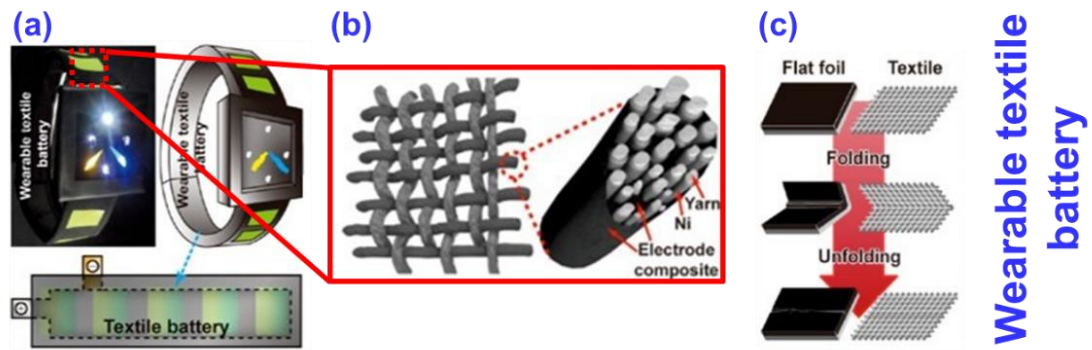


Figure 2.3: Wearable textile battery a.) Photograph and schematic of a watch with a wearable textile battery strap. (Left) 6 LEDs (1 yellow=42 mW, 1 blue=62 mW & 4 whites=62 mW) were lit up as a demonstration of a functioning watchstrap battery b.) Schematic of woven battery electrode yarns, where each yarn consisting of multiple strands is coated with nickel and a battery composite c.) Schematic comparing the electrode based on a standard flat metal foil and the textile battery electrode is based on the woven yarn during repeated folding tests (Lee et al., 2013)

Since a lot of monitoring is possible at the device-skin interface (Liu et al., 2017), the conformity of the device to the skin is of paramount importance. Better conformity will result in better data and thus better diagnosis. Thus a conformal device like a temporary tattoo – electronic tattoo - that could provide data directly from of the skin would be a way forward. Electronic tattoos are designed on flexible substrates or protective coatings made up of silicone materials like PDMS, Ecoflex, or other polymeric materials like poly(vinyl alcohol) (PVA) and polyethylene terephthalate (PET), which enable conformal and optimised skin access for good skin-electrode contact. Recently, some groups have established self-healable electronic tattoos, which is a big stride forward in the electronic tattoos sector. Wang et al. (Wang et al., 2019) have developed a self-healing multifunctional e-tattoo that is based on a graphene/silk fibroin/ Ca^{2+} (Gr/SF/ Ca^{2+}). Their e-tattoo is highly sensitive to variations in strain, humidity and temperature (Figure 2.4a). The multistimuli e-tattoo was employed by the group to demonstrate monitoring of

electrocardiograms (ECG) (Figure 2.4b), temperature (Figure 2.4c) and respiration (Figure 2.4d).

The self-healing ability of human skin is an important feature for any human skin mimicking device, which is why the group have successfully incorporated this ability into their e-tattoo, so that their e-tattoo is not just multifunctional, but also self-healable. The self-healing ability of the e-tattoo was demonstrated (Figure 2.4e) by connecting a commercial light-emitting diode (LED) through copper electrodes across a Gr/SF/Ca²⁺ film and applying a constant voltage of 1.5 V, which resulted in the LED lighting up. The film was then cut into two parts with a razor blade, which resulted in the LED switching off. Then a water droplet was applied to the fractured region of the film, that resulted in the fractured film repairing mechanically, which consequently switched the LED on again. This is due to the SF/Ca²⁺ matrix swelling up when water was applied and the reformation of hydrogen and coordination bonds, leading to the physical fusing of the two separated parts of the film. Additionally, the current of the Gr/SF/Ca²⁺ film recovered its original conductivity with a self-healing efficiency of 100% within 0.3 s for multiple cutting and healing cycles (Figure 2.4f).

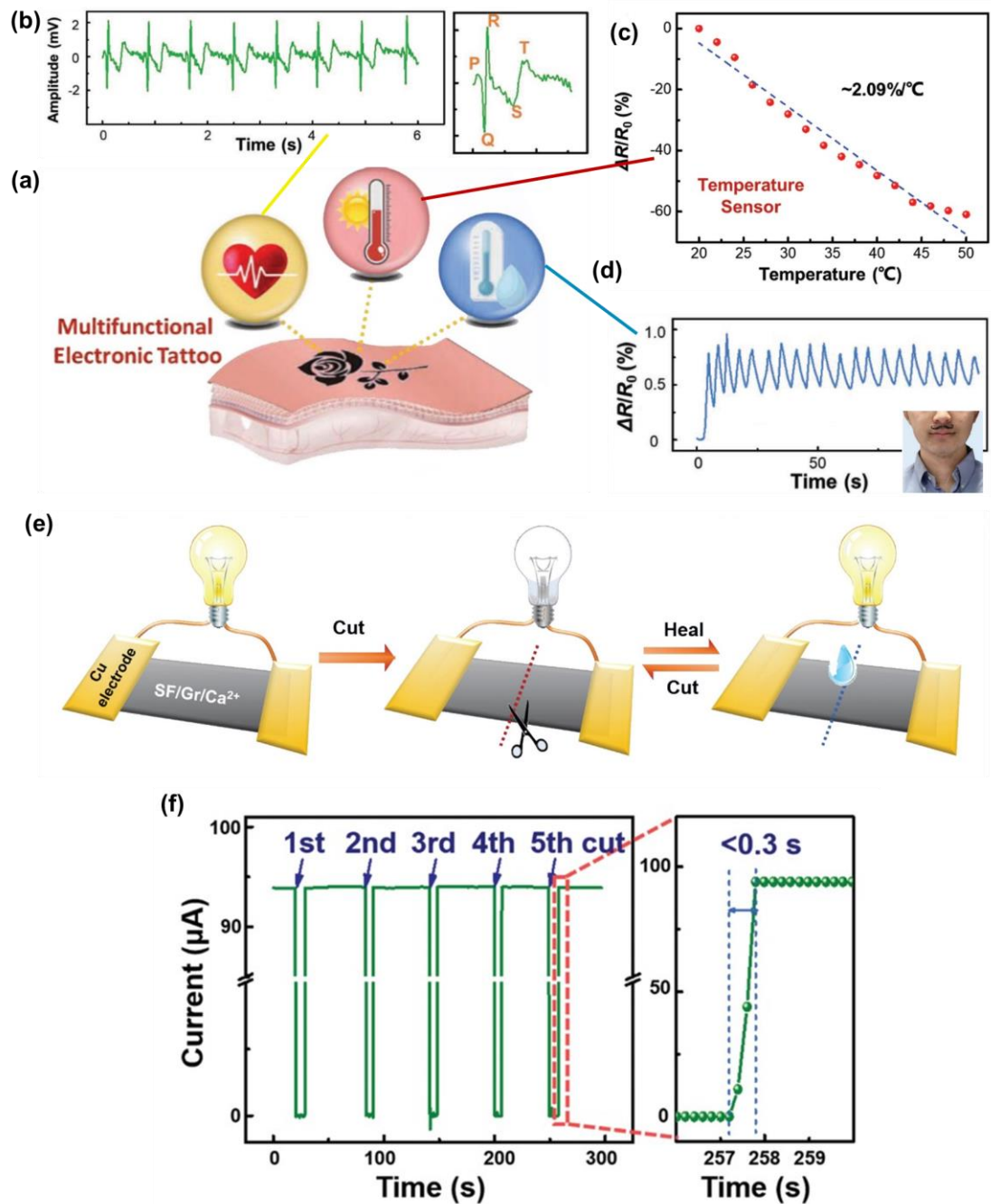


Figure 2.4: Self-healable and multifunctional e-tattoo a.) Schematic illustration of the Gr/SF/Ca²⁺ E-tattoo b.) Relative resistance changes of ECG response, image shows the corresponding enlargement of a single signal waveform c.) Temperature response performance d.) Relative resistance change of humidity response of (inset) moustache tattoo attached directly beneath the nose to monitor respiration e.) Schematic illustrations showing a visible fracture and healing process of the LED circuit interconnected with a Gr/SF/Ca²⁺ film f.) Electrical measurements of the films during five cutting and healing cycles and the zoomed image shows that the film heals within 0.3 s (Qi Wang et al., 2019)

Moreover, clinicians are looking for devices to monitor in-vivo during operations.

Devices that can adapt to their already existing surgical gloves or expensive

surgical tools, which are essential for the clinical task. Ying et al. (Ying et al., 2012) developed electrotactile silicon nanomembranes for fingertip electronics (Figure 2.5a) that have wide usage in instrumented surgical gloves and in human-machine interfaces. The finger glove shows the perception of touch on a dry human thumb as a function of voltage and frequency (Figure 2.5b), where the required voltage for sensation decreases with increasing frequency. Similarly, for the strain gauge array on the finger tube, the relative resistance change was recorded for thumb bending (Figure 2.5c black line) and side to side motion (Figure 2.5c red line), where the bending results in the gauge experiencing tensile strain which translates into the resistance increasing. Since the array is located near the knuckle of the thumb, the side to side motion results in no change in resistance as expected.

Wei et al. (Wei and Simaan, 2012) modelled and experimentally demonstrated a steerable cannula robot (Figure 2.5d) that is suitable for a variety of medical applications including microstent delivery, catheterisation and drug delivery. Figure 2.5e (i-xii) shows the successful microstent delivery process with the steerable cannula robot, where Figure 2.5e (i) shows the initial setup followed by the robot poking through the top surface of the artificial blood vessel (Figure 2.5e (ii, iii)) and then adjusting its angle via extending the angle adjustment tube (Figure 2.5e (iv-vi)). This is then followed by the extension of the stent pushing tube to deliver the stent (Figure 2.5e (vii-ix)) and then the complete retraction of the stent pushing tube from the artificial blood vessel, leaving behind the stent inside the artificial blood vessel (Figure 2.5e (x-xii)). This work has shown the potential of such flexible devices being utilised by surgeons in demanding

operations, where monitoring of the applied force is important for a safe operation.

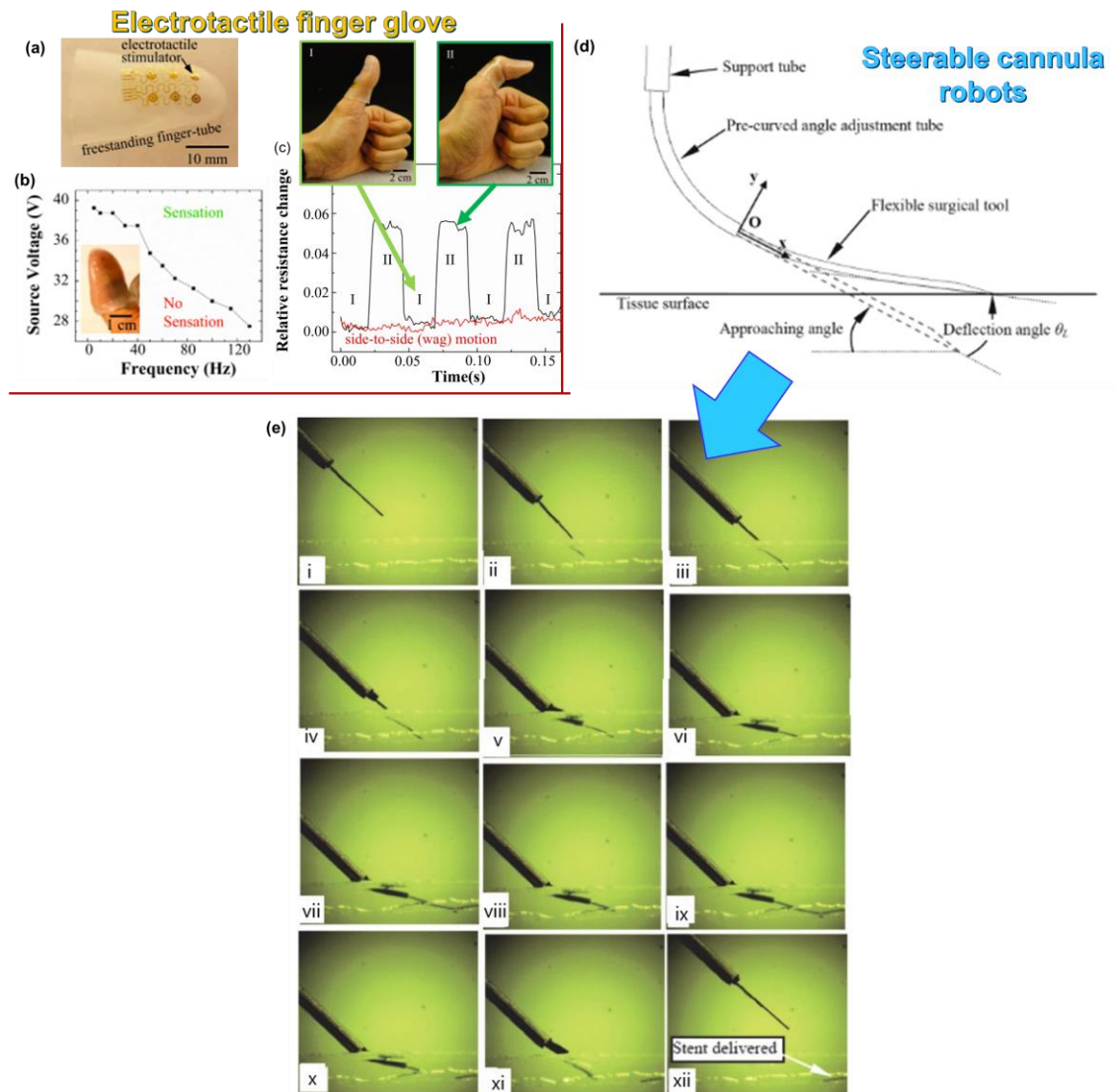


Figure 2.5: Electrotactile finger glove (Ying et al., 2012) and steerable cannula robots (Wei and Simaan, 2012) a.) Electrotactile array on freestanding finger tube b.) Voltage needed for electrotactile sensation as a function of stimulation frequency, image shows electrotactile array on a human finger during the experiment c.) Resistance change of a representative gauge during bending cycles (black) and side to side motion (red), images of strain gauge array on a finger-tube mounted on thumb in (I) straight and (II) bent positions d.) Illustration of flexible surgical tool and its setup e.) experimental image for microstent delivery in an agar-based artificial blood vessel channel model

Such needs and the like have driven much of the research on flexible electronics for healthcare in recent times (Wang et al., 2017), with fruits being harvested in the form of smart lenses (Senior M., 2014), rolled-up glucose

sensors that can be inserted into microcatheters (Li et al., 2007), nanomembranes for fingertip electronics (Ying et al., 2012), steerable cannula robots (Wei and Simaan, 2012), e-tattoos (Liu et al., 2017; Qi Wang et al., 2019), etc. To further enhance such flexible devices, research groups are working on adding more and more functionality to each flexible device, so that more varied data can be collected/sensed from each flexible device, i.e. a lab on skin (Liu et al., 2017). This is achieved by integrating flexible/soft sensors.

2.2 Flexible sensors

Sensors are 'devices that detect or measure a physical property and record, indicate, or otherwise respond to it' ("Definition of Sensor by Lexico," 2019) and can be broadly divided into flexible and non-flexible sensors. Non-flexible sensors are rigid and have been rooted deep into various sectors ranging from environmental monitoring sensors on submarines (Mayer et al., 2019) in the depths of the ocean to remote sensing systems employed on satellites (Chong and Kumar, 2003).

However, with an increasing focus on personalised devices that are able to offer user specific device functionality, the need for flexible sensors – sensors that can be 'flexed' into compliant operation with minimal impact on the overall design of the existing system – has never been greater. Flexible sensors, differ essentially in terms of the materials they consist of – being mainly polymers like polycarbonate (Nanto et al., 2000), polysulfone (Kuroiwa et al., 1995), polydimethylsiloxane (Mitrakos et al., 2017), poly(ethylene terephthalate) (Akiyama et al., 2006), etc. - which tend to have lower Young's moduli, enabling flexibility for advanced functionality. This extended ability brings about many

benefits for numerous sectors, including automotive systems (Engler et al., 2016), medical devices (Khan et al., 2016), wearable devices (Kim and Ahn, 2017), solar cells (Lungenschmied et al., 2007), consumer electronics (Sugimoto et al., 2004), etc (Li et al., 2012). Amongst them, the healthcare sector has much to profit from their flexibility and adaptability. Flexible sensors enable unique conformal access, e.g. electronic-skin (Dagdeviren et al., 2014; Huang et al., 2012; Jeong et al., 2014; Yeo et al., 2013), that provides previously untapped data for monitoring and diagnosing patient conditions. Their capabilities are such that flexible sensors have been employed in many types of applications including humidity sensing (Sotzing et al., 2000; Su and Wang, 2007), pH sensing (Huang et al., 2011; Urban et al., 1992), temperature sensing (Moser and Gijs, 2007; Yang et al., 2015), optical sensors (Kolle et al., 2013), magnetic field sensors (Melzer et al., 2015), strain sensors (Daoud et al., 2005; Lang et al., 2008; Ryu et al., 2015; Yamada et al., 2011), glucose sensors (Jina et al., 2014; Kudo et al., 2006; Mitsubayashi et al., 2003) and pressure sensors (Kwon et al., 2016b; Nakamura et al., 2014; Shuai et al., 2017b, 2017a; Tee et al., 2014; Woo et al., 2014; Yu et al., 2017; Zhuo et al., 2017). The focus in this project is on flexible pressure sensors for healthcare applications.

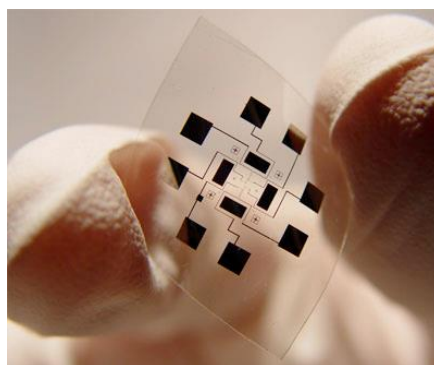


Figure 2.6: A flexible gas sensor – Nanowire on a plastic gas sensor for detecting environmental pollutants (Mcalpine et al., 2007)

2.3 Flexible pressure sensors

2.3.1 Fundamentals

Broadly speaking, the components of flexible pressure sensors are a flexible substrate, a flexible electrode and a flexible functional element/material. The common choices for flexible substrates are PDMS, EcoFlex, PET and Polyimide. As for flexible electrodes the selection is from flexible PCBs, sputtered gold, silver, ITO, copper or just conductive tapes. The flexible functional element/material determines the sensing mechanism of the flexible pressure sensor. There are various sensing mechanisms for flexible pressure sensors, including piezoresistive, piezoelectric, triboelectric, capacitive and optical. The next sections will expand on the main sensing mechanisms for flexible pressure sensors and their respective strengths and weaknesses. Capacitive pressure sensors are elaborated in section 2.4.

The performance of a flexible pressure sensor can be measured in terms of five main indicators: sensitivity, sensing range, response time, relaxation time and durability. In order to elucidate the key performance indicators of pressure sensors, the characteristic responses of a reported capacitive pressure sensor (based on silver nanowires embedded PDMS with a microarray structure (Figure 2.7a) fabricated by Shuai et al. (Shuai et al., 2017a) are presented in Figure 2.7.

The sensitivity (S) of a pressure sensor is defined as $S = (\Delta E/E_0)/\Delta P$, where ΔE is the electrical signal change (Δ resistance, Δ voltage, Δ capacitance, etc.), E_0 is the initial electrical signal value when no pressure is being applied to the sensor and ΔP is the change in pressure over which the particular electrical

signal change (ΔE) is occurring (Huang et al., 2019). Based on the sensing mechanism, it is possible for a flexible pressure sensor to have multiple sensitivities over a wide sensing range, as in Figure 2.7b, where the sensitivity is $2.94 \pm 0.25 \text{ kPa}^{-1}$ for a sensing range from 0 to 2 kPa and drops to $0.75 \pm 0.06 \text{ kPa}^{-1}$ for the sensing range from 2 kPa to 6.7 kPa. Generally speaking, the higher the sensitivity and sensing range, the better the pressure sensor is considered to be, as it can cater for more applications.

The response time of a flexible pressure sensor can be defined as the time taken to achieve 90% of the stable output (Huang et al., 2019) when a load/force is loaded/applied to the sensor. It demonstrates how fast a pressure sensor responds to a pressure change. The response time usually ranges from a few ms to close to 1 sec, which is good for healthcare devices and other similar applications, where the response time has to be as low as possible (Park et al., 2018), but for few specific 'slow' applications like level measurements with submersible pressure transmitters in liquid mediums (Shitashima et al., 2008) a high response time ($> 1 \text{ sec}$) is beneficial. The relaxation time for a flexible pressure sensor is the time taken from removing the load/force of the sensor to the signal drop starting to stabilise. From Figure 2.7c the response and relaxation time of a capacitive pressure sensor can be identified to be just under 50 ms. The response and relaxation time are usually similar, given that the applied force/load is within the linear viscoelastic region of the active sensing material. The durability of a flexible pressure sensor defines how consistently the output of the sensor responds to a given/fixed load/force being applied repeatedly over multiple cycles. Figure 2.7d shows that the capacitive pressure sensor demonstrated a stable input-output relation a pressure of 2 kPa for 1000 cycles.

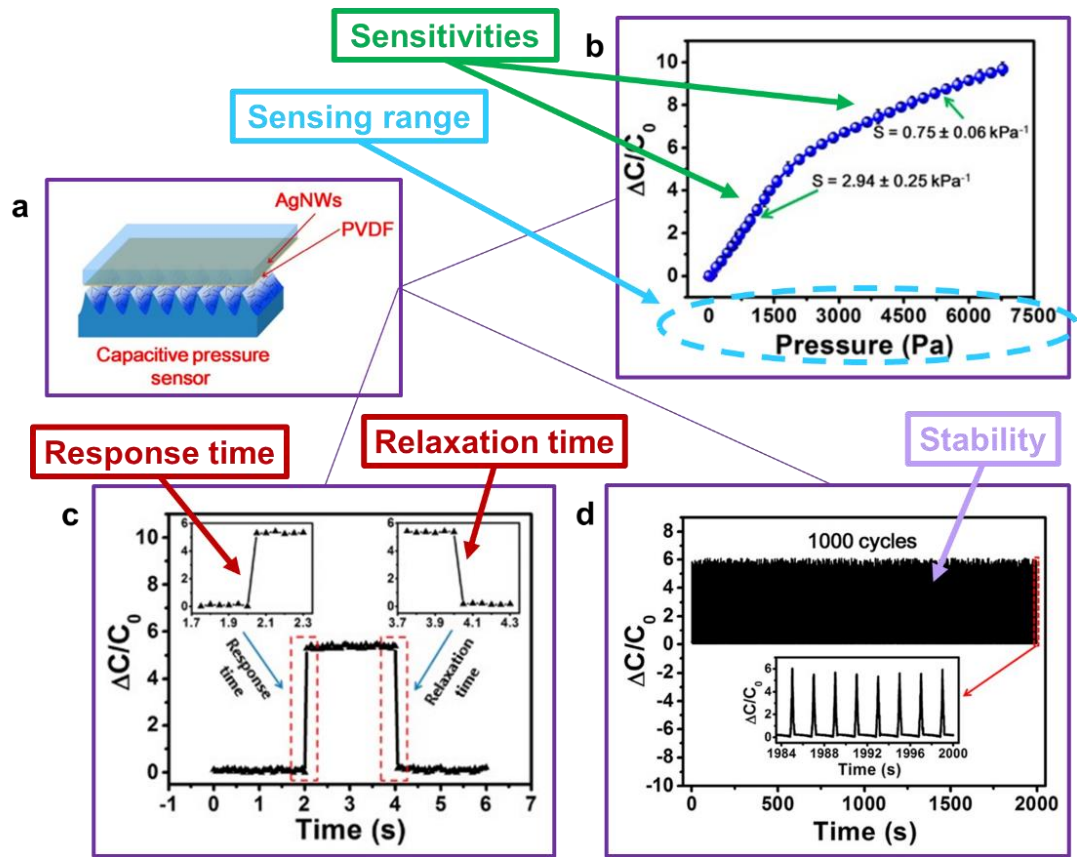


Figure 2.7: Example of sensor performance indicators a.) schematic of a capacitive pressure sensor based on a silver nanowires embedded PDMS with a microarray structure b.) relative capacitance change over a pressure range of 0-6.7 kPa with a sensitivity of $2.94 \pm 0.25 \text{ kPa}^{-1}$ and $0.75 \pm 0.06 \text{ kPa}^{-1}$ for pressure ranges 0 to 2 kPa and 2 kPa to 6.7 kPa respectively c.) sensor response time and relaxation time d.) sensor response stability for a repeated compression test for 1000 cycles (Shuai et al., 2017a)

2.3.2 Piezoresistive sensing

Piezoresistive pressure sensors are a common choice for pressure sensing owing to the many benefits they offer, including simplicity in the structure of the device (Li et al., 2019), straightforward circuitry for signal collection and low susceptibility to electromagnetic pick-up (Oh et al., 2019), etc. (Liu et al., 2018). Piezoresistive pressure sensors contain pressure sensitive elements which change their resistance to the flow of current when a force (compression or strain) is applied to them. The pressure sensitive element should have sufficient charge transport paths for good electrical flow and also good elasticity for reliable mechanical performance when in use. This is why composite materials

made up of an elastic matrix with conductive fillers are the most popular material choice for piezoresistive pressure sensors (Huang et al., 2019).

However, in order to maintain stable sensing characteristics, the conductive fillers must be well dispersed (minimal aggregation) and also lodged well in the elastic matrix (Hussain et al., 2001; Knite et al., 2004), which is why conductive composites and consequently piezoresistive pressure sensors are generally prone to large hysteresis (Mahmoud et al., 2007), especially for large pressures. This is also why it is common to see research groups choose to apply a relatively low pressure (~10% of maximum applicable pressure) value cyclically on their developed piezoresistive sensor for stability testing. As in the work of Guo et al. (Ying Guo et al., 2019) who developed a piezoresistive sensor made up of MXene Nanosheets (Qingtao Wang et al., 2019) embedded in tissue paper (Figure 2.8a), which was able to sense pressures of up to 30 kPa (Figure 2.8b), but was only cyclically tested with a pressure of ~3 kPa (Figure 2.8c). Or the nanoporous polymer composite based piezoresistive sensor (Figure 2.8d) developed by Li et al. (Li et al., 2019), which could handle a compressive strain of up to 90% (Figure 2.8e), but was only subject to a strain of 1.5% for the durability test (Figure 2.8f).

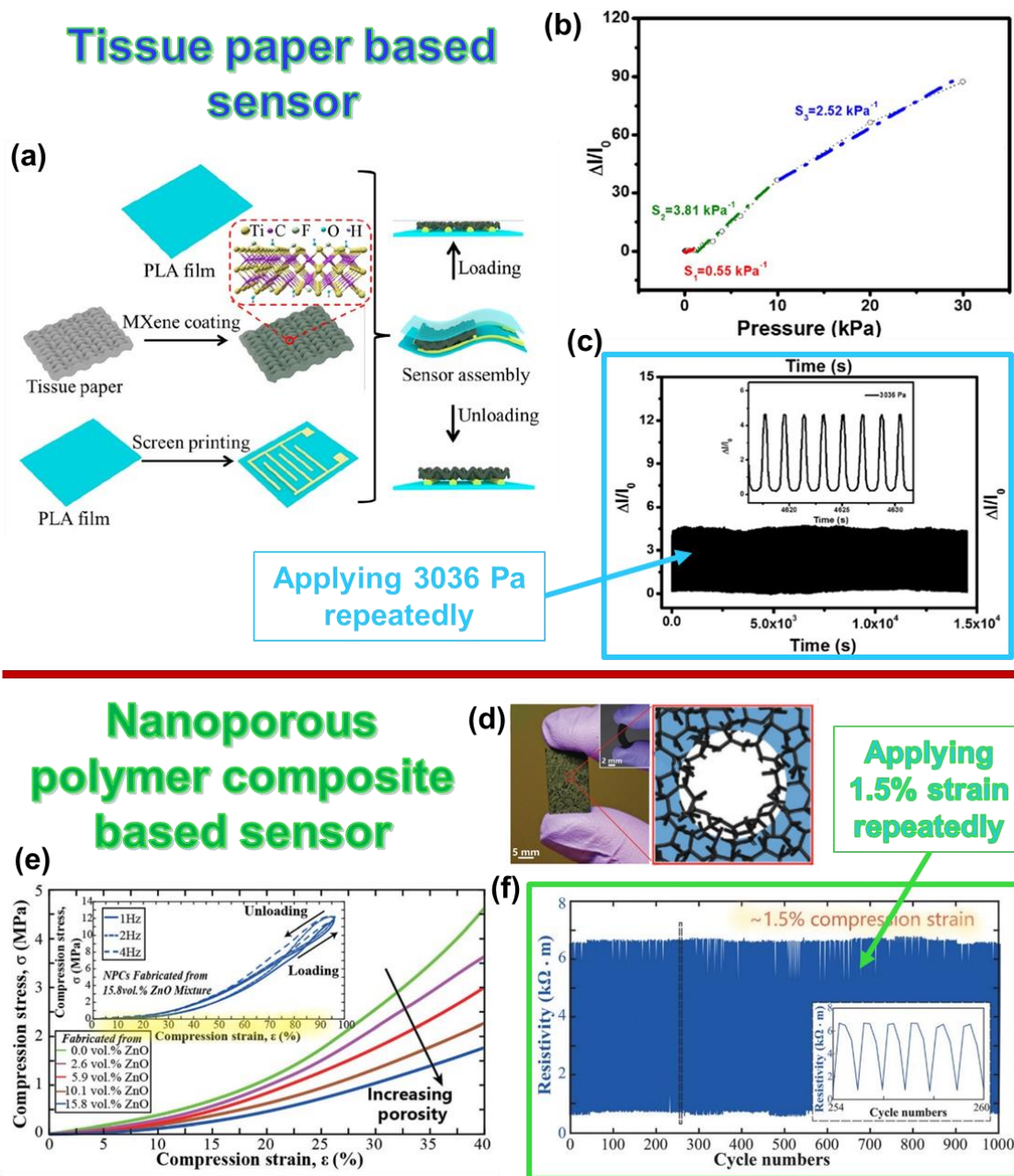


Figure 2.8: Piezoresistive sensors and their stability tests a.) Schematic illustration of the fabrication steps of the MXene nanosheets based flexible pressure sensor b.) Relative current change as a function of applied pressure c.) Durability test by applying a pressure of 3036 Pa repeatedly (Ying Guo et al., 2019) d.) Photograph of a nanoporous polymer composite, inset shows the side of the specimen in bent form and the zoomed image shows a schematic of the nanoscale pore with exposed carbon nanotubes e.) compressive stress-strain curves of the nanoporous polymer composites with increasing volume fraction of added sacrificial ZnO NP, inset shows the loading and unloading of the NPCs fabricated from 15.8 vol% ZnO NPs under different loading frequencies (Li et al., 2019)

Additionally, piezoresistive sensors typically suffer from undesirable drift (Dabling et al., 2012), often require constant power consumption and have high sensitivity to temperature (Muhammad et al., 2011).

2.3.3 Piezoelectric and triboelectric pressure sensing

Piezoelectricity is generated when a piezoelectric material - like a quartz crystal - experiences some mechanical strain (force/pressure). The applied pressure causes the charges - which normally are balanced in crystals – to not be able to cancel each other out and thus the net positive and negative charges appear on opposing crystal faces, creating a potential difference across the opposing crystal faces. Similarly, when a potential difference is applied across the same element, the atoms move to rebalance and this process causes the crystals to deform accordingly (Bunde et al., 1998). With the list of advancements in material science extending, the benefits of (enhanced) piezoelectric materials is also subsequently increasing (Hlinka, 2019). Piezoelectric sensors today offer many benefits including enabling self-powered devices (Wang et al., 2011), ease of processing and low cost implementation (Persano et al., 2013). Materials that have demonstrated piezoelectric capabilities can be divided into naturally occurring and synthetic (organic and inorganic). Examples of such materials include barium titanate (BaTiO_3) (Kang et al., 2015), lead zirconate titanate (PZT) (Tseng et al., 2013) and polyvinylidene fluoride (PVDF) (Shirinov and Schomburg, 2008).

Wang et al. (Wang et al., 2011) fabricated a piezoelectric force sensor based on PVDF fabrics that were electrospun (Figure 2.9a). The sensors demonstrated

excellent sensitivity and response to external mechanical forces (Figure 2.9b). Even the reproducibility of the sensors was good, with samples B and F, that are identical, responding with the same output voltage of 140 mV and sensitivity of 42 mV N⁻¹ (Figure 2.9c).

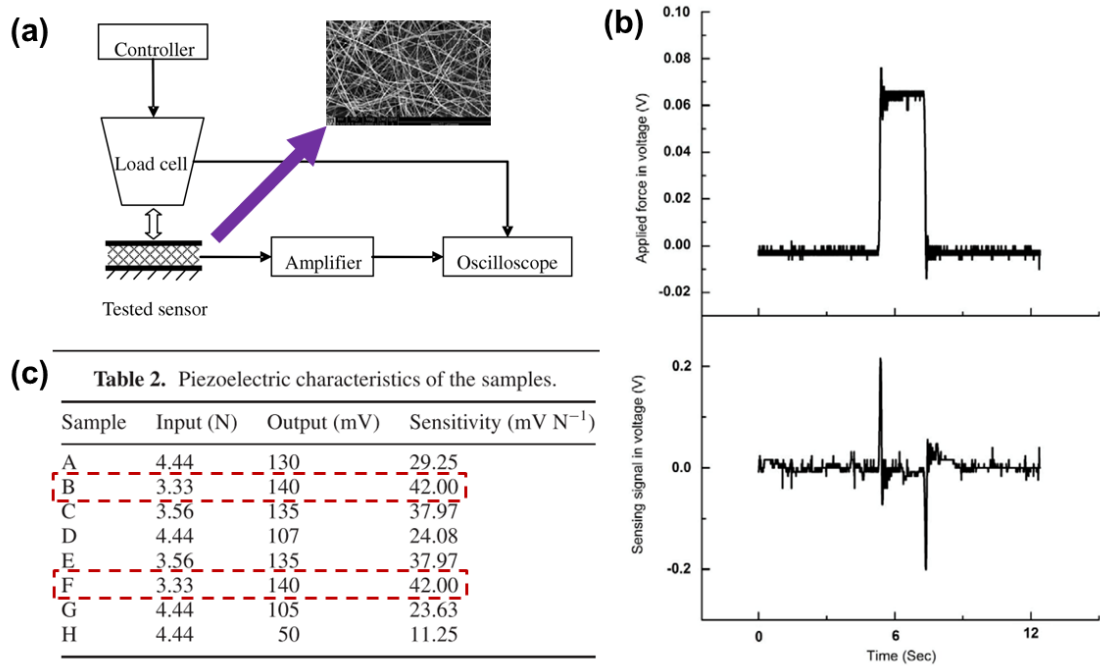


Figure 2.9: PVDF fabric based piezoresistive sensor a.) 4-part setup for characterising the developed PVDF sensors, inset showing SEM of PVDF fabric b.) Piezoelectric characteristics of the different sensor samples c.) Sensor response applying a 3 and 5 N load, where the upper figure shows the load force and the lower figure shows the corresponding electrical signal of the sensor (Wang et al., 2011)

However, PVDF also has pyroelectric properties, which is why piezoelectric sensors based on PVDF need to be shielded from thermal interferences (Shirinov and Schomburg, 2008). Additionally, PVDF films only produce low levels of charge piezoelectrically and thus need an amplification (circuit) in order to make the signal collection procedure simple (Wang et al., 2011) (Figure 2.9a). In terms of inorganic materials, lead zirconate titanate (PZT) is one of the most common piezoelectric materials, due to its good stability and low hysteresis (Dagdeviren et al., 2014). PZT is typically rigid, but can be integrated

into flexible devices by making PZT into very thin films. In general, the main problem with piezoelectric sensors is that they are limited to dynamic measurements since the sensor generated output voltage is impulsive (Shirinov and Schomburg, 2008), thus making static measurements challenging.

The mechanical to electrical energy conversion can also occur due to triboelectrification, where charge is induced due to frictional contact between an electrification layer and an electrode or dielectric layer (Wang et al., 2015), i.e. 2 layers that have different surface electron affinities. Triboelectric nanogenerators (TENG) harvest these charges and pave the way for low power and even self-powered devices, like self-powered pressure sensors (Uddin and Chung, 2016). TENGs have four different modes of operation (vertical contact separation mode, in place sliding mode, single electron mode, free standing triboelectric layer mode) that have been elaborated by Wang et al (Wang et al., 2015) in great detail.

However, since triboelectrification occurs at the interface of the electrification layer and electrode/dielectric layer, the bonding between these two layers has to be good. But in practice, these interfaces can have weak interfacial bonding, because typically one layer (electrode) is hydrophilic and the other layer (elastomer) is hydrophobic (Pu et al., 2017).

2.4 Capacitive pressure sensors

2.4.1 Fundamentals

Capacitors (also known as condensers) are one of the fundamental passive components with two-terminals like resistors and inductors. In their simplest configuration – parallel plate capacitors - they consist of two electrodes that are separated by an insulating medium (dielectric layer) as shown in Figure 2.10a below. They have the ability to store charge between the plates (electrodes) in an electric field. The amount of charge a given capacitor can store is represented by its capacitance, which is measured in Farads. The capacitance C for a simple parallel plate capacitor is governed by:

$$C = \frac{A \times \epsilon_0 \epsilon_r}{d} \quad (1)$$

where A is the overlapping cross-sectional area of the electrodes (m^2), ϵ_0 is the permittivity of free space (8.854×10^{-12} F/m), ϵ_r is the permittivity of the dielectric medium (F/m) and d is the distance between the two conducting plates/electrodes (m), where d_0 is the initial distance between the two electrodes.

Figure 2.10b demonstrates the working principle of capacitive pressure sensing. For a flexible capacitive pressure sensor, where the dielectric medium is a flexible medium (rubber or elastomer), as pressure is applied to the top plate (electrode) of the capacitor, the distance between the plates reduces, thus reducing the distance between the two plates and in turn increasing the measured capacitance across the capacitor. When the pressure is removed, the plates return to their original position and the measured capacitance returns to its initial capacitance value.

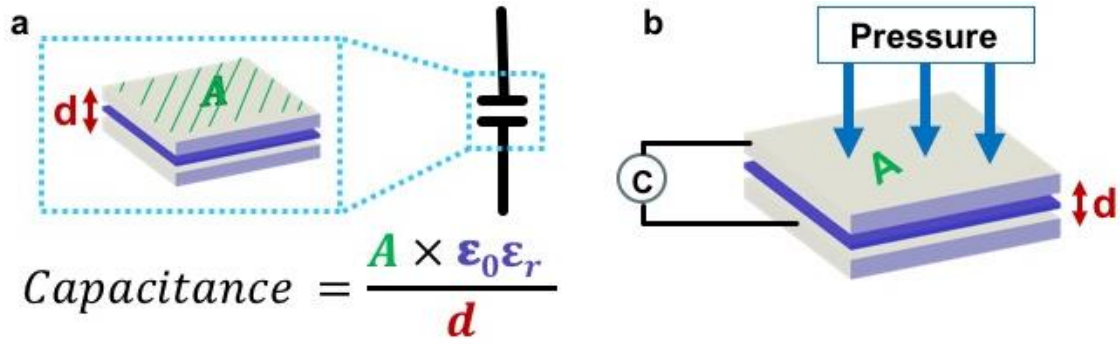


Figure 2.10: a.) Capacitor circuit symbol and schematic of a parallel plate capacitor with the fundamental formula for capacitance b.) Schematic of a capacitor employed as a pressure sensor

In order to measure the pressure sensitivity (S) of a given capacitive pressure sensor with base capacitance of C_0 , the relative capacitance change is given by:

$$\frac{\Delta C}{C_0} = \frac{C - C_0}{C_0} \quad (2)$$

where C is the capacitance measured under an applied pressure (P). Thus the above can be expressed as a function of applied pressure (P), such that the pressure sensitivity (S) can be given as:

$$S = \frac{\delta\left(\frac{\Delta C}{C_0}\right)}{\delta P} = \frac{\frac{\Delta C}{C_0}}{\frac{F}{A}} = \frac{\Delta C \times A}{C_0 \times F} \quad (3)$$

Considering the mechanical aspect to this, the Young's modulus (E) of the dielectric medium is defined as:

$$E = \frac{\text{Stress}}{\text{Strain}} = \frac{\frac{\text{Applied force}}{\text{Force affected area}}}{\frac{\text{Change in Distance}}{\text{Initial Distance}}} = \frac{\frac{F}{A}}{\frac{\Delta d}{d_0}} = \frac{F \times d_0}{A \times \Delta d} \quad (4)$$

Rearranging to make Δd the subject and multiplying by -1 due to the change in distance being a compression results in:

$$\Delta d = -\frac{F \times d_0}{A \times E} \quad (5)$$

Since the change in capacitance is due to the variation in the distance (d) between the two plates, the change in capacitance with respect to the change in distance is obtained by differentiating equation (1):

$$\frac{\Delta C}{\Delta d} = \frac{-A \times \epsilon_0 \epsilon_r}{d_0^2} \quad (6)$$

$$\Delta C = \frac{-A \times \epsilon_0 \epsilon_r \times \Delta d}{d_0^2} \quad (7)$$

Substituting equation (5) into equation (7) gives:

$$\Delta C = \frac{\epsilon_0 \epsilon_r \times F}{d_0 \times E} \quad (8)$$

Substituting equation (8) into equation (3) gives:

$$S = \frac{\frac{\epsilon_0 \epsilon_r \times F}{d_0 \times E} \times A}{C_0 \times F} = \frac{\epsilon_0 \epsilon_r \times A}{C_0 \times d_0 \times E} \quad (9)$$

Rearranging equation (1) we know that:

$$d_0 = \frac{\epsilon_0 \epsilon_r \times A}{C_0} \quad (10)$$

Substituting equation (10) into equation (9) gives:

$$S = \frac{1}{E} \quad (11)$$

Equation (11) defines the pressure sensitivity S for a dielectric layer with Young's modulus E, assuming the Poisson ratio is 0. From equation (11) it becomes clear that in order to increase the sensitivity of a given capacitive

pressure sensor, the dielectric layer should have low Young's modulus. This is why polymers with low Young's modulus like PDMS and Ecoflex are commonly reported as being employed as the dielectric layer of capacitive pressure sensors.

2.4.2 Nanoparticles dispersed dielectric

Nanofillers have been introduced in recent years as an effective way to enhance dielectric properties, especially in low relative permittivity materials such as polymeric dielectric mediums. One main approach is to embed polymers with conductive/semi-conductive nanomaterials – like carbon black (CB) nanoparticles - taking interfacial polarization effects and percolation effects into consideration. Including nanofillers below the percolation threshold in a polymer matrix can enhance the dielectric constant by one to several orders, especially when the dispersion of the nanofillers is good (Achour et al., 2008; Xu et al., 2004). Carbon black (CB) being low in cost, high in electrical conductivity even at low concentrations, low density, etc. is one of the most commonly used fillers for enhancing both electrical and mechanical properties (Matchawet et al., 2016). This is also due to the filler loading level required to enhance the dielectric constant of CB composites being much lower than that of ceramic composites. Additionally, there are different levels of conductivity for different carbon black types. Generally, more conductive CB nanoparticles will lead to a higher overall dielectric constant of the composite (Xu et al., 2004).

Beyond the percolation threshold - ~7 vol% for CB (Matchawet et al., 2016) – a large number of conductive networks will form, leading to a reduction in the overall dielectric behaviour. Thus recent approaches to prevent conductive

networks from forming include core–shell structured nanoparticles, where the nanofillers are coated with metal oxides with high dielectric properties, such as Al_2O_3 , SiO_2 , TiO_2 and Ta_2O_5 that prevent the formation of percolation paths (Chen et al., 2018).

It should be noted that for healthcare applications, the toxicity of the employed materials is of paramount importance. The toxicity of carbon black nanoparticles has been challenging to determine and conclude for over a decade (Fiorito et al., 2006; Mu et al., 2010; Pacurari et al., 2016). Thus the actual use of CB nanoparticles in healthcare devices should be avoided until more is understood. In this work, CB nanoparticles have been used as an effective way to enhance the base capacitance and show proof of concept only (shown in chapter 6). The dielectric medium of the developed medical device prototype in chapter 6 of this work consists of PDMS only.

2.4.3 Porous dielectric

From the ways reported for enhancing the sensitivity of capacitive pressure sensors the solution is to introduce air voids into the dielectric layer such that it is easier to deform it. So for example, for 2 dielectric layers of the same thickness and material, but one layer is a uniform film and the other is an air void containing film, then when the same force is applied to each layer, the air void containing the film layer will undergo a greater deformation than the uniform film layer.

Kwon D. et al. (Kwon et al., 2016a) reported a wearable, flexible, microporous, elastomer based pressure sensor (Figure 2.11). The sensor was based on Ecoflex, with the electrodes consisting of a carbon nanotube – Ecoflex composite and the dielectric being porous Ecoflex. The porous dielectric in comparison to the non-porous dielectric layer gave a 20-fold increase in compressibility. The sensitivities stated were up to 0.601 kPa^{-1} in the low pressure region of $<10 \text{ kPa}$. Additionally, their sensor was able to cover the entire tactile pressure range up to 130 kPa . However, this was enabled due the increased thickness of the dielectric layer being 1 cm high.

Similarly, Chen S. et al. (Chen et al., 2016) blended the PDMS with ammonium bicarbonate for pore creation and made the sensor for even higher pressure ranges covering up to 1 MPa . However, the sensor was low on sensitivity, with sensitivities in the low regions ($<10 \text{ kPa}$) being 0.01 kPa^{-1} . Reproducibility in both reported porous sensors is low, since the pore location and size inside the dielectric could not be controlled.

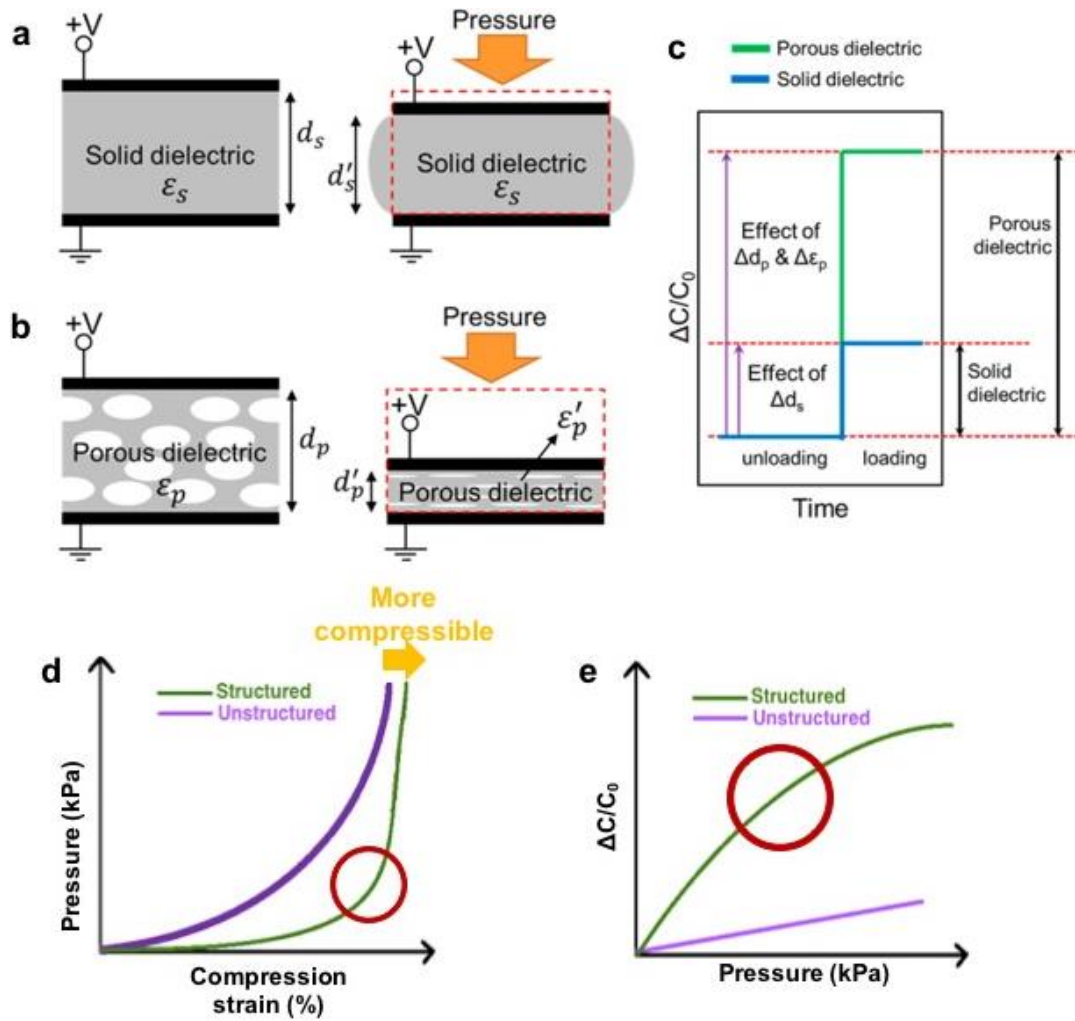


Figure 2.11: a.) Schematic of a capacitive pressure sensor with solid dielectric medium and its compressed state with applied pressure b.) Schematic of a capacitive pressure sensor with a porous dielectric medium and its compressed state (showing increased compression due to micropores) c.) Enhanced relative capacitance change for a porous dielectric medium in contrast to a solid dielectric d.) Applied pressure VS compression strain showing that a porous dielectric medium is more compressible than the solid dielectric medium e.) Enhanced relative capacitance change for a porous dielectric medium in contrast to a solid dielectric medium (Kwon et al., 2016a)

The disadvantages of porous dielectric media are that for most of the reported porous capacitive pressure sensors the pore sizes and locations are random, so that the deformation of the sensor and in turn the sensitivity of the sensor is challenging to reproduce and control.

2.4.4 Structured dielectric

If the dielectric material is shaped into different structures so that the air voids are engineered in place, then the deformation of such microstructured dielectric layers would be more controlled, which enables control of the sensitivity of the sensor.

Mannsfeld et al. (Mannsfeld et al., 2010) demonstrated microstructuring of thin ($< 100 \mu\text{m}$) films of the biocompatible elastomer PDMS into pyramidal structures using silicon moulds. The pyramid shape (V) containing silicon moulds was micropatterned by photolithographically using a $\langle 100 \rangle$ silicon wafer with a 300 nm thermally grown silicon oxide layer. This was followed by chemical anisotropic etching using potassium hydroxide (KOH) and removing the remaining silicon oxide using buffered hydrofluoric acid. It should be noted that the sidewall angle – the angle between any of the 4 side walls and the base of the pyramid – was always 54.7° due to the etch rate being different for the different silicon crystallographic planes with KOH .

The fabricated silicon mould was exposed to a vapour deposition of (tridecafluoro-1,1,2,2,-tetrahydrooctyl)trichlorosilane to facilitate the release of the PDMS moulding from the mould. PDMS was prepared, diluted with Hexane (10:1, Hexane:PDMS) and casted onto the micropatterned silicon mould. The mould and the solution were degassed in a vacuum chamber for 30 minutes, so that the diluted PDMS solution filled the pyramidal air voids in the silicon moulds. A Polyethylene terephthalate (PET) film of $150 \mu\text{m}$ thickness was deposited with indium tin oxide (ITO) and then ultraviolet-ozone treated for 20

minutes. This flexible electrode was then placed and clamped on top of the degassed PDMS solution on the mould with a pressure of >100 MPa at a temperature of 70 °C. After a minimum of 4 hours of curing, the microstructured PDMS film with the attached PET/ITO electrode was demoulded (Figure 2.12a (i-iv)). A mechanical stage and a force gauge were used to apply loads (pressure) to the sensor. The capacitance change was measured using a LCR meter. The pressure response for 3 types of PDMS films was obtained. The first type being an unstructured PDMS film and the other 2 types being structured PDMS films of $6\text{ }\mu\text{m} \times 6\text{ }\mu\text{m}$ pyramids and lines (Figure 2.12b (i, ii)). The pyramidal structured PDMS film gave the highest sensitivity of 0.55 kPa^{-1} in the low pressure region $<0.2\text{ kPa}$. This was ~ 30 times higher than the unstructured PDMS film. This was possible because the pyramidal structures gave less resistance to deformation when a pressure was applied onto the sensor than a line structured or unstructured PDMS film, so that the effective Young's modulus of the whole dielectric layer is lower for the pyramid based film than the line structured based film and both of which are lower than the unstructured film. However, due to the height of the pyramids being $6\text{ }\mu\text{m}$, the pressure range was limited to 7 kPa . In order to demonstrate the capability of the sensor to detect low pressure, a bluebottle fly (20 mg) was placed and removed on top of the sensor, which had an area of $8 \times 8\text{ mm}^2$, so that the applied pressure was only $\sim 3\text{ Pa}$ (Figure 2.12c). Similarly, when a pressure of 15 kPa was applied to the sensors, then the unstructured sensors showed a relaxation time of more than 10 seconds, whereas the structured (pyramids and lines) sensors showed an enhanced relaxation time of under 1 second (Figure 2.12d). In particular, the pyramid film based sensor showed a response time of $\sim 356\text{ ms}$ and a relaxation time of $\sim 413\text{ ms}$. This was considered fast ~ 9 years ago, but more

recent evidences in microstructured capacitive pressure sensor development have reduced the response and relaxation time by an order of magnitude, where groups are reporting response and relaxation times as low as 20 ms (Zhang et al., 2017).

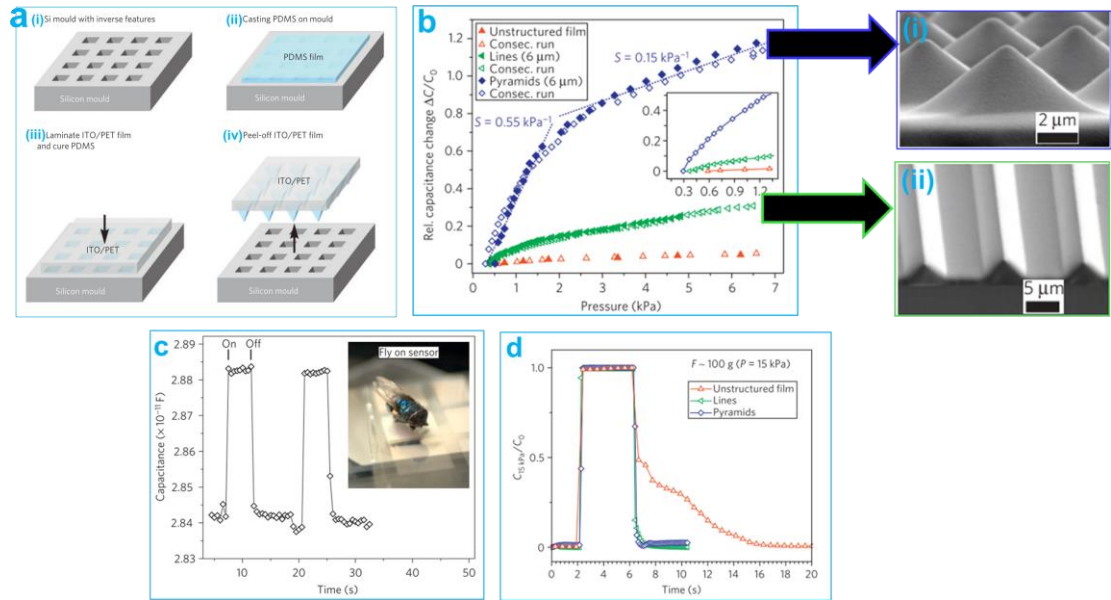


Figure 2.12: Microstructuring PDMS film into lines and pyramids a.) Schematic process for the fabrication of microstructured PDMS films. (i) A dilute solution of the PDMS mixture of base and cross-linker in hexane is drop cast onto a Si wafer mould (ii) containing arrays of the inverse of the features to be replicated (iii) The PDMS film is vacuum-degassed and partially cured. An ITO-coated PET substrate is laminated to the mould, and the PDMS film is cured under pressure at a temperature of 70 °C for at least 4 hours (iv) Peeling the cured flexible substrate off the mould b.) Pressure response curves for 3 types of PDMS films, one being an unstructured film and the other 2 types being structured with (i) pyramids and (ii) lines c.) Response and relaxation time for the 3 types of PDMS films after loading and unloading of 15 kPa for 4 seconds d.) Response and relaxation time for loading and unloading a bluebottle fly on the 8 x 8 mm² sensor (Mannsfield et al., 2010)

A few years later Tee B. et al (Tee et al., 2014) demonstrated the use of the photolithographically made silicon mould as a template for making soft lithography moulds made up of PDMS. These PDMS soft moulds were then treated with UV plasma and trichloro-fluorosilane to facilitate demoulding. The soft moulds were then filled with PDMS and cured as before. The

microstructured PDMS film was peeled off the soft mould Figure 2.13a (i-iii)). It should be noted that the soft mould would need to be retreated with UV plasma and trichloro-fluorosilane before the next moulding process. These elastomeric stamps are an enhancement for microstructured films because of their flexibility such that they are able to wrap around objects, which enable the moulding to cure and fixate even in a flexed position. Additionally, the elastomeric stamps are less prone to drastic failure due to their elasticity in contrast to the brittle silicon moulds. However, the demoulding of flexible moulds can be more challenging since you are peeling off a flexible moulding from a flexible mould, where extensive strain could lead to permanent deformations or even rupture. This is in contrast to peeling off a flexible moulding from a rigid moulding, where the peeling only adds strain on the moulding. The group (Tee et al., 2014) then showed how, using their fabrication approach they were able to make pyramidal microstructured PDMS films, with pyramids of heights of $\sim 20\text{ }\mu\text{m}$ and different inter-pyramid spacings (edge to edge) ranging from $41\text{ }\mu\text{m}$ to $182\text{ }\mu\text{m}$. The bigger the spacing the bigger the sensitivity of the sensor, so that the sensor with the biggest inter-pyramid spacing of $182\text{ }\mu\text{m}$ gave the highest sensitivity (Figure 2.13b (i, ii)). This was because, for an applied pressure, the deformation of the dielectric layer is highest when there is less support. There was less support since for a given electrode area, the number of pyramids is limited, so that, with an increase in inter pyramid spacing, the number of pyramids in the electrode area will reduce, leading to less support. This results in more deformability, but a lower base capacitance, because the dielectric layer has more air in it, which has a lower dielectric constant (~ 1) (Hector and Schultz, 1936) than PDMS (~ 2.7) (Dow corning, 2014). The maximum pressure applied was $\sim 21\text{ kPa}$, which was ~ 3 times higher than the maximum pressure of 7 kPa

that was applied to the sensor of Mannsfeld et al (Mannsfeld et al., 2010), whose pyramid heights were about ~3 times smaller (6 μm) than the 20 μm high pyramids of Tee et al.. This shows that there is a close relationship between pyramid height - the dielectric layer thickness - and pressure range. The group (Tee et al., 2014) also showed via simulations that the sensitivity is higher with an increase in inter-pyramid spacing and also with a lower side wall angle. The lowest side wall angle they simulated was 54.7 °C, which is also the sidewall angle that is obtained when etching the microstructure into <100> wafer with KOH (Figure 2.13c).

Similarly, Boutry et al. (Boutry et al., 2015) used the same soft lithographic moulding approach to fabricate a sensitive and fully biodegradable flexible capacitive pressure sensor array for cardiovascular monitoring. The biodegradable elastomer they used was poly(glycerol sebacate) (PGS) (Figure 2.13d). The sensor was able to successfully measure the blood pulse waves of the radial, femoral and carotid artery of a volunteer. In fact, the sensor successfully measured the wrist pulse wave even under different skin conditions, like a dry, slightly wet and a completely wet skin area (Figure 2.13e (i-iii)).

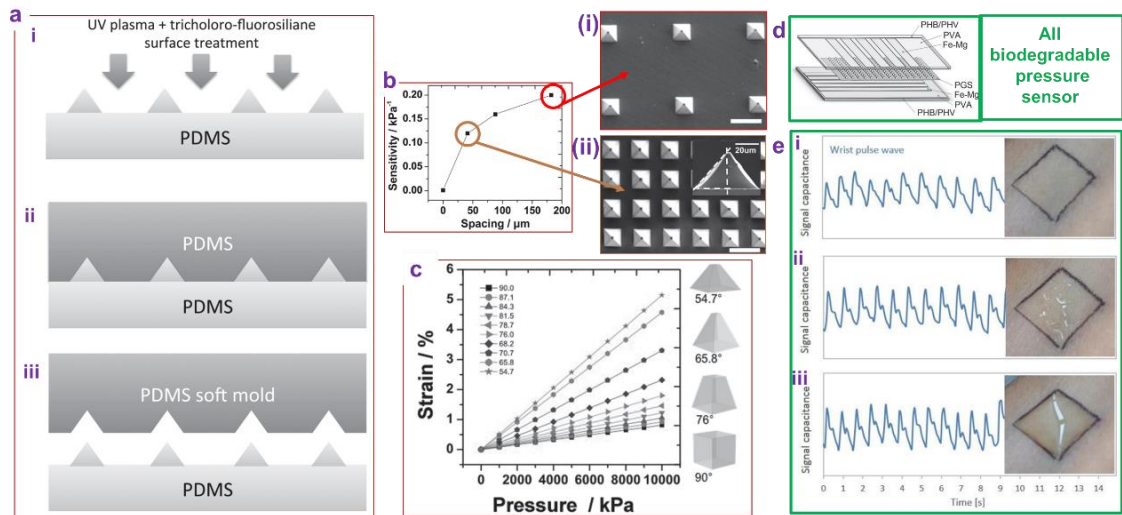


Figure 2.13: PDMS soft mould and all biodegradable pressure sensor a.) Schematic of a soft lithographic process for making PDMS soft mould (i) Treating the surface of PDMS mould after the first feature replication step from silicon (ii) Pouring PDMS over the treated surface of PDMS mould and cure to complete (iii) Removing the PDMS soft mould and treating with fluorosilane again to use for subsequent feature replications b.) Sensitivity values plotted with spacing distance of the microstructures for pressure values less than 4 kPa (i) Scanning Electron Microscope (SEM) of 182 μm spacing and (ii) 41 μm spacing c.) Simulation data showing the predicted stress-strain relationship of different sidewall angled microstructures (Tee et al., 2014) d). Schematic of a fully biodegradable and flexible pressure sensor array from microstructured poly(glycerol sebacate) PGS films e.) Measuring a wrist pulse wave when the sensor is placed on top of (i) dry skin, (ii) wet skin and (iii) when the skin is fully covered with artificial sweat (Boutry et al., 2015)

The flexible and transparent electrodes of capacitive pressure sensors are primarily made of a thin indium tin oxide (ITO) layer coated onto a flexible substrate like PET. This is primarily because of ITO's great optical and electrical properties (López-Naranjo et al., 2016). However, ITO is scarce and expensive (Kulkarni et al., 2015), which is why some groups have demonstrated capable alternatives. Luo et al. (Luo et al., 2018) showed the making of transparent graphene electrodes for capacitive pressure sensing. The graphene was grown via a chemical vapour deposition method and then transferred onto PET. Other groups like Shuai et al. (Shuai et al., 2016) cast silver nanowires (AgNWs) onto a silicon substrate and then poured PDMS above it to form a flexible AgNW

embedded PDMS electrode. They then used a photolithographically microwave patterned silicon mould to mould a microstructured PDMS moulding via spin coating. The cured AgNW embedded PDMS electrode was then placed above the spin coated PDMS so that the flexible electrode and microarray dielectric layer cure as one part (Figure 2.14a).

The microstructured dielectric layer facilitates rapid deformation of the dielectric layer, which results in a rapid change in the electric field between the two parallel plates. Similarly, microstructuring a flexible electrode instead of the dielectric layer would also empower deformation (Figure 2.14d) as demonstrated by another work by Shuai et al. (Shuai et al., 2017a), where a microarray mould was made by stretching a PDMS film and this was then treated with plasma of dry low pressure air, which consequently buckled the PDMS film during relaxation. Filtered AgNWs out of ethanol were transferred onto the PDMS film. Another PDMS mixture was spin coated onto the AgNW film containing buckled PDMS film and cured at 70 °C for 2 h. The AgNW's film embedded microstructured PDMS electrode film was peeled off the elastomeric mould. The dielectric layer in this case was a spin coated layer of high dielectric constant (~ 9) (Li et al., 2011) polyvinylidene fluoride (PVDF) (Figure 2.14b). The sensor showed a high sensitivity of 2.94 kPa^{-1} in the low pressure region of $<1.5 \text{ kPa}$, but there was a clear trade-off between sensitivity and pressure range as can be seen in Figure 2.14c, where, for a thin $1.6 \text{ }\mu\text{m}$ layer of PVDF, the sensitivity was the highest, but the entire pressure range was only up to $\sim 3.9 \text{ kPa}$. For the thickest dielectric layer of $13.5 \text{ }\mu\text{m}$, the sensitivity was lowest, but the pressure range was up to 10.8 kPa . However, a thin dielectric layer would be easily destroyed when a large pressure is applied and a thick dielectric layer would have lower sensitivities. This is why the group took a compromised

dielectric layer thickness of $3.5\ \mu\text{m}$, which resulted in a high sensitivity of $2.94\ \text{kPa}^{-1}$ in the low pressure region of $<2\ \text{kPa}$ and a sensitivity of $0.75\ \text{kPa}^{-1}$ for $>2\ \text{kPa}$.

Other groups like Cui et al. (Cui et al., 2017) sandwiched polystyrene (PS) beads as the dielectric layer between two photolithographically microstructured electrodes. The concept here being that the PS beads contribute to more deformation when a pressure was applied (Figure 2.14e (i, ii)).

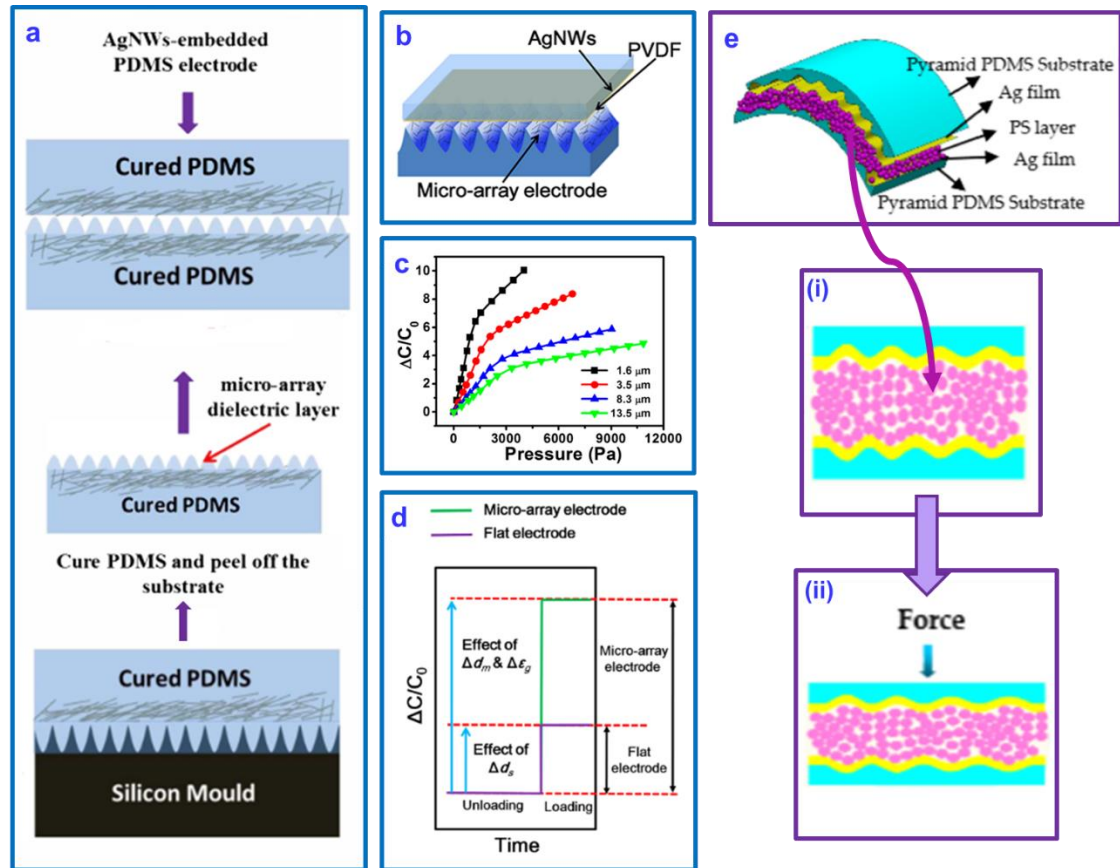


Figure 2.14: Microarray dielectric layer and microstructured flexible electrodes a.) Fabrication process of the micro-array dielectric layer capacitive pressure sensor. The AgNW's embedded PDMS electrode is laminated onto the micro-array dielectric layer (Shuai et al., 2016) b.) A flexible pressure sensor integrates the top electrode, dielectric layer, and microarray electrode in a sandwich structure c.) Effect of PVDF dielectric layer thickness on the sensor response d.) Relative capacitance response of flat sensor and microarray electrode sensor for the same applied pressure (Shuai et al., 2017a) e.) Schematic of flexible capacitive pressure sensor with a dielectric layer consisting of polystyrene (PS) microspheres (i) Schematic side view of the sensor without any force applied and (ii) with a force applied (Cui et al., 2017)

Zhuo et al. (Zhuo et al., 2017) pioneered an acrylonitrile butadiene styrene (ABS) mould (in 3D printing) using a commercial 3D printer (UP Plus 2 from Tiertime, Figure 2.15a), which was used as the template for microstructuring PDMS films into microgrooves (Figure 2.15b). But the resolution was limited to 400 μm due to the limitation of the commercial printer (Figure 2.15c (i)). Additionally, the use of ABS required a heated print head and pre-heated surface.

The range and sensitivity were amongst the lowest reported, with the range reaching just under 4 kPa and the sensitivity being 0.05 kPa⁻¹ (Figure 2.15d). However, the sensor was good enough to detect and real-time monitor wrist pulse (radial artery) wirelessly (Bluetooth) on a mobile phone. For this a self-designed data acquisition (DAQ) board was attached to the sensor for acquiring and transmitting data to the mobile phone (Figure 2.15e (i)). Similarly, Peng et al. (Peng et al., 2018) used 3D printing to print the equivalent of the pyramidal silicon mould without the need for a clean room or expensive tools and equipment (Figure 2.15f). However, the printed moulds had structure sizes that were relatively big ~ 1 mm, due to avoiding rupture of the moulding during the demoulding process. The group did not show the effect of their fabrication approach on capacitive pressure sensing, but instead only focused on resistive pressure sensors.

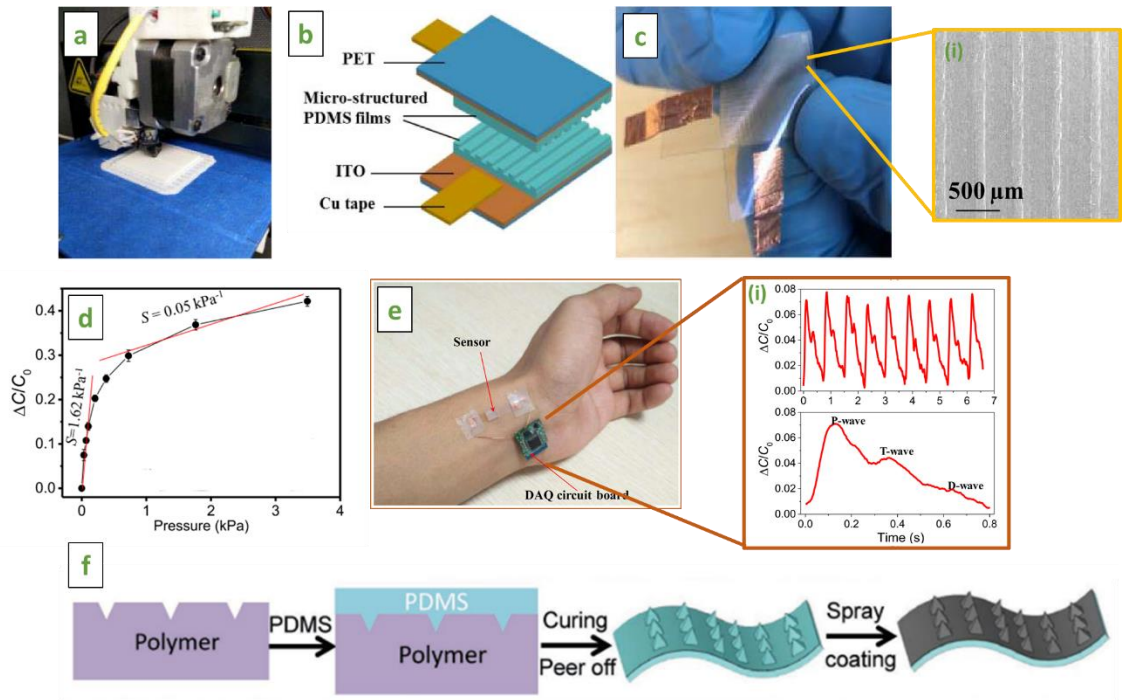


Figure 2.15: 3D printing of a microstructured mould a.) Image of printhead of the 3D printer (UP Plus 2 from Tiertime) being used for fabricating an acrylonitrile butadiene styrene (ABS) based mould b.) Schematic of the fabricated capacitive pressure sensor c.) Photograph of the sensor (i) SEM showing the surface structure of the PDMS moulding d.) Relative capacitance response of the developed sensor e.) The whole sensor system, composed of the pressure sensor and the self-designed data acquisition (DAQ) circuit board, is placed on the radial artery at the wrist, and fixed by transparent adhesive tape for real-time monitoring of wrist pulse. The sensor has dimension 0.7 cm × 0.7 cm (i) The real-time measured wrist pulse waveform with relative capacitance change (upper), and the details of the pulse wave in one period (bottom), which contains the percussion wave (P-wave), the tidal wave (T-wave), and the diastolic wave (D-wave) (Zhuo et al., 2017) f.) Fabrication of conductive microstructured PDMS thin films using a 3D printed structured mould (Peng et al., 2018)

Ruth et al. (Ruth et al., 2019) introduced a lamination layer in order to enable application specific structured dielectric media. The improved fabrication method involved partially curing a PDMS layer onto an ITO/PET electrode, so that this layer served as a place where the pyramid tips can be anchored so that there was more adhesion between the microstructures (pyramids) and the electrodes (Figure 2.16 (a-f)). Additionally the group showed experimentally how varying the thickness of the lamination layer did not affect the initial sensitivity of the sensors, which demonstrated reproducibility of the sensors,

since this showed that the sensors with the different thicknesses of lamination under the same amount of deformation on the pyramidal structures.

Yang et al. (Yang et al., 2019) recently reported microstructured sensors based on porous pyramids. This was achieved by blade coating the photolithographically made silicone moulds with a solution containing polystyrene beads ($\sim 2\text{ }\mu\text{m}$) and spin coating PDMS onto the mould. This filled mould was cured under an applied pressure. The cured moulding was cut and peeled off the mould. The moulding was immersed in toluene so that the polystyrene beads would dissolve away and leave behind porous pyramids with a porous base layer (Figure 2.16g, h). In comparison to the non-porous pyramid dielectric layer the porous pyramid dielectric layer demonstrated an increased sensitivity (Figure 2.16i). However, due to the porous nature of the pyramids, the stability of the dielectric layer to repeated pressure is not the same as for very porous film dielectrics mentioned in the previous section. This is why the group only applied a relatively low pressure of 400 Pa for the stability test, where the sensor showed a stable response for over 5000 cycles (Figure 2.16j).

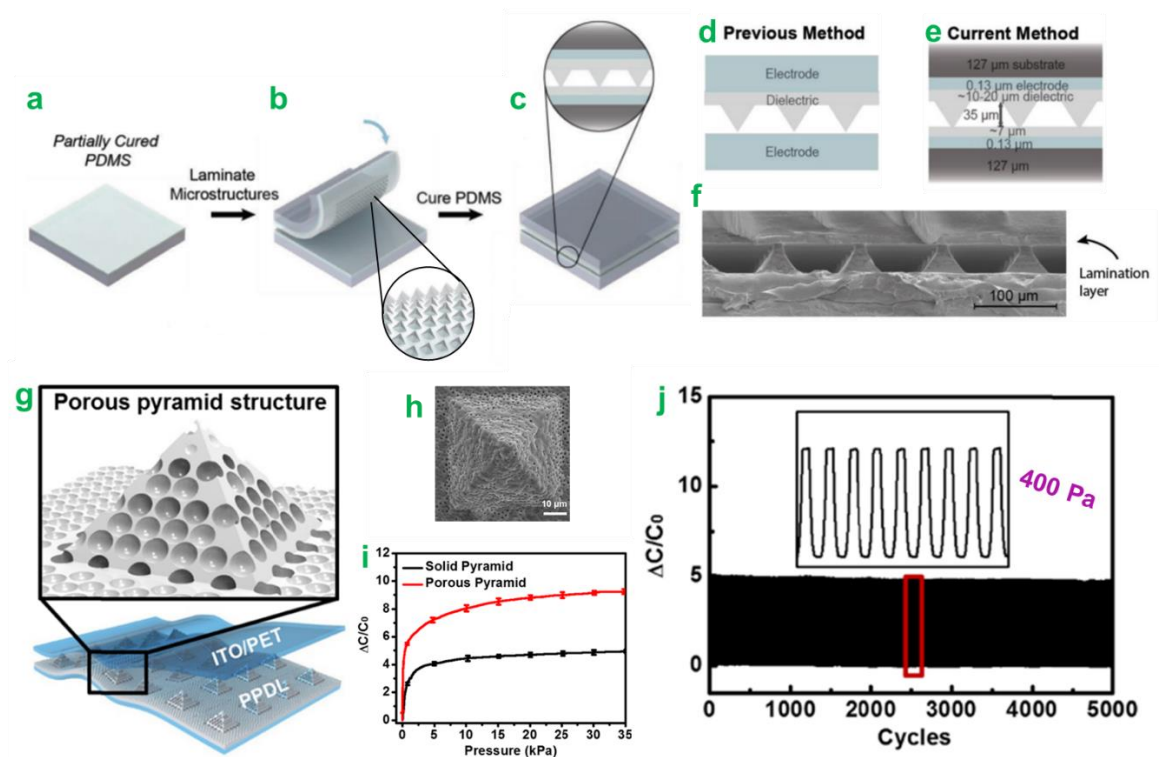


Figure 2.16: Lamination layer for stability and porous pyramids a.) A 3D printed microstructured mould a.) Partially cured PDMS layer which will be the lamination layer of the sensor b.) Slightly anchoring the cured microstructures with the tips facing the partially cured PDMS layer c) Curing the entire sensor d.) comparison between the previous method which had no lamination layer and e.) the current method f.) Scanning electron microscope (SEM) cross-sectional image shows the microstructured pyramids and lamination layers (Ruth et al., 2019) g.) Schematic diagram of the porous pyramid dielectric layer h.) SEM of the top view of the porous pyramid and base layer i.) relative capacitance response to pressure for a porous pyramid dielectric layer and a solid (non-porous) pyramid dielectric layer j.) relative capacitance response to 5000 cycles of applying 400 Pa (Yang et al., 2019)

The main methods for microstructuring the dielectric layers of flexible capacitive pressure sensors over the last decade can be divided into two groups; using photolithographically made silicone moulds and more recently using 3D printed moulds for microstructuring (Figure 2.17). Besides these two approaches, a few groups such as Shuai et al. (Shuai et al., 2017a) have reported using treatment of plasma of dry low-pressure air to buckle the AgNWs embedded PDMS electrode layer, but were limited to ridge structures that undergo less deformation than individual pyramids (Mannsfeld et al., 2010).

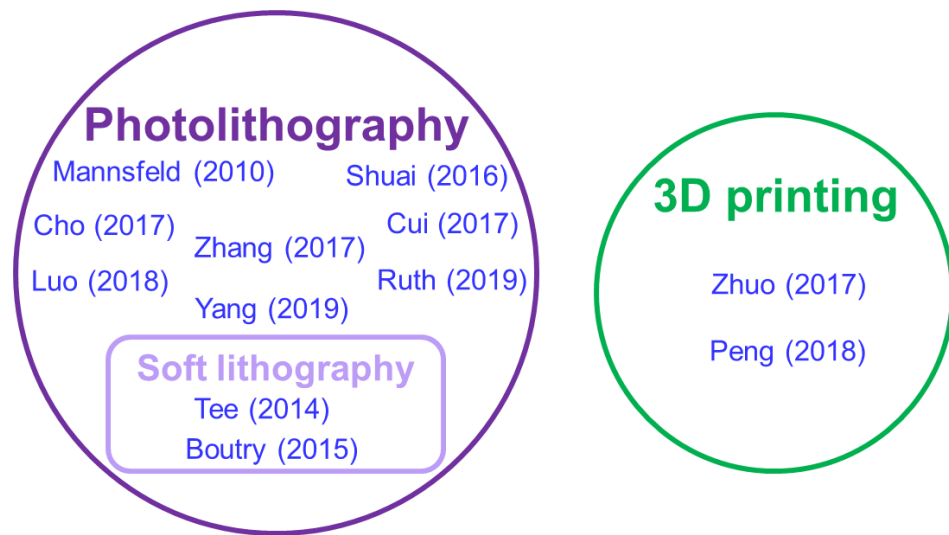


Figure 2.17: Photolithography and 3D printing of pyramidal moulds

2.5 Methods of manufacture

2.5.1 Photolithography

Photolithography (subtractive manufacturing) has been widely used in many industries including the microelectronics industry (e.g. integrated circuits), the biomedical engineering industry, etc. The fundamental principle of photolithographic techniques is using electromagnetic radiation with increasingly shorter wavelengths and a photomask to expose multiple layers of a thin optically-sensitive chemical (polymer resist films) to get etched and leave behind patterned structures (Mojarad et al., 2015).

However, this technique requires the surface of the target substrate to be as flat as possible. Additionally, a sequence of chemical treatments (for etching, etc.) is required, operating at fixed temperature ranges with very clean fabrication environment conditions (often clean rooms), making rapid prototyping/manufacturing – especially for higher resolutions - challenging and expensive.

2.5.2 3D printing

3D printing (additive manufacturing) is a way to fabricate 3 dimensional objects in an additive process, meaning that the objects are fabricated layer by layer using different 3D printing techniques. Most 3D printing methods - in particular for high-resolution ($<10\text{ }\mu\text{m}$) 3D printing - are forms of direct-write (DW) techniques. DW can be defined as '*any technology that can create two/three dimensional functional structures directly onto flat or conformal surfaces in complex shapes, without any tooling or masks*' (Abraham and Helvajian, 2004; Mortara et al., 2009). The next chapter highlights the fundamental science behind small-scale fluidics in high-resolution 3D printing, mainly adopted from (Fang and Aabith et al., 2017).

Chapter 3 - High-resolution 3D printing

This chapter focuses on forms of high-resolution 3D printing techniques and highlights the importance of careful ink formulation for effective direct-write printing. This chapter forms the second part of the literature review of this thesis and has been largely adopted from a published book chapter (Fang and Aabith et al., 2017).

3.1 Additive instead of subtractive manufacturing

The micro/nanomanufacturing needs of many sectors such as the microelectronic industry are broadly met with the use of photolithographic techniques, which work by selectively exposing multiple layers of thin polymer resist films to electromagnetic radiations to fabricate high resolution structures. Nonetheless, these resist-based manufacturing techniques are 'subtractive' and wasteful, since most of the materials used in the fabrication process end up getting dissolved/wasted in the etching stage (Williams et al., 2002).

3.2 Forms of high-resolution 3D printing

3.2.1 3D direct laser writing

The direct laser writing (DLW) technique offers direct scaffolding of photosensitive materials from the microscale down to resolutions as low as sub-100 nm (Selimis et al., 2015). It is based on a non-linear two-photon absorption process that induces photo polymerisation (Figure 3.1a). DLW is a more controlled alternative to exposing certain polymer materials to UV-light. This is due to an ultra-fast laser beam (with high light intensity and short pulse length) that is focused into the volume of certain polymers or resins, which results in the

two-photon polymerization to only occur in the focused point and volume (Figure 3.1a). This precise control enables smooth finishes in most resins and particularly suitable polymers. Klein et al. (Klein et al., 2011) fabricated polymer scaffolds with protein-repellent features for cell culture studies. The base structure consisting of polyethylene glycol diacrylate (PEG-DA) – that is protein repellent - was fabricated using DLW (Figure 3.1b). Using a biocompatible photoresist Ormocomp, small protein binding cubes were added to the framework with another direct laser writing step (Figure 3.1b).

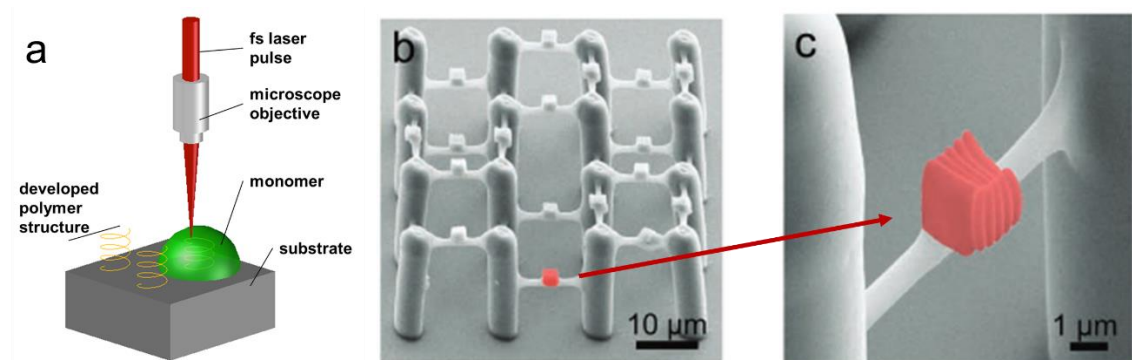


Figure 3.1: a.) Schematic illustration of 3D direct laser writing. b.) Direct laser written protein-repellent PEG-DA framework and c.) photoresist Ormocomp cubes precisely placed (Klein et al., 2011)

3.2.2 Focused ion beam

The focused Ion Beam (FIB) writing approach offers imaging and efficient milling, deposition and etching capabilities at the microscale and nanoscale level. Thus it has started to play an important role in fundamental materials' studies and advanced technological applications (Volkert and Minor, 2007). The technique is similar to the Scanning electron microscopy (SEM) technique, which uses an electron beam to image at high resolution. FIB uses an ion beam which upon contact with the surface sputters a small amount of material and comes off as ions or neutral atoms (Figure 3.2). The ions that come off the

surface can be collected for imaging, but the technique's imaging abilities with Gallium ions are limited to ~5nm due to sputtering and detector capabilities (Orloff, 1996). FIB devices are typically equipped with SEM to help in imaging, but primarily for charge neutralisation. FIB enables maskless ion implantation, where an ion beam is scanned over a desired area to achieve ion implantation or surface functionalisation, which brings many advantages to the semiconductor processing technology sector, such as lateral impurity control.

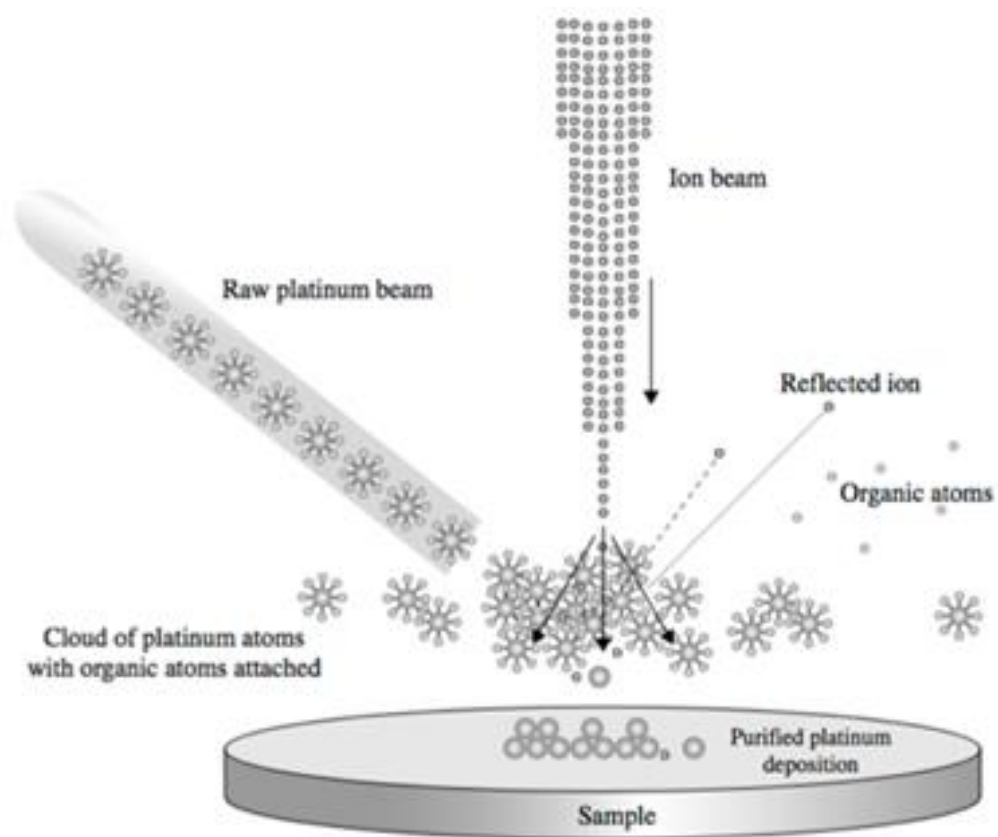


Figure 3.2: FIB setup with a gas injector for platinum deposition (Yao, 2007)

3.2.3 Direct-write printing

Direct-write printing in essence is pneumatically forcing – via compressed air - rationally formulated inks through custom-tapered microscale capillaries. The nozzles are maintained close to the surface of the substrate to be printed on, so that the extruded ink is able to make a fluid contact between the nozzle and the substrate. Nanopositioning stages with nanometre step sizes are controllably moved to have features printed on top of the substrate, layer by layer (Figure 3.3). Essentially it can be seen as having a stationary pen (nozzle) and the paper (substrate) is moved to get written (printed) on top off. All of this is observable via a co-positioned microscope. The diameter of the nozzles can be as small as a few nm and is a key factor in determining the final print resolution.

Many inks for direct-write printing have been reported, ranging from colloidal suspensions to various polymer based inks, which demonstrates the versatility of the direct-write printing approach (Ahn et al., 2009). The resourcefulness of the direct-write printing approach and its many other benefits (Lewis et al., 2006) have made it the high-resolution 3D printing approach that has been employed in this work.

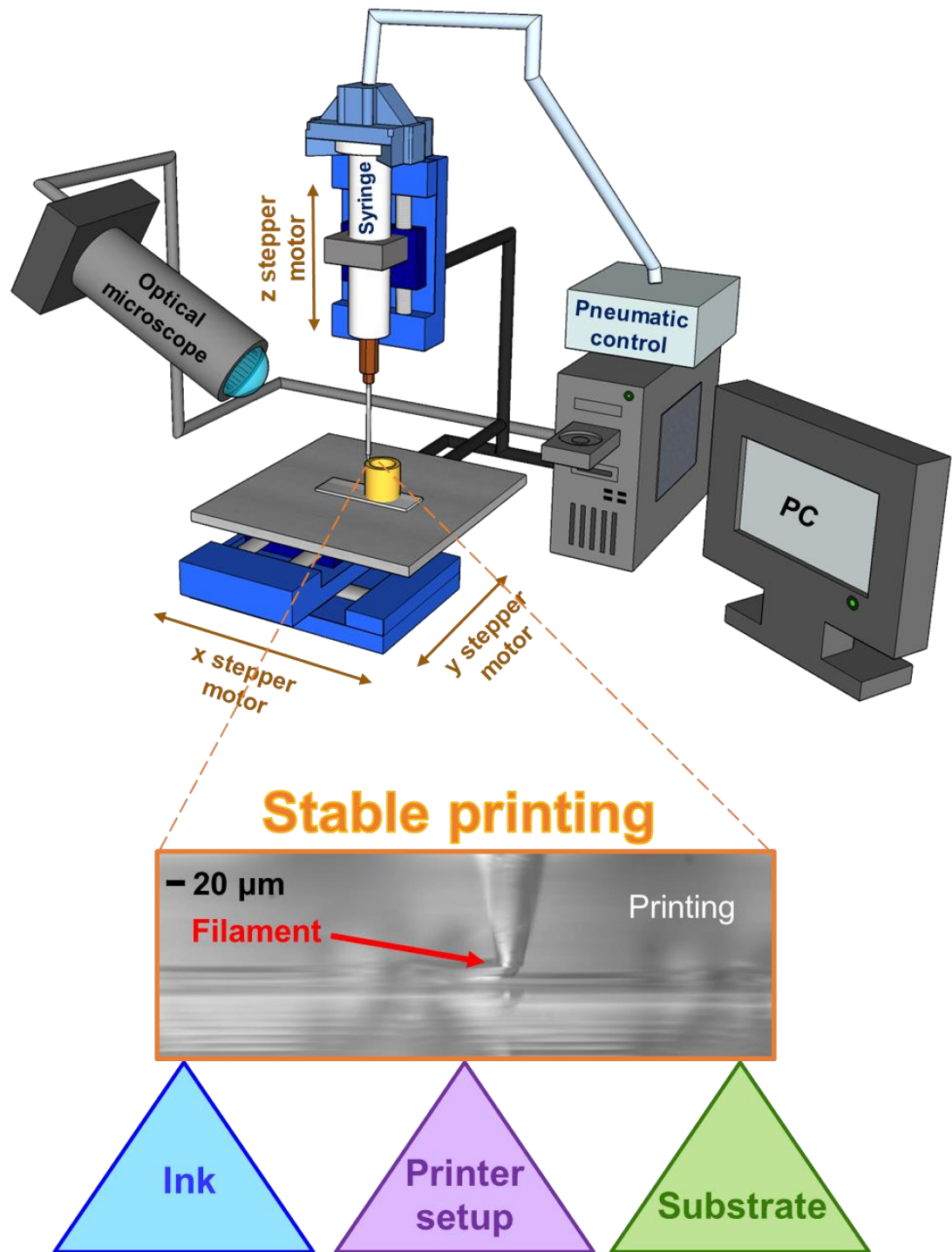


Figure 3.3: Schematic of the direct-write assembly approach printing setup and the main printing parameters governing print resolution and print quality

3.3 Ink properties

Fluid mechanics plays a fundamental role in many high-resolution 3D printing techniques including 3D direct-write printing. This means a good understanding of small scale (micro/nanoscale) fluidics is essential for effectively implementing and controlling these techniques for this project and beyond.

Micro/nanofluidics is the study of fluid and flow systems with a characteristic dimension ranging from 1 nm to 100 μm . Volumetric entities in such systems typically range between 10^{-9} and 10^{-18} L (Eijkel and van den Berg, 2005; Schoch RB, Han J, 2008; Whitesides, 2006).

The Reynolds number (R_e) is a non-dimensional parameter, which can be used to predict the fluid flow characteristics by comparing the relative effects between fluid inertial and viscous stresses. It can be expressed as:

$$R_e = \frac{\rho v L}{\mu} \quad (1)$$

where for a characteristic length scale L (the diameter of the tip aperture in the direct-write print assembly) ρ , v and μ are the density, the mean velocity and the dynamic viscosity of the fluid (ink), respectively. The diameter of the tip aperture is directly related to the printing resolution. For high-resolution printing, the tip aperture is usually in the sub-micrometre to 500 μm range, so that the Reynolds number is very small, much less than 1.

For low Reynold numbers (<1) viscous forces dominate over inertial forces which leads to regular/laminar flow patterns. This is similar to the predominantly laminar flows encountered in microfluidics (Tabeling, 2005). Thus a good understanding and control of viscous stresses for stable printing operation is necessary.

Viscosity and viscous stresses are only parts of 'rheological' properties of fluids, that encompass all flow properties relating to fluid deformation rate (flow) with fluid stresses. Moreover, the printing process and resolution are also strongly dependent on the wettability (liquid affinity) of the nozzle and the printing substrate, and the evaporation rate (vapour pressure) of the ink solvent as summarised in Figure 3.4. These factors are strongly interlinked and a careful balance of these factors needs to be established for every new ink that is to be direct-write printed. For example, targeting high-resolution printouts ($<10\text{ }\mu\text{m}$) with fine tip sizes will result in a higher evaporation rates, which will alter the time needed for the extruded filament to adhere to the substrate, which in turn will have a certain amount of affinity to the extruded filament material. For more details on ink viscosity, the flow through capillaries (tip diameter), the evaporation of ink and the wettability of nozzle and substrate can be found in the book chapter (Fang and Aabith et al., 2017).

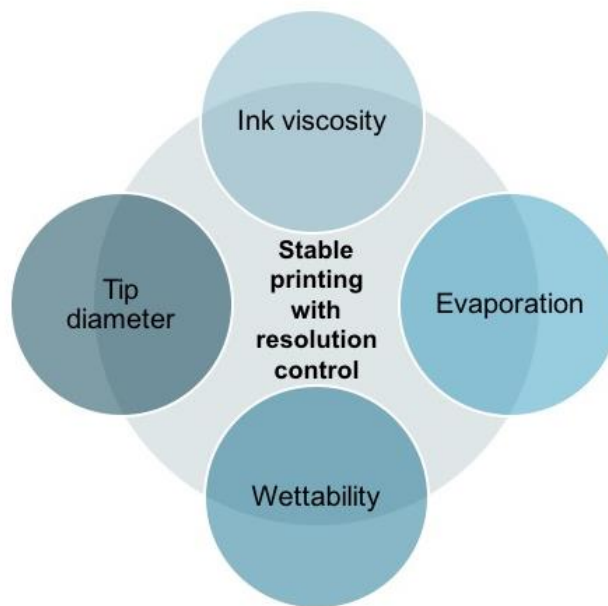


Figure 3.4: Summary of the main parameters (ink viscosity, evaporation of ink mainly based on the solvent used, wettability of the nozzle & substrate and diameter of tip) for stable printing with resolution control for direct-write printing

Chapter 4 - Experimental methods

This chapter describes and expands on the two main experimental setups used in this thesis. The mainstay of fabricating microstructured (pyramidal) dielectric medium has been photolithography (Clementine M Boutry et al., 2015; Ruth et al., 2019; Tee et al., 2014; Zhang et al., 2017). Herein we describe our approach of utilising high-resolution direct-write 3D printing for fabricating pyramidally microstructured dielectric media for miniaturised enhanced capacitive pressure sensors, that are characterised with a LCR meter. Details of the rheological setup and procedures have been included in the appendix (A.1 Rheometer setup and procedures).

4.1 Direct-write assembly for high-resolution printing

4.1.1 Nozzle fabrication

The P-1000 micropipette puller from Sutter Instruments (Figure 4.1a) was used to fabricate fine glass nozzles with particular nozzle apertures (that were programmed) to form the 'pen' through which the synthesised inks would be extruded in the direct-write assembly.

Borosilicate glass capillaries were bought from world precision instruments (WPI) (B150-86-7.5, WPI). The capillaries were used to make the printing nozzles and are available in varying diameters, wall thicknesses and lengths. For the purpose of printing, capillaries 'B150-86-7.5' (outer diameter: 1.5 mm, inner diameter: 0.86 mm & length: 7.5 cm, see Figure 4.1b) are inserted and secured (using knobs) along the pipette puller bars, so that the centre of the capillary is inside the heating element (filament) in the centre of the machine.

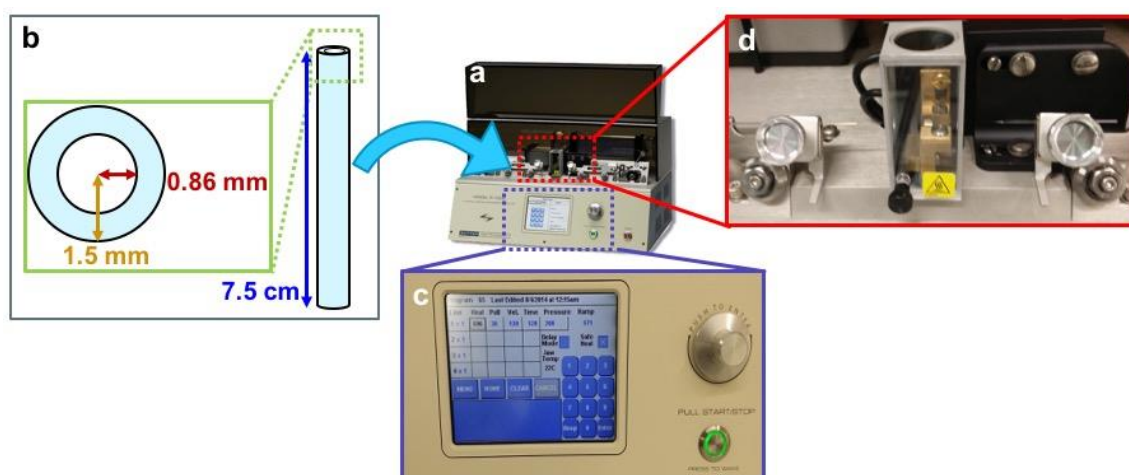


Figure 4.1: a.) P-1000 micropipette puller from Sutter Instrument (Oesterle, 2017) b.) Schematic of the borosilicate glass capillary with inner and outer diameter dimensions c.) The front panel provides the user interface for navigating and programming the machine d.) The resulting nozzles after the machine has finished running the program. The program details can be found in the appendix (A.2 P-1000 Sutter Instrument parameter programs)

The user interface was used to program the machine to run such that the desired nozzle size was fabricated. The 5 main parameters in the program to be set by the user were: Heat, Pull, Velocity, Time/Delay & Pressure. The 'heat' parameter determined how much current was applied across the filament, which resulted in heating up the filament. The filament must be sufficiently heated to melt the glass capillary, which depended on the glass wall thickness and the filament used for heating. The 'velocity' parameter was related to the rate of separation of the puller bars holding the glass capillary, once the glass started to melt inside the filament. This rate was detected by a transducer inside the puller and if the 'user set velocity' value was detected, then the current to the filament was stopped, which resulted in the heating stopping and the cooling to start. For more details on all the parameters, refer to the Sutter instrument manual (Oesterle, 2017).

The default parameter settings provided in the supplier manual (Oesterle, 2017) cater for nozzle sizes ranging from 600 nm to 3 μm only. In order to print with bigger nozzle sizes ($>3 \mu\text{m}$), the parameters were varied systematically 'one parameter at a time' and the effect on the resulting nozzle size was checked. It became clear that the most significant parameters for varying nozzle aperture were 'heat' and 'velocity'. Varying the parameters accordingly, the required larger nozzle sizes (5 to $35 \pm 2 \mu\text{m}$) were successfully made as shown in Figure 4.2a.

In order to reproduce the nozzle apertures for a given set of inputs, the system had to be left to cool for a given time, so that the machine conditions are the same for each pull. This was determined by using the same program repeatedly with different 'cooling times' between each consecutive pull. The minimum time

to maintain reproducibility of the nozzle size with a tolerance of $\pm 0.2 \mu\text{m}$ was found to be at 5 minutes as shown below in Figure 4.2b.

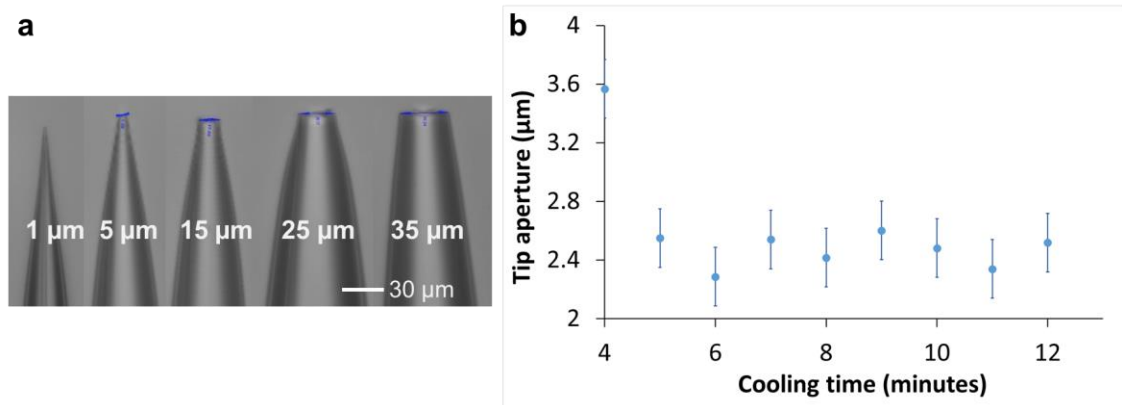


Figure 4.2: a.) Microscope images of nozzle apertures from 1 to 35 μm b.) relationship between nozzle aperture (μm) and cooling time (minutes) between each consecutive pull for the same parameter program

4.1.2 Direct-write printing

The 3D printer setup essentially consists of four main parts: the nozzle assembly, the stage controllers (controlled by the user through a PC) that control the three stepper motors (for the three directions x, y & z), an objective microscope focusing on the aperture of the nozzle and a nitrogen gas supply to be able to apply pressure to the syringe barrel (Figure 4.3). The nozzle assembly consists of a syringe barrel that is filled with the required ink to be printed. The actual 'pen' for printing consists of a dispenser with an attached glass nozzle. The attached glass nozzle can have apertures ranging from 600 nm to a maximum of 35 μm , depending on the resolution and application needed.

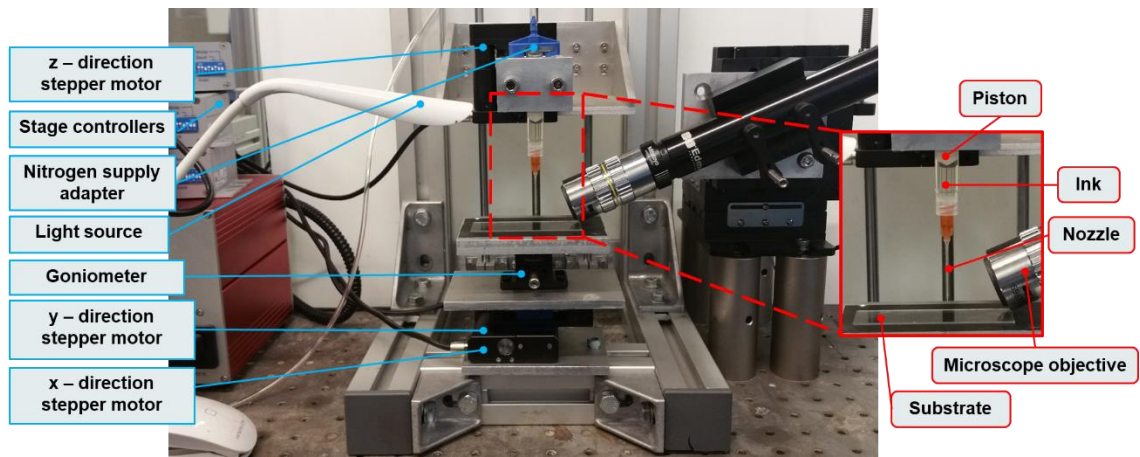


Figure 4.3: Direct-write assembly - 3D printer setup

The actual printing process was made up of initially mounting the substrate – which would get printed on top of – onto the x & y stage. Then the syringe barrel was loaded with the formulated ink to be printed and a piston was inserted into the syringe barrel and pushed till the ink meniscus was visible on the syringe barrel nozzle opening (Figure 4.4a). A glass nozzle (nozzle) with the desired aperture size was attached to the syringe barrel (Figure 4.4b). Then an adapter from the nitrogen supply was connected to the top of the syringe barrel. This nozzle assembly was fitted to the z direction stepper motor as shown in Figure 4.4c.

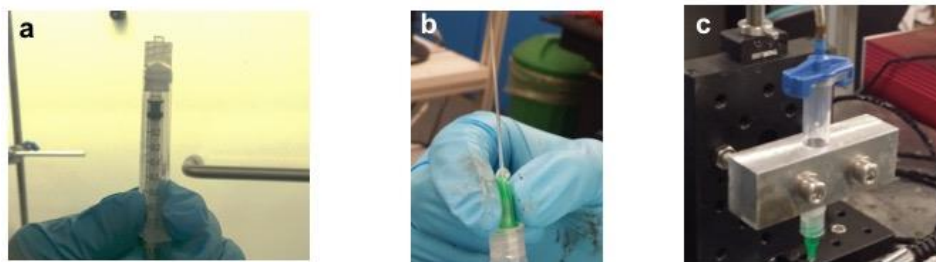


Figure 4.4: a.) Loading ink, inserting piston and forming a meniscus at the opening b.) Mounting nozzle to the syringe barrel c.) Mounting nozzle assembly to the printer

The nozzle is brought close to the surface of the substrate through focusing the objective microscope at the tip of the nozzle (Figure 4.5a). In order to align the

nozzle and the surface of the substrate, 2 parallel lines are drawn with the spacing between them being the same size as the nozzle aperture (Figure 4.5b). But, if the nozzle is in the bigger size range (20 to 30 μm) then the gap between the nozzle and the substrate is maintained to be half of the nozzle aperture. So if the nozzle opening is 22 μm , then the gap between the lines is set to be 11 μm . Then the software controlling the three motors is used to move the stage, so that the goniometer can be adjusted to ensure that the gap between the two lines is constant throughout the motion. Once this gap is consistent for the complete stage, then the stage is levelled (parallel to nozzle opening). Next, an electronic valve is used to pneumatically ‘push’ the ink out of the nozzle using the LabVIEW interface (Figure 4.5c).

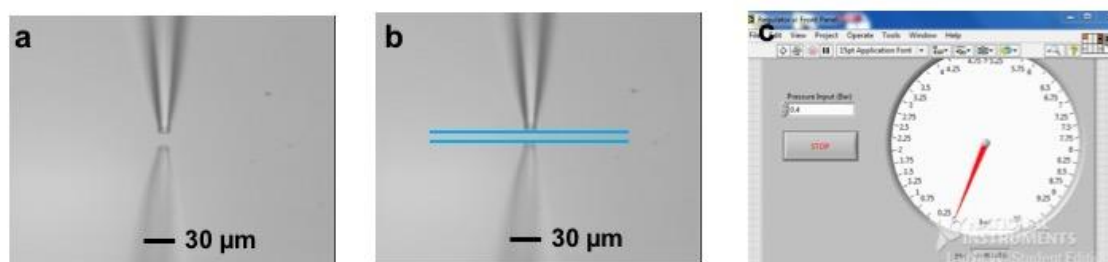


Figure 4.5: a.) Nozzle close to the substrate b.) Parallel lines to make the nozzle-substrate gap constant (levelling) c.) Labview interface for the electronic pneumatic regulator

Then as soon as the ink comes out of the nozzle and forms a capillary bridge (Figure 4.6a) the printing program is initiated and the 3 stages move according to the programmed pattern to be 3D printed. In essence, the setup can be seen as a stationary pen (the glass nozzle with ink droplet) with stages that are moving with the substrate to get ‘printed’ on. In this way the programmed pattern is 3D printed in an additive manner, layer by layer (Figure 4.6b). It should be noted that some surfaces like copper substrates needed to be corona treated with a laboratory corona treater (BD-20AC Laboratory Corona Treater,

Electro-Technic Products) in order to enhance/increase the surface energy of the substrates and facilitate good printout adhesion,

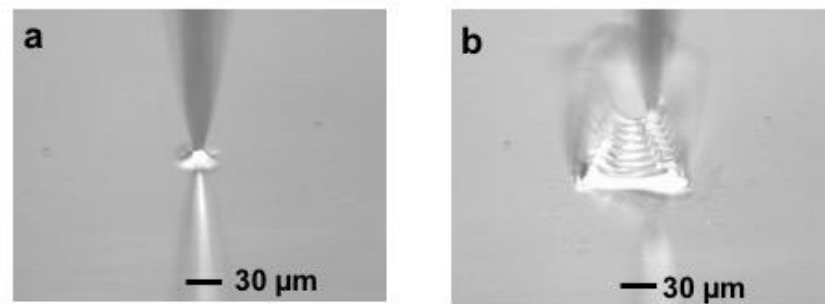


Figure 4.6: a.) Capillary bridge formed between the nozzle and the glass substrate b.) Printing a 3D structure

4.2 Capacitive pressure sensing

4.2.1 PCB design & Cjig

To reliably characterise the printed dielectric structures, the electrodes had to have minimal defects and the sheet resistance for each electrode used should be as consistent as possible. Printed circuit boards (PCBs) offer this capability and more. PCBs have developed into an integral part of the electronic industry (“World PCB Production in 2014 Estimated at \$60.2B,” 2015) for the many benefits they offer over wired circuitry, such as compact design, ease of maintenance, minimal electronic noise (low cross-talk between components) (Lee, 2019), etc. Semi-flexible (18-600-18, FR4, Holders Technology Plc) and flexible (12-20-12, ESPANEX, Holders Technology Plc) PCB sheets were obtained. The contact electrode pads were designed in DipTrace (NoVarm Limited) as shown in appendix (A.3 PCB design software DipTrace) with dimensions presented in Figure 4.7b. The user programmed structures were printed onto the contact pads (Figure 4.7c). Figure 4.7d shows an example of a printed raster pattern. Flexible wires were soldered onto the larger end of the contact pads.

A capacitive pressure measurement jig ‘Cjig’ was designed such that the parallel plates (electrodes) were aligned vertically and horizontally. Figure 4.7a shows the first version of the Cjig without the extra alignment pins, which were added later for smaller (<3 mm) square contact pads.

Initially, FR4 (semi-flexible – 0.6 mm thickness) PCBs were used for the characterisation of the printed dielectric structures. Figure 4.7e shows the flexible Espanex based (12 μm copper thickness) PCBs inside the Cjig.

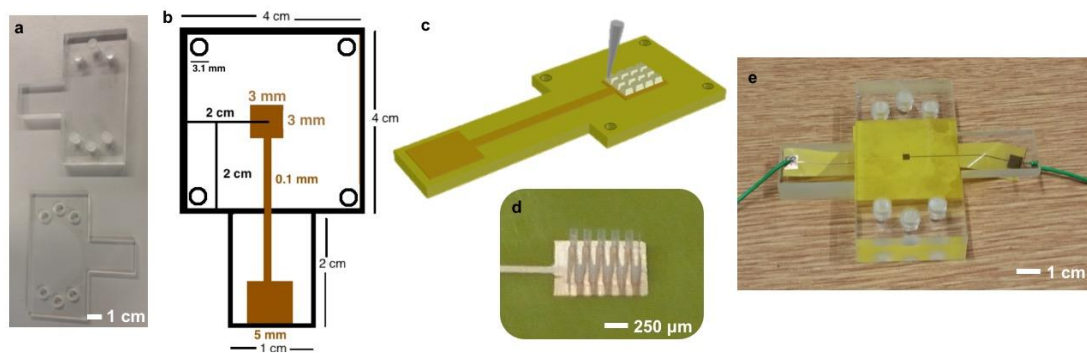


Figure 4.7: a.) Cjig made of acrylic b.) PCB design of 3 mm square contact pads c.) Schematic showing the printed dielectric on the designed PCB board d.) 3D printed raster pattern on contact pad e.) Flexible Espanex PCB inside Cjig

4.2.2 Measurement setup

A LCR meter with Kelvin probes (Figure 4.8a) was used to obtain capacitance readings from the sensor. The setup was calibrated following the steps from the manual, which can be found in appendix (A.4 Calibration steps of LCR-821) by placing the Kelvin probes at the same distance apart as they would be placed during the actual capacitance measurement. This calibration step measures the capacitance between the probes and stores that value as the default capacitance. In essence it was ‘taring’ the meter so that the capacitance reading was only that of the capacitance across the device under test (DUT). The main LCR meter settings for the measurement consisted of a frequency of

100kHz, a voltage of 1V and a parallel equivalent circuit configuration as recommended by the manual.

Once the LCR meter was calibrated the Kelvin probes were connected to the terminals of the sensor as shown below in Figure 4.8b. Small acrylic plates weighing 1 g, 0.5 g and 0.25 g were used as loads to apply pressure to the sensor. For each load that was applied, the measurement was taken from the LCR meter (Figure 4.8c).

This was completed for a range of 0 – 6kPa for most of the sensors that were made with dielectric height of 100 μm , since the 100 μm high structures deformed beyond ~ 6 kPa. But for the sensors with larger dielectric heights (650 μm , etc.) the range was extended accordingly (up to ~ 22 kPa).

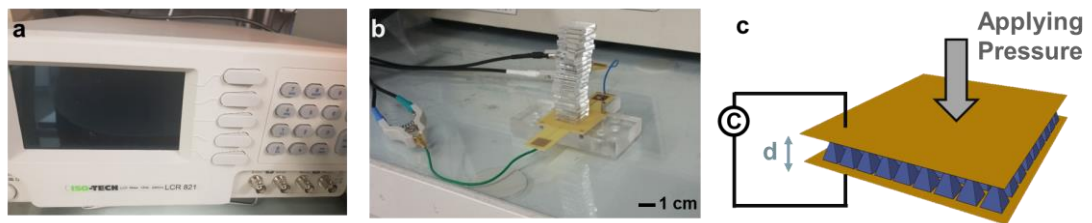


Figure 4.8: a.) Photograph of the LCR meter (model LCR-821, Iso-tech) b.) Sensor connected through the Kelvin probes to LCR with acrylic plates (loads) placed above it c.) Schematic of capacitive pressure sensor with pyramidal structured elastomeric dielectric

Chapter 5 – Decoupling printability from ink synthesis for rapid prototyping

This chapter presents rheologically underpinned formulations of a range of concentrations of a 3D printable polymer ink. The ink is compared to other inks that have been reported to be 3D direct-write printable. The ink is employed for a micromoulding approach that enables low viscoelastic materials such as PDMS (Silicones) to be effectively moulded at the micrometre scale.

5.1 Experimental procedure

5.1.1 Polyvinylpyrrolidone (PVP) ink

Polyvinylpyrrolidone (PVP), also known as polyvidone or povidone, is a water soluble polymer that comes in the form of a white hygroscopic powder that is readily dissolved in various polar solvents (Kumbar et al., 2014). It has been around for almost 80 years and is one of the most commonly used biomaterials (Lee, 2005). PVP has been utilised primarily due to its great adhesion properties (Lee, 2005) in multiple sectors, including the pharmaceutical industry, where it is used as a coating agent or tablet-binder.

In this project 3D printable PVP inks were developed by varying the PVP concentration and solvent. For this PVP (powder form) with molecular weight of 360,000 Da was purchased from Sigma Aldrich. PVP was added into glass vials and dissolved initially in various solvents including Isopropanol, Ethanol, Acetone, N-Dimethylformamide and DI water to test for printability. However, in order to keep the developed ink away from harmful solvents, the ink with DI water was used and further characterised. Water solutions of PVP were

prepared by dissolving PVP (molecular weight of 360k Da) in varying concentrations from 10 to 40 wt% in DI water via stirring at 60 rpm at room temperature (RT) over 6 days. The varying PVP concentration inks were developed in order to test, rheologically compare and establish a suitable range of 3D printable PVP inks.

Here we define 3D printability as the ability to form self-standing printed structures. The developed inks that were used here are known to be safe, biocompatible and were prepared outside the cleanroom.

5.1.2 Polydimethylsiloxane (PDMS) and EcoFlex inks

Two different silicones and nanocomposites of them were used to fill the printed moulds. Firstly, Polydimethylsiloxane (PDMS, Sylgard 184 Silicone Elastomer Kit) was purchased from Fisher Scientific. The kit consists of two components, the pre-polymer (base) and the cross-linking agent (curing agent). Both were added into a vial in the recommended ratio of 10 parts of silicone base to 1 part of curing agent (10:1). This was stirred with a spatula for 3 minutes (Lam and Ngo, 2007; Schneider et al., 2008) and then desiccated in a vacuum chamber for another 20-30 minutes in order to remove the trapped air bubbles inside the silicone mixture (Johnston et al., 2014). The vacuum chamber would expand the trapped air bubbles and consequently cause them to rise to the surface and burst (Lam and Ngo, 2007). The PDMS compound could be cured at various temperatures - ranging from room temperature to 200 °C – each curing temperature would result in different Young's moduli for the cured PDMS (Johnston et al., 2014). For this project, the PDMS was cured at 125 °C for 20 min as recommended by the supplier (Dow corning, 2014). Additionally, Ecoflex (Ecoflex series 00-50) was purchased from Bentley Advanced Materials.

Ecoflex (00-50) was prepared in the recommended ratio of 1 part A to 1 part B (1:1). This was stirred for 2 minutes and desiccated in the vacuum chamber for 10 minutes. EcoFlex had to be cured at 125 °C for 3 hours.

5.1.3 Dispersing carbon black in PDMS

Carbon nanoparticles have been previously reported (Achour et al., 2008; Dang et al., 2012; Matchawet et al., 2016; Nan et al., 2010) as nanofillers for enhancing the relative permittivity of polymers like PDMS. Carbon black nanoparticles (~40 nm particle size) were purchased from Sigma Aldrich. Spatula stirring in carbon black nanoparticles directly into PDMS(10:1) proved to be an ineffective way of ensuring a good carbon black dispersion in the PDMS matrix. It is well known that nanoparticles tend to agglomerate when stored in a container (Tuncer et al., 2009).

In order to improve the dispersion, the carbon black nanoparticles were added into the curing agent without the base polymer, such that the carbon black concentration was 0.1% of the PDMS (base and curing agent). Since probe sonication helps in reducing agglomeration of the CB nanoparticles (Siddiqui et al., 2009), the mixture was probe sonicated through a two-step process. The first sonication step was at an amplitude of 20% for a duration of 1 minute, followed by the second sonication step at an amplitude of 100% for 1 minute (Figure 5.1a). A longer sonication duration would have improved the dispersion, but it was limited to a total of 2 minutes due to the curing agent with the carbon nanoparticles starting to evaporate at around 1 minute into the sonication process. This was partially due to the heat produced in the sonication process (Figure 5.1b). The sonicated curing agent-CB mixture was added to the pre-

polymer base to form PDMS-CB composites. The curing profile was kept the same as in the case of PDMS without CB (125 °C for 20 min).

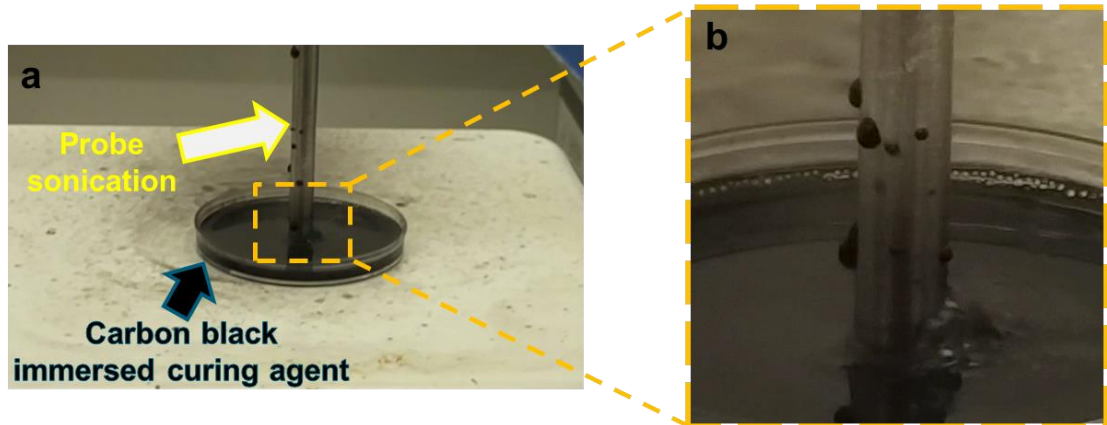


Figure 5.1: a.) Image showing carbon black nanoparticles 0.1 wt% immersed in curing agent and the probe sonication in process b.) Image showing a small amount of evaporated curing agent with carbon black nanoparticles on the probe

5.1.4 Rheological studies of PVP

The effects of the different PVP concentrations on the viscosity and viscoelasticity of the inks were rheologically studied using a rheometer (DHR-3, TA instruments). All tests were carried out at room temperature (controlled), with a sandblasted parallel plate geometry (40 mm) and a sample gap of 500 μm . The sandblasted parallel plate geometry was used to avoid any apparent wall slip (Mendes et al., 2014). The inks were subjected to a flow ramp (steady state response) and oscillatory amplitude sweep. The amplitude sweep was performed at a frequency of 1 Hz over a torque range of 0.1 to 10,000 $\mu\text{N}\cdot\text{m}$ at 5 points per decade following previously reported protocols (M'Barki et al., 2017; Valentine et al., 2017).

5.1.5 Mould printing

For the mould fabrication, hollow 3D structures (Figure 5.2a) were printed with our developed PVP inks at a speed of 0.2 mm/s and nozzle apertures ranging from 5 to 30 μm . The printed structures were then filled with PDMS, Ecoflex or PDMS with carbon black 0.1 wt%. This was done by loading a syringe barrel with the desiccated silicone, attaching a 1 to 3 μm nozzle to the syringe, lowering and aligning the nozzle assembly above the printed mould. The operator then applying sufficient pressure (0.1 to 0.3 bar) to the piston to just force the filler ink out of the nozzle and retracting the nozzle assembly once the mould was filled to the brim (Figure 5.2b). All of the steps were completely observable via the optical microscope. Bigger nozzles (greater than 3 μm) were not used since they resulted in some PDMS droplets leaking from the nozzle without control. The filled mould was left to cure in an oven at 125 °C for 20 minutes, such that the PDMS cured completely (Figure 5.2c). The mould with the cured moulding was placed outside the oven at RT for another 10 minutes to cool down completely. The water soluble PVP mould was then simply washed away with few water droplets by simply pipetting water onto the mould. This resulted in the moulding (PDMS structure) remaining behind (Figure 5.2d).

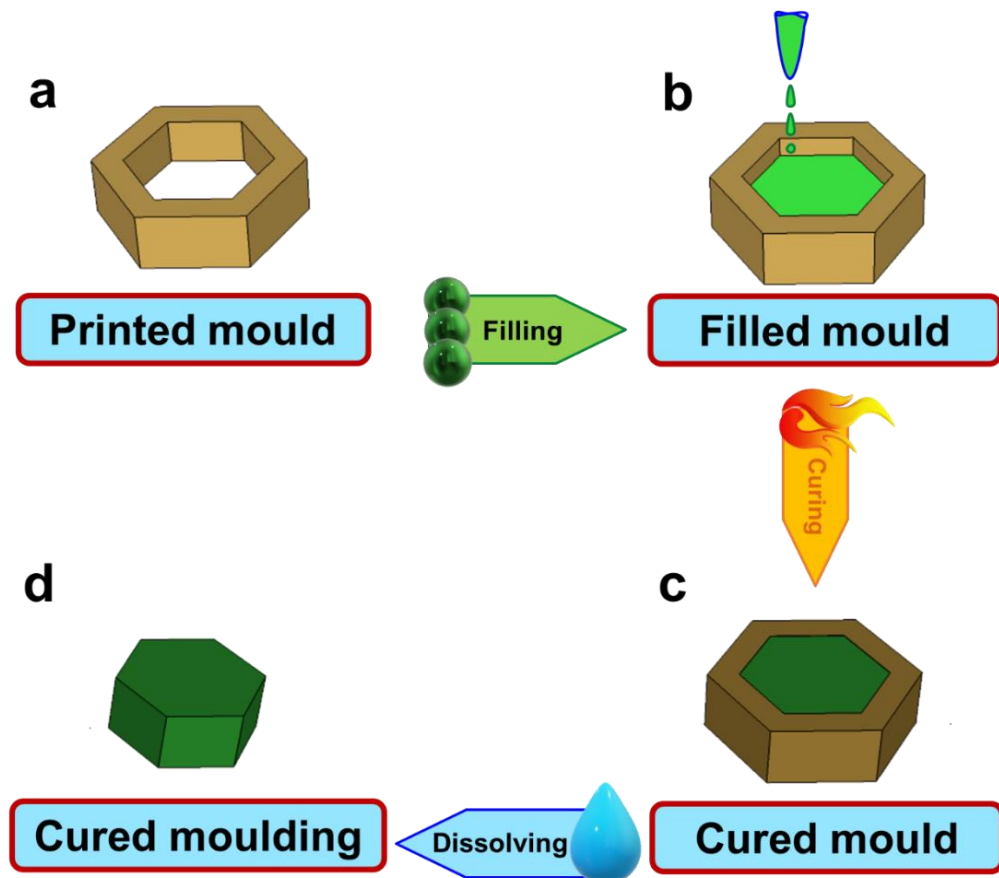


Figure 5.2: Schematic overview of the mould process: a.) Printing PVP mould b.) Filling printed mould with PDMS via nozzle c.) Curing mould with PDMS content at RT for 48 hours or in oven at 125 °C for 20 minutes d.) Pipetting a few water droplets onto the mould in order to dissolve the PVP mould and leave behind the cured and structured PDMS moulding

This was done for different structures including 3D hexagons (Figure 5.3a-d).

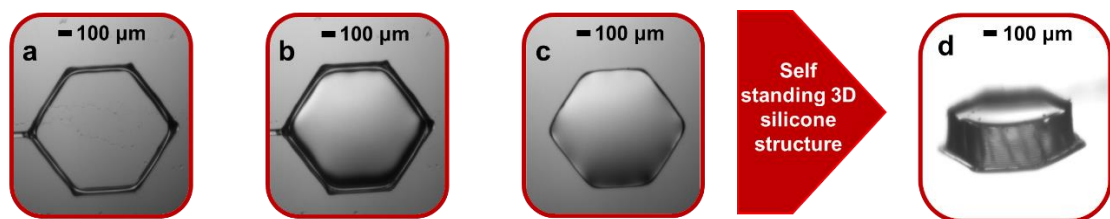


Figure 5.3: a.) Printed hexagonal structure b.) PDMS filled and cured mould c.) top view of the cured moulding without a mould d.) 3D view of the cured moulding

5.2 Results & Discussions

5.2.1 Rheology of PVP

The flow behaviour and viscoelastic properties for 10, 15, 20, 25 and 30 wt% PVP ink concentrations were characterised. From the steady state response of the 10 to 30 wt% PVP inks (Figure 5.4a) it was observed that the zero shear viscosity values increased from 0.3 Pa.s to 40 Pa.s with an increase in PVP concentration. The inks show clear shear thinning across the PVP concentrations in the shear rate ($\dot{\gamma}$) region of 46 – 1600 s⁻¹. This corresponds to our printing speed of 0.2 mm/s for nozzle sizes 1 – 35 μ m and can be calculated from

$$\dot{\gamma}_{max} = \frac{4 \times \dot{Q}}{\pi \times r^3}$$

where r is the nozzle radius (m) and \dot{Q} is the volume flow rate (m³/s). The volume flow rate is calculated as

$$\dot{Q} = S \times \pi \times r^2$$

with S being the printing speed (m/s) (Janna, 2010). The higher concentration inks (20 to 30 wt%) show small shear thickening at lower shear rates, which can be attributed to intermolecular entanglements that can form during low shear rates (Vrahopoulou and McHugh, 1987). These entanglements will get destroyed during higher shear rates, leading to a reduced viscosity (shear thinning).

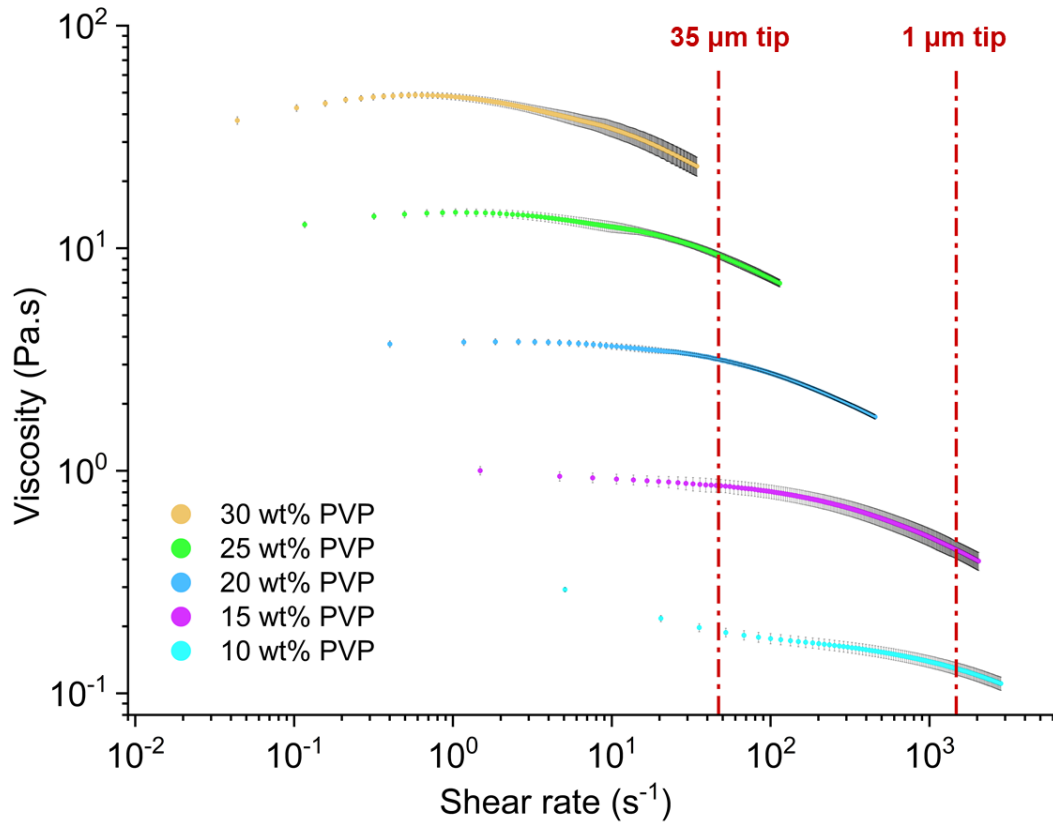


Figure 5.4: Steady state response of PVP inks: Viscosity as a function of shear rate

The flow index numbers (n) for the different PVP concentrations (Figure 5.5b) were obtained from fitting a power law model $\tau = \alpha \dot{\gamma}^n$ to the shear stress (τ) as a function of shear rate ($\dot{\gamma}$), where α is the slope (Figure 5.5a). The flow index numbers for the different PVP concentrations are very similar ranging from 0.64 to 0.75, suggesting similar flow behaviour.

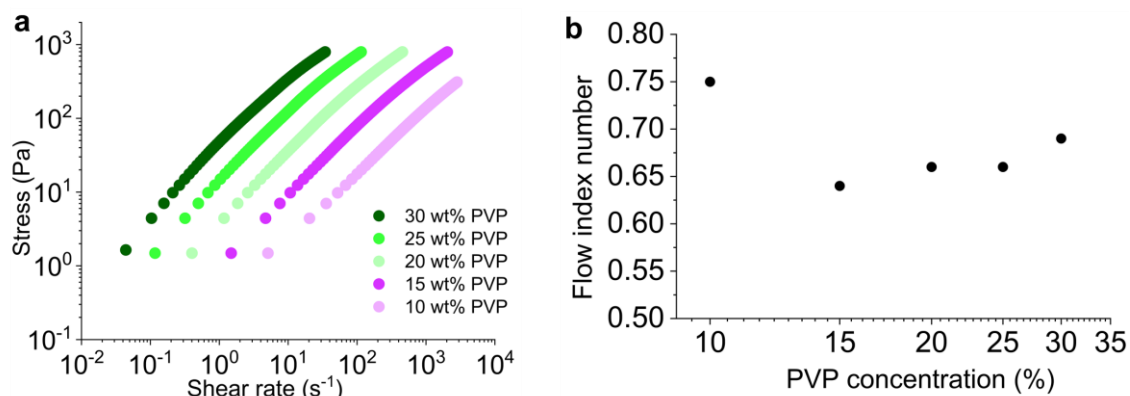


Figure 5.5: a.) Oscillation stress as a function of shear rate b.) Flow index number for different PVP ink concentrations

The viscoelastic response (Figure 5.6) shows that the storage modulus is lower than the loss modulus for all PVP concentrations ($G' < G''$), as was the case for the UV assisted 3D printable polyimide ink reported by Yuxiong et al. (Yuxiong Guo et al., 2019b). This is in contrast to the 3D printable graphene oxide (GO) based inks from Esther et al. (García-Tuñón et al., 2017) and the 3D printable silver flake loaded thermoplastic polyurethane (AgTPU) from Alexander et al. (Valentine et al., 2017), both of which have a higher storage modulus than loss modulus ($G' > G''$). This has influence on the ink's consistency and print resolution (Figure 5.7), where the GO based ink and AgTPU ink are more paste like and are printed with 510 μm and 200 μm nozzles respectively. This is bigger than the 90 μm nozzles used for the polyimide ink, which was more liquid like and also needed UV assistance while printing to help the curing/printing process. This suggests that dominant viscous properties (G'') with some viscoelastic properties (G') are more suited for higher resolution printing focussed herein.

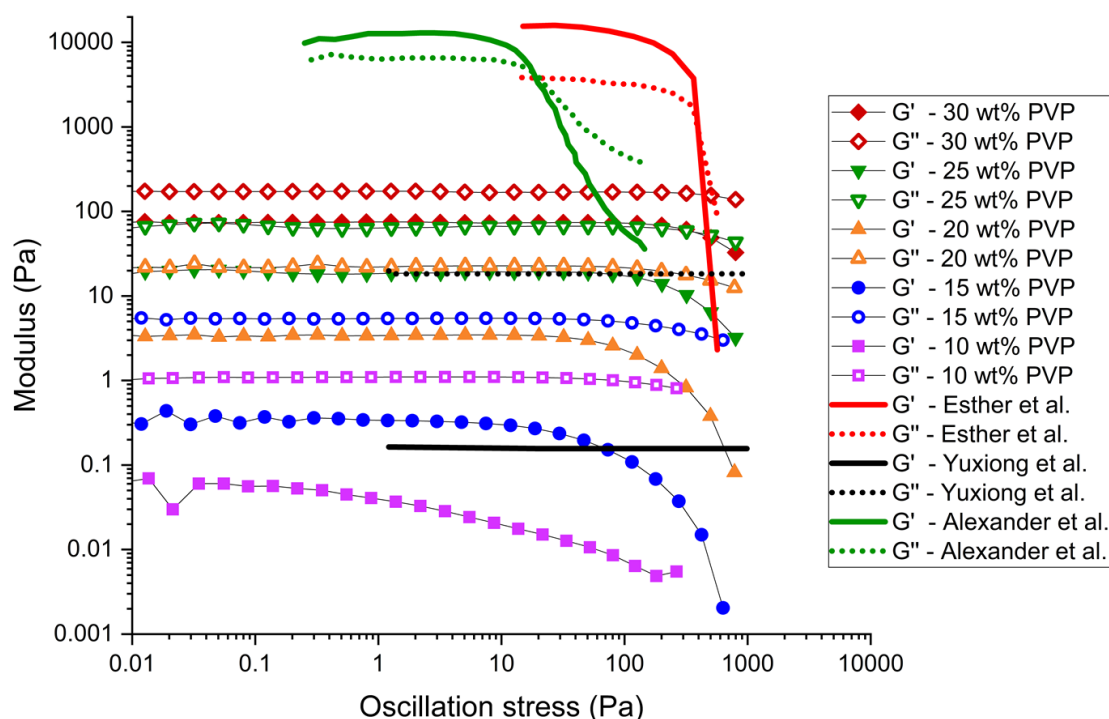


Figure 5.6: Viscoelastic properties of PVP inks: a.) G' and G'' as a function of oscillation stress for the different PVP concentrations and other reported inks (García-Tuñón et al., 2017; Yuxiong Guo et al., 2019a; Valentine et al., 2017)

The G''/G' plot in Figure 5.7 shows the expected outcome for the liquid like inks approaching the gelation point ($G' = G''$) (Mewis, J. & Wagner, 2012) when increasing the polymer content of the ink. This is due to the increased formation of polymer networks when the polymer content is increased.

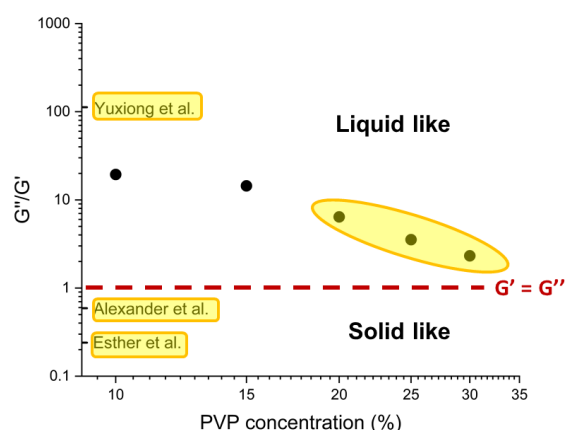


Figure 5.7: Ratio of loss modulus to storage modulus as a function of PVP concentration in comparison to other inks (García-Tuñón et al., 2017; Yuxiong Guo et al., 2019a; Valentine et al., 2017), with the 3D printable inks highlighted in yellow

5.2.2 Printability of PVP

In order to develop a 3D printable water based PVP ink, the PVP concentration was varied from 10 to 40 wt% and tested with different tip (nozzle) apertures ranging from 1 μm to 35 μm . The 40 wt% PVP ink was unprintable and always led to nozzle clogging. Figure 5.8 summarises the printability of the different PVP concentration inks with respect to nozzle sizes.

With tip sizes 35 μm to 15 μm and a PVP concentration of 30 wt%, 'multilayer printing' – the ink was 3D printable and able to form self-standing structures without the nozzle clogging or fracturing at consecutive layers – was achieved (Figure 5.8d). Being able to 3D print multiple layers is crucial for making fully formed 3D structures. 'Multilayer printing' was also achievable with tip sizes of 25 μm to 15 μm and a PVP concentration of 25 wt%. Similarly, multilayer printing was attained with tip sizes of 15 μm to 5 μm and the 20 wt% PVP ink. Tips under 5 μm only achieved 'single layer printing' – being able to print a single complete layer only after which (in the consecutive layer) the nozzle either clogs up or breaks (Figure 5.8c) - for all concentrations, due to the tip breaking in the second layer.

The 10 wt% PVP ink with tip sizes of 35 μm to 15 μm was not printable. In this case the ink simply wet the surface without forming a filament (Figure 5.8a). Tip sizes less than 14 μm but bigger than 3 μm were 'printable' with the 10 wt% PVP ink, meaning, being able to form filaments that are adhering to the surface, but not being able to complete the first layer due to either nozzle fracturing, clogging up or the ink overflowing (Figure 5.8b).

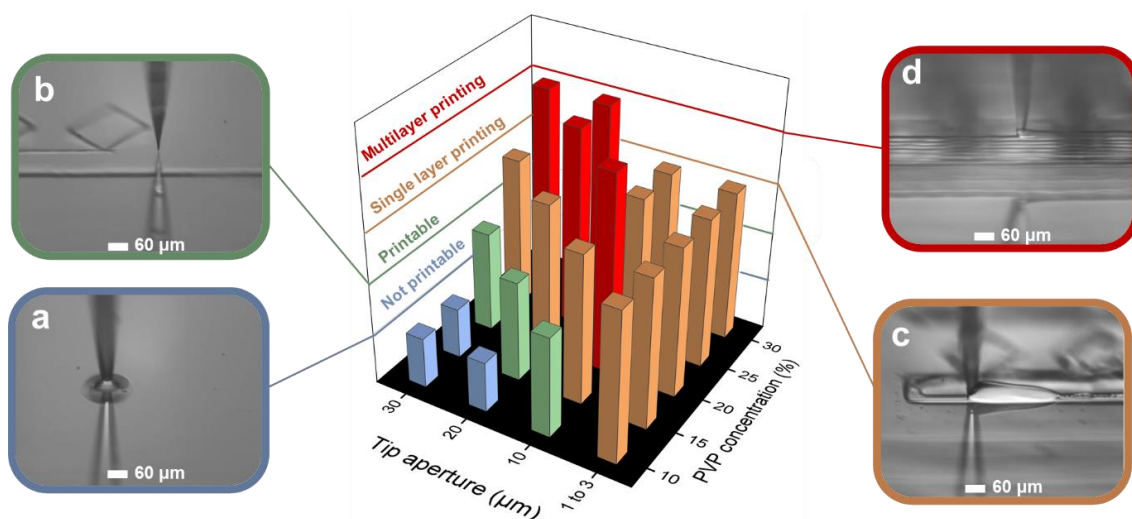


Figure 5.8: Guide to achieving printability of different PVP ink concentrations with different nozzle sizes: a.) 'Not printable' meaning that the ink would just wet the surface without forming a surface adhering filament b.) 'Printable' meaning that the ink was able to form strands that were adhering to the surface, but it was unable to complete the initial layer due to either nozzle fracture, clogging or overflowing c.) 'Single layer printing' meaning that the ink was able to complete a single layer, but being then not able to complete the consecutive layer due to nozzle clogging or fracture d.) 'Multilayer printing' meaning that the ink was 3D printable and able to form self-standing structures without the nozzle clogging or fracturing at consecutive layers

5.2.3 Mouldings

Owing to the good adhesion properties of PVP, the moulds were able to be printed onto various substrates including glass, copper, aluminium and stainless steel. The printable substrate range extends the potential applications of this moulding approach further.

Some of the moulds that were printed and their corresponding mouldings are shown in Figures 5.9 and 5.10. The star shape logo of UCLs' Wellcome/EPSCRC centre (WEISS logo) was printed on glass with a 10 μm tip and filled with PDMS(10:1) The printed mould was only 1 layer high ($\sim 10\ \mu\text{m}$), thus showing how suitable a water based mould is in its ability to be filled with a hydrophobic filling (PDMS or Ecoflex). The hydrophobicity of the PDMS stops it from crossing the printed mould boundaries (Figure 5.9a-c).

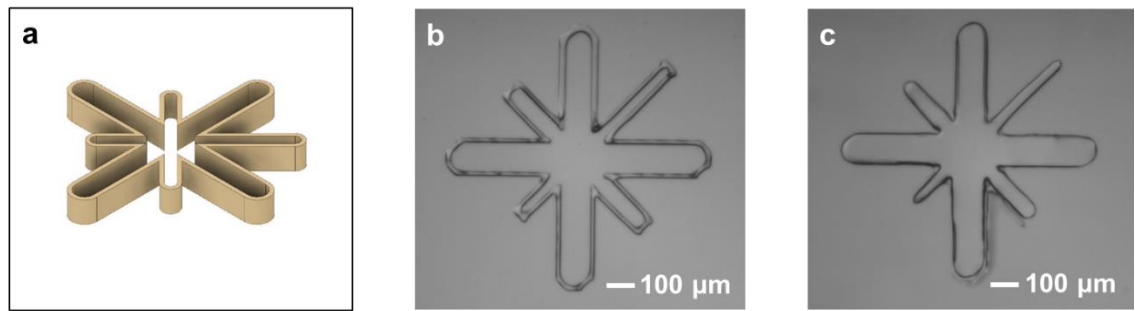


Figure 5.9: Star shaped logo of UCLs' Wellcome/EPSRC Centre for Interventional and Surgical Sciences (WEISS logo) a.) Schematic of the mould, b.) the printed mould and c.) PDMS(10:1) moulding

Similarly, more complex structures like pyramids were printed with a 15 µm tip (Figure 5.10a-b). The pyramids were filled with Ecoflex. Figure 5.10c shows an Ecoflex moulding of good quality, where the number of layers can be identified from the moulding itself. The tip of the pyramid is under 50 µm in diameter. It should be noted that at the end of each printout, an extra string of PVP would be formed while retracting the nozzle. This was simply washed away in the demoulding process (Figure 5.10c).

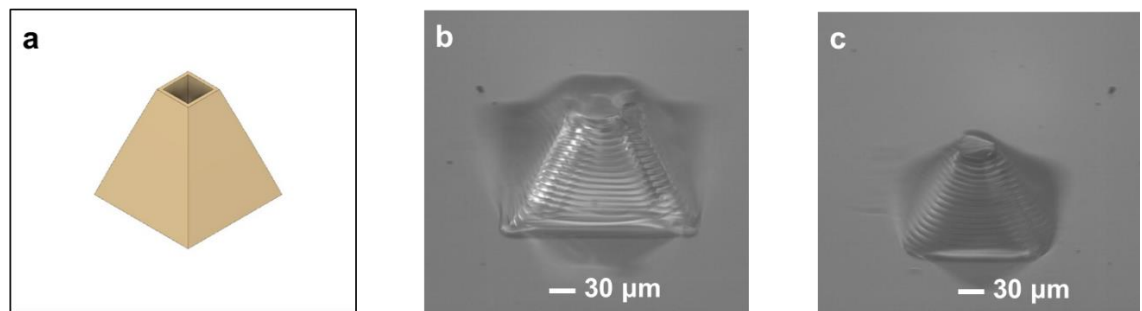


Figure 5.10: a.) Schematic of a pyramidal mould structure, b.) the printed mould and c.) Ecoflex moulding

5.3 Conclusions

- A set of water soluble PVP inks have been developed and characterised rheologically, for rapid high-resolution prototyping, enabling micrometre structures to be fabricated with ease outside the clean room.

- Exemplar printed micro moulds and their mouldings – made of silicone and silicone nanocomposites - were demonstrated ranging from simple 2.5D structures (WEISS logo) to more complex 3D structures (a Pyramid).
- This work and methodology introduce a safe and simple approach to prototype high-resolution ($<10\ \mu\text{m}$) structures using 3D direct-write printing, without the need for exhaustive formulation and optimisation of inks, which is a major challenge, where often the material with suitable properties for a desirable application lacks the required features to be AM fabricated.
- This approach opens the door for micrometre scale silicone structures to be AM fabricated into self-standing structures.
- This work permits several applications, especially in the world of flexible electronics and bioengineering, where the capability to precisely structure ‘soft’ materials on the micrometre scale is much sought after.
- The rheological data from this chapter serve as a guide for developing other potential printable inks at the micrometre scale.

Chapter 6 – Micro moulding approach for microstructured capacitive pressure sensors

This chapter demonstrates how the micro moulding approach developed in the previous chapter can be employed for microstructuring dielectric layers into pyramids without the need for photolithography. The chapter highlights how the challenges in filling pyramidal micromoulds were overcome and how bigger pyramidal structures provide a bigger sensing range and good response times. Additionally, the chapter describes the development of a prototype pressure sensing ring, which is a potential medical device that doctors and surgeons can wear. The chapter concludes with discrepancies in the resolution of the printed arrays of pyramid moulds.

6.1 Experimental procedure

6.1.1 Arrays as printed moulds

A microstructured dielectric layer consists of multiple structures. Thus printing of arrays of microstructures were pursued. In particular, printing with the developed PVP 30 wt% ink (chapter 5) arrays of micro moulds, filling them with elastomers, curing the filled moulds and then washing away the micro moulds with DI water proved to be an effective way to fabricate microstructured dielectric layers with ease away from the clean room, without any chemical etching or the need for any photolithographic techniques.

A 2.5D hexagonal micro mould array of 9 hexagons was programmed to follow the print path shown schematically in Figure 6.1a and direct-write printed (Figure 6.1b).

The hexagonal micro moulds were filled with PDMS using tips with diameters 1 – 5 μm as shown in Figure 6.1c. One of the moulds was not filled due to human error. Then the filled array was placed in the oven at 125 °C for 20 min to cure the PDMS inside the hexagonal micro mould. The mould with the cured moulding was removed from the oven and left to cool down outside for another 10 minutes. The mould was then washed away with DI water by gently placing a few DI water droplets on the mould repeatedly until the PVP was completely washed away, leaving behind the cured microstructured PDMS moulding as shown in Figure 6.1e, f.

It was noticed that there were some discrepancies in the quality of the printed moulds. In particular, the corners of the hexagons, that became more rounded with each layer that was printed, leading to oval structures instead of hexagonal structures. This was also reflected in the mouldings, which were oval structured instead of hexagonal. This occurred due to the extra ink that was accumulating at the glass tip – which is hydrophilic - over the printing duration, which led to more ink being drawn out of the tip, so that the effective diameter of the ‘pen’ was wider than the tip aperture.

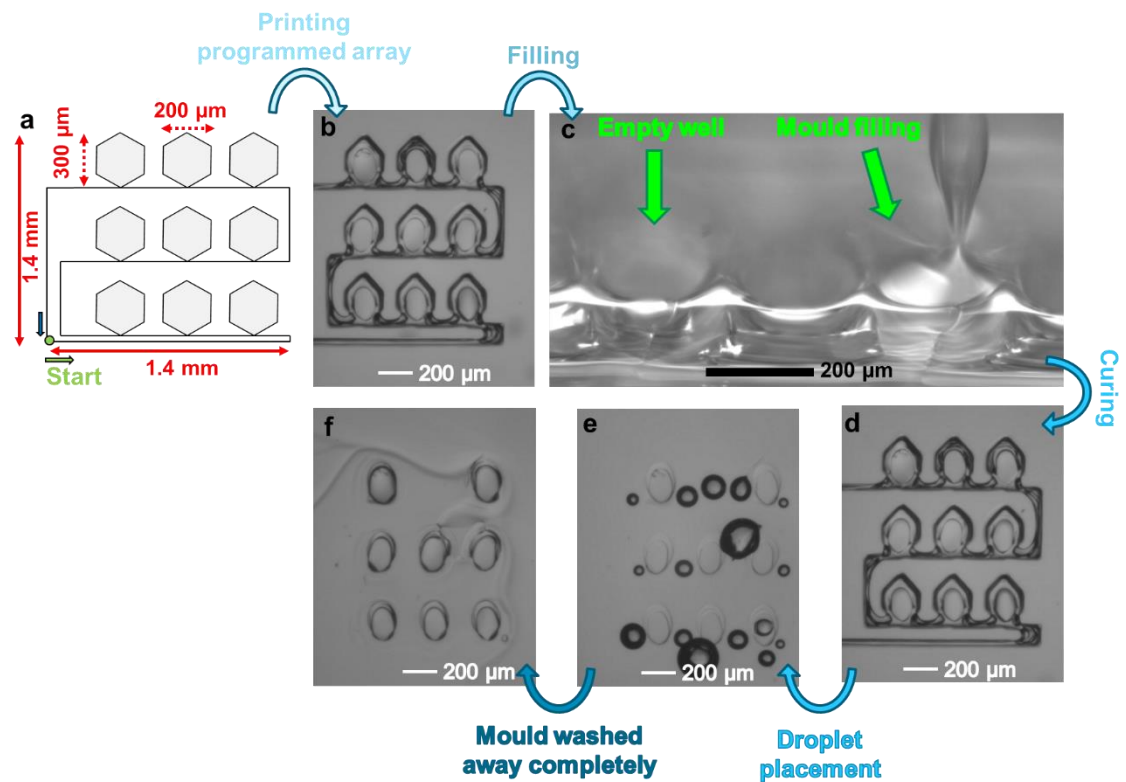


Figure 6.1: Micro moulding arrays a.) Schematic of path of printer in printing a 2.5D hexagonal micro mould array b.) Successfully printed hexagonal array on glass c-d.) Filling moulds with PDMS (10:1) followed by curing 125 °C for 20 min and letting cool down outside the oven at room temperature (RT) e.) After initial DI water droplet placement, there are still remnants of PVP f.) Repeated placement of DI water droplets completely washed away the PVP and left the moulded and cured PDMS structure

The array was updated so that the individual structures of the array form a square based pyramid similar to those that were reported from previous groups (Clementine M Boutry et al., 2015; Chen et al., 2014; Mannsfeld et al., 2010; Tee et al., 2014). The array was now made up of 25 square based pyramids, each pyramid with a square base of 141 x 141 µm (200 µm diagonal) and 200 µm high. Figure 6.2a shows the top view of the successfully printed array and Figure 6.2b shows the side view of the moulds. Filling of these pyramidal moulds was attempted by first aligning the tip above the pyramid mould and then lowering the tip into the mould Figure 6.2c. This was then followed by applying a back pressure of 0.1 to 0.3 bar – the amount of pressure needed to force the PDMS droplet out of the nozzle tip. The overhanging droplet that was

formed at the tip came into contact with the interior side walls of the pyramidal mould and thus started filling the mould. But, as the upper part of the pyramid mould was filled along the interior side walls, the air at the bottom of the mould became trapped. This prevented the ink from filling the bottom of the pyramid mould, as shown in Figure 6.2d-f.

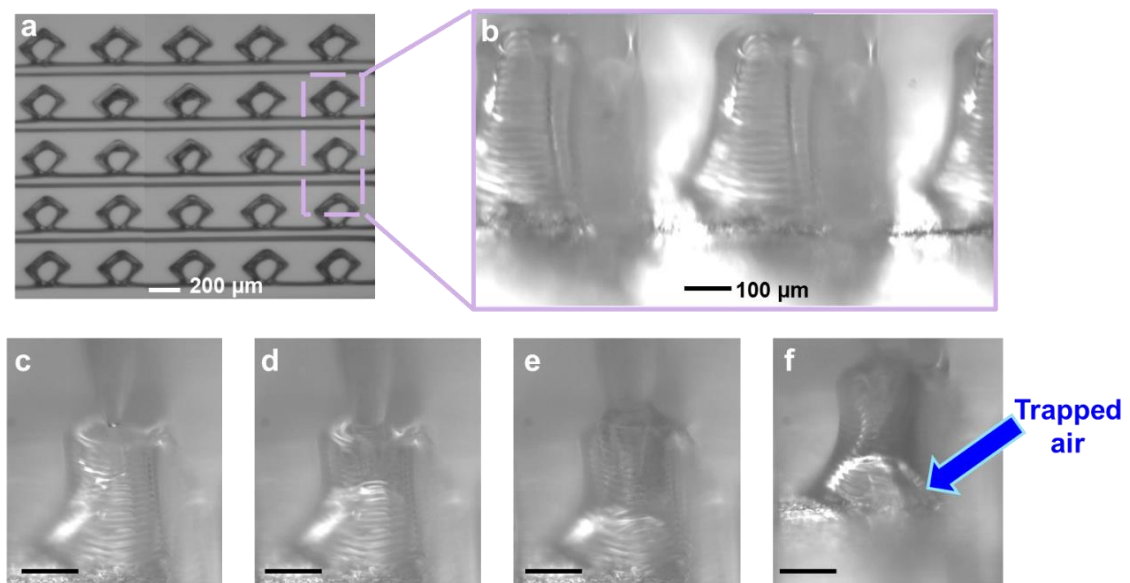


Figure 6.2: a.) Successfully printed square based pyramid micro mould array of 25 b.) Side view of the printed micro mould array c.) Pyramid filling attempt, with tip being centred above each mould and then lowered into the mould. d-f.) This is followed by applying a back pressure of 0.3 bar into the nozzle. The overhanging droplet of the tip makes contact with the interior walls of the pyramid and thus helps to start filling the pyramid. However, as the ink fills up the upper part of the pyramid along the interior side walls, the bottom part of the pyramid has air bubbles trapped inside it, preventing the ink from reaching the bottom of the pyramid. (Scale bar: 100 µm)

The trapped air problem was attempted to be overcome by using PDMS diluted with Hexane (10%) and varying the filling tip's sizes from 1 – 25 µm. But the problem was still persistent. In order to overcome this, rectangular based pyramids (base aspect ratio 1:n, where $n \geq 2$) were printed and moulded as a way to give the trapped air bubbles room to leave the mould as demonstrated in the next section.

6.1.2 Rectangular based pyramid micro mould printing

The square based pyramids were updated to rectangular based pyramid micro moulds, so that the air would have 'room' to leave the individual moulds during the filling process and not get trapped at the bottom of the moulds as encountered previously. Different dimensions for the rectangular based pyramid moulds were programmed and printed, including aspect ratios of 1:2 (100 μm x 200 μm), 1:4 (100 μm x 400 μm) and 1:10 (100 μm x 1000 μm). It should be noted that due to the ink accumulation on the tip and the consequent loss of resolution while printing, a new tip was used for each rectangular pyramid in the array. So for example, an array of 4 rectangular based pyramids would need 4 nozzles for printing, one nozzle per structure.

Once the moulds were printed, the filling process was initiated with the tip being lowered into the centre of a mould and then applying a back pressure of 0.1 to 0.3 bar (Figure 6.3a). As soon as the ink started to come out of the tip and fill the mould, the software was used to move the tip to the right, slowly at a low velocity of 0.01 mm/s until the right corner of the structure was almost filled. Then the software was used to move the tip to the left until the left corner was filled (Figure 6.3b-d). The tip was then raised to the surface of the filled mould. At the interface the back pressure was turned off and the tip was moved away from the filled mould (Figure 6.3e,f). In all mouldings, the air was able to easily exit the mould, mainly because the filling ink was able to reach the bottom of the mould instead of filling the top half of the mould and trap the air at the bottom of the mould. PDMS, PDMS in hexane (10%) and PDMS with carbon nanoparticles (0.1%) were all able to fill the moulds successfully.

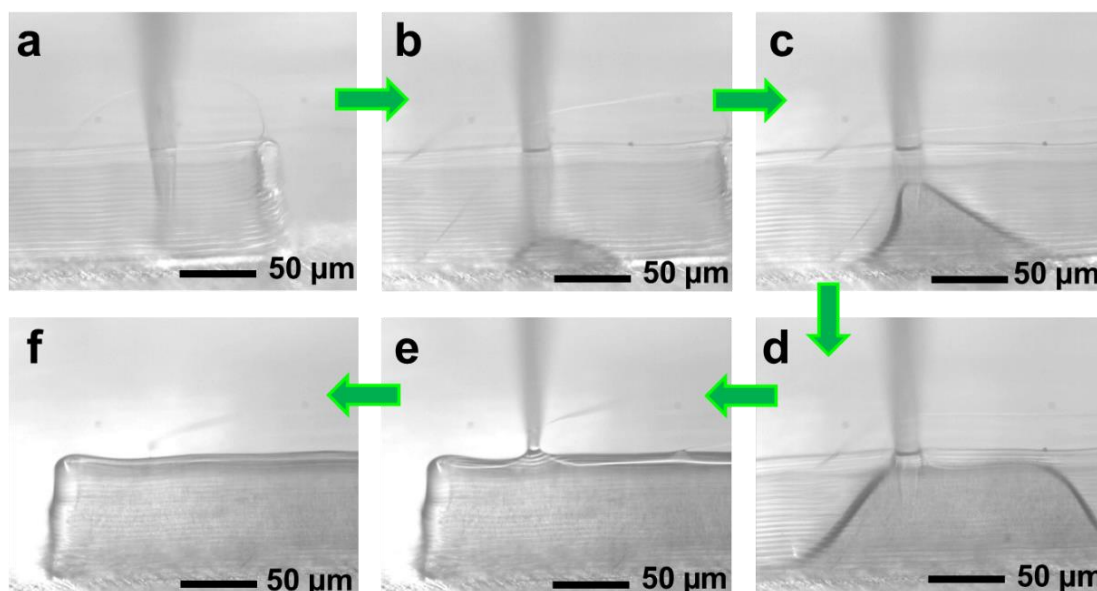


Figure 6.3: Rectangular ($100\ \mu\text{m} \times 400\ \mu\text{m} \times 75\ \mu\text{m}$) based pyramid mould filling process a.) Lowering the tip into the centre of the mould b.) Applying sufficient pressure ($0.1 - 0.3\ \text{bar}$) to force elastomer (PDMS_CB composite) out of the tip c-d.) Filling and moving to the right and then to the left hand side of the mould e.) Moving the tip to the surface of the filled mould f.) Turning off the pressure and raising the tip completely away from the filled mould

It should be noted that when the tip is raised to the surface of the filled mould, the back pressure is only turned off once, then the mould was filled to a maximum of $\sim 3\ \mu\text{m}$ above the mould and not under filled as shown in Figure 6.4a,b.

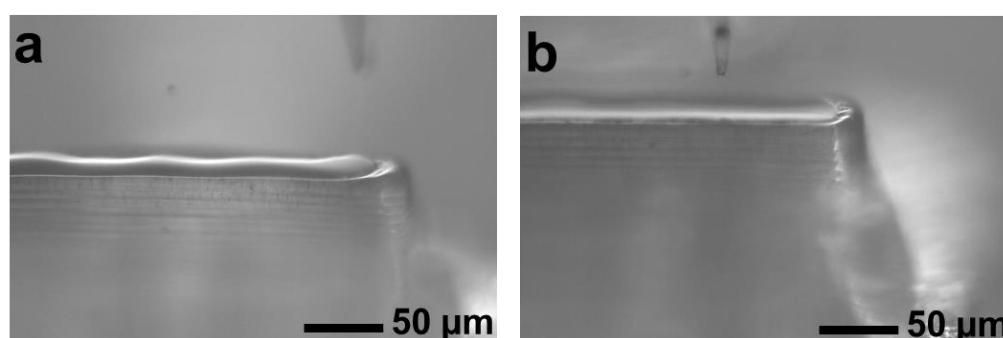


Figure 6.4: a.) Example of a sufficiently filled mould with a maximum overfill of $\sim 3\ \mu\text{m}$ b.) Example of an underfilled mould

However, a microstructured dielectric layer would need more than one rectangular based pyramid mould to be printed and filled. This meant that after the moulds were printed, a new tip (similarly sized $1\ \mu\text{m} - 5\ \mu\text{m}$) for the filling process had to be mounted to the syringe and aligned at the centre of the next mould with the help of the microscope. For example; to fabricate an array of 9 rectangular based pyramid moulds, 9 tips were needed for printing them and another 9 tips were needed for filling those moulds. The changing of tips between each mould printing and each filling was very time consuming. In order to reduce the overall fabrication time of the microstructured dielectric layer, the printing program was updated such that one tip would print each mould layer by layer and then move down to the starting point of the next mould – benefitting from the viscoelastic properties of the ink - and print it, without changing tips (Figure 6.5a). The line printing in between the moulds served as a ‘runway’ to allow some of the accumulated ink from the tip to become deposited – dragged off - from the moulds (Figure 6.5b,c).

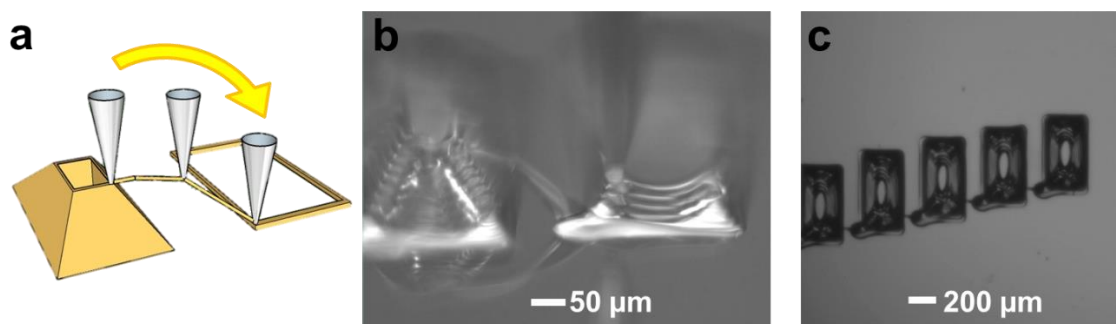


Figure 6.5: a.) Schematic demonstrating continuous printing array of moulds with one tip b.) Rectangular based pyramid moulds printed continuously with one tip on glass c.) Top view of a printed array of rectangular based pyramid moulds

It should be noted that for structures that were $> 100\ \mu\text{m}$ in height, the nozzle would dry out and break when moving from the top of the printed structure to the surface of the substrate (Figure 6.6a). This was overcome by introducing a

dabbing step in the nozzle movement, where the nozzle would print on the outside wall of the printed pyramid mould to avoid drying out (Figure 6.6b). This extra step did not affect the quality of the final moulding since it only affected the outside of the mould, which was washed away.

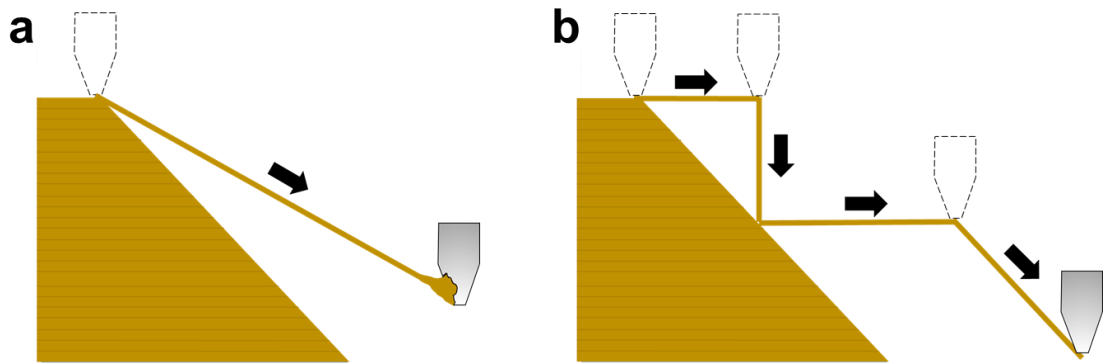


Figure 6.6: Schematic of the pyramid mould printing nozzle demonstrating a.) nozzle fracture when the nozzle moves directly from the top of the printed mould to the surface and b.) successful continuation of the printing array of pyramid moulds by moving the printing nozzle from the top of the printed mould to the outside of the mould and then reaching the surface without nozzle fracture

The filling of each mould individually was very time consuming (~2 minutes/mould), especially when the array size was near 100 pyramid moulds. Thus in order to overcome this, vacuum filling was introduced, as detailed in the next section.

6.1.3 Filling the entire micro mould simultaneously using vacuum

To reduce the overall fabrication time further, where the filling of the moulds took the biggest share of the overall fabrication time of the microstructured dielectric layer, a new technique was developed to fill the pyramidal moulds. This involved using the vacuum chamber to fill all of the moulds in an array simultaneously, instead of using the printer setup to fill each mould using one tip at a time.

The filler ink (PDMS, PDMS with CB, Ecoflex, etc.) was prepared as described in chapter 5. For the case of PDMS_CB(0.1%) filler, the ink was first degassed for 20 minutes and then pipetted above the printed micromould array on top of the copper electrode on the PCB board. The air was trapped inside the individual structures of the mould. The mould was placed inside the vacuum chamber and left to run for 20 minutes. This was so that the air moved out of the pyramids and the PDMS_CB went into the pyramids as shown in Figure 6.7.

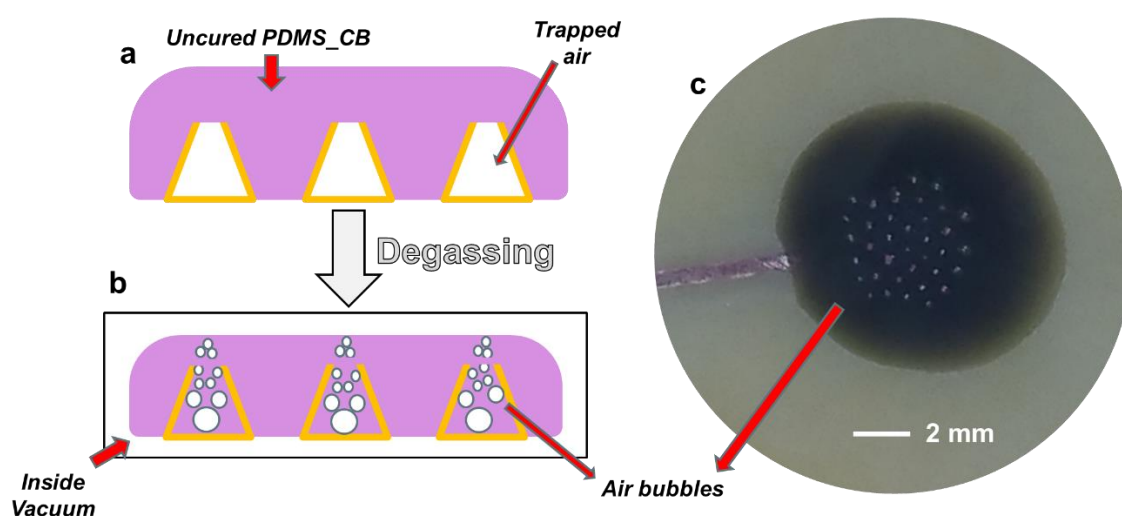


Figure 6.7: a.) Schematic showing the side view of the mould and the pipetted uncured PDMS above the mould b.) Schematic showing the side view of the degassing of the pyramidal moulds by placing moulds inside the vacuum chamber to force the trapped air bubbles out of the pyramidal moulds and force the uncured PDMS into the mould c.) Photo showing the PCB board above which the printed moulds and the pipetted PDMS_CB are located. The photo captures the moment when the air bubbles are coming out of the moulds

The mould was then placed in the oven at 125 °C for 20 min, so that the PDMS_CB could cross link and cure as shown in Figure 6.8.

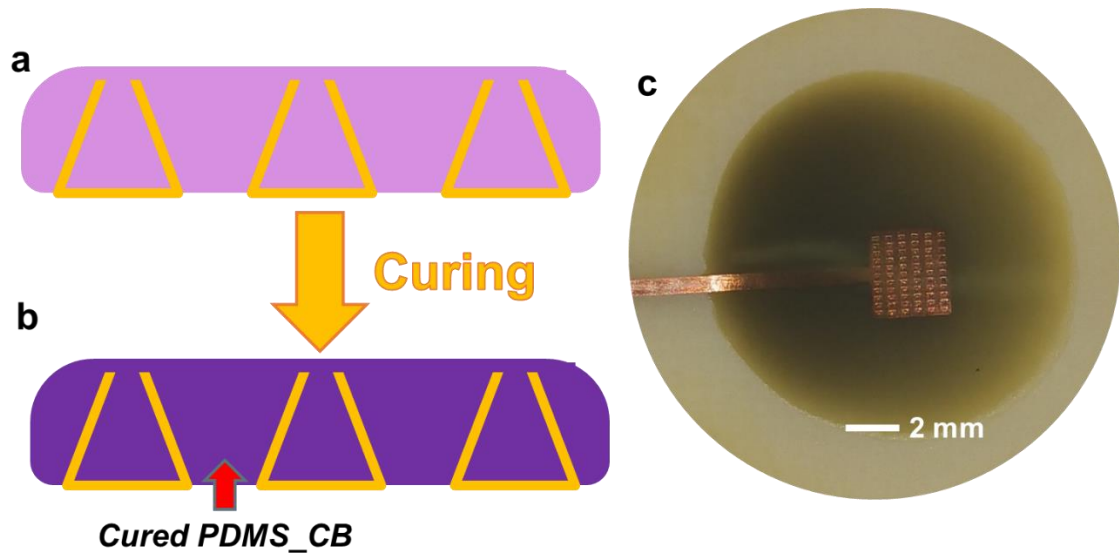


Figure 6.8: a.) Schematic showing the side view of the mould completely filled with uncured PDMS_CB b.) Schematic showing the cured PDMS_CB encompassing the mould c.) Photo of the cured PDMS_CB film on the PCB

Small incisions around the mould were made with a razor blade and then tweezers were used to peel the cured film off the mould. The incisions helped to easily remove the cured film. After peeling, the PDMS_CB remained inside the pyramidal moulds, because the film broke off at the tips of the pyramidal mould during the peeling process (Figure 6.9). This was also facilitated due to the nature of the mould-moulding interface, where the PVP mould is hydrophilic and the PDMS_CB moulding is hydrophobic, so that they both struggle to form any bonds between each other. Bonds would have made the break off more challenging or potentially not even possible. Our developed approach introduces an extra lever to vary and alter the dielectric medium, where the gaps between the pyramids can be filled with another high relative permittivity material. This was not possible previously, because a base layer was a mandatory by-product of photolithography, which also reduced the overall base capacitance because of the extra thickness of the dielectric medium. The base

layer is non-existent in our developed approach and thus the space in between the pyramids can be filled with other high relative permittivity materials.

Additionally, the peeled off film could be used as the master for soft lithographic moulding, because it contains the pyramidal indentations. To do this, the PDMS soft mould needs to be treated with UV plasma and trichloro-fluorosilane for every moulding as reported by other groups (Clementine M. Boutry et al., 2015; Tee et al., 2014). We are not aware of any approach for moulding micropyramids where the mould and the moulding were both made together in the same process and were both of use.

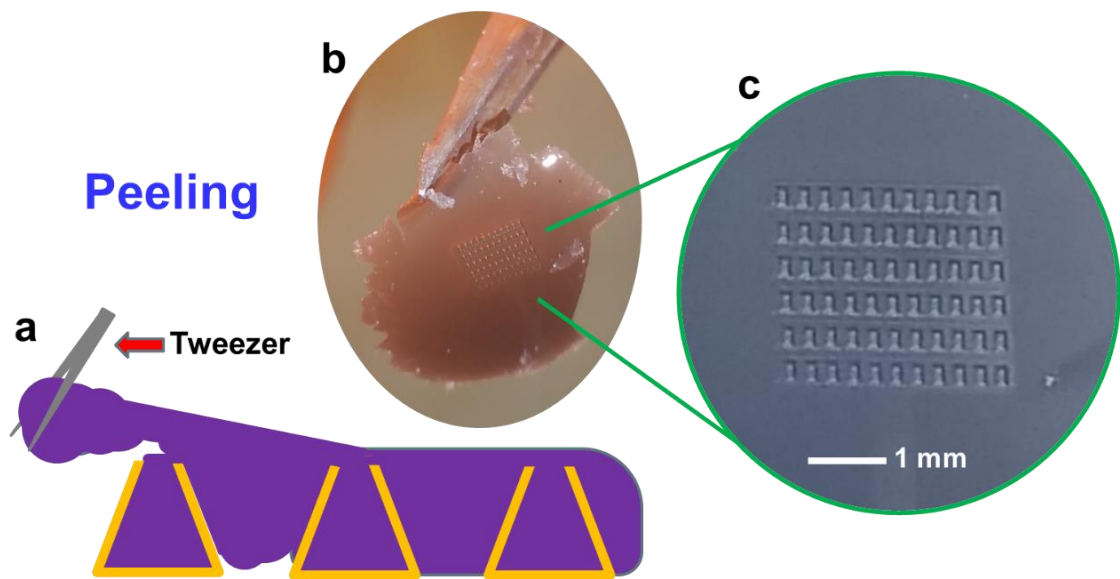


Figure 6.9: a.) Schematic showing the side view of the mould and the cured PDMS_CB layer getting peeled off the mould b.) Photo of the tweezers holding peeled film c.) Photo of the peeled film, where the rectangular pyramidal indentations are visible

The filled mould was then pipetted with DI water droplets and consequently washed away, leaving behind the cured PDMS_CB moulding as shown in Figure 6.10. This fabrication approach saves time and paves the way into micrometre scale rapid prototyping of 3D pyramidal arrays.

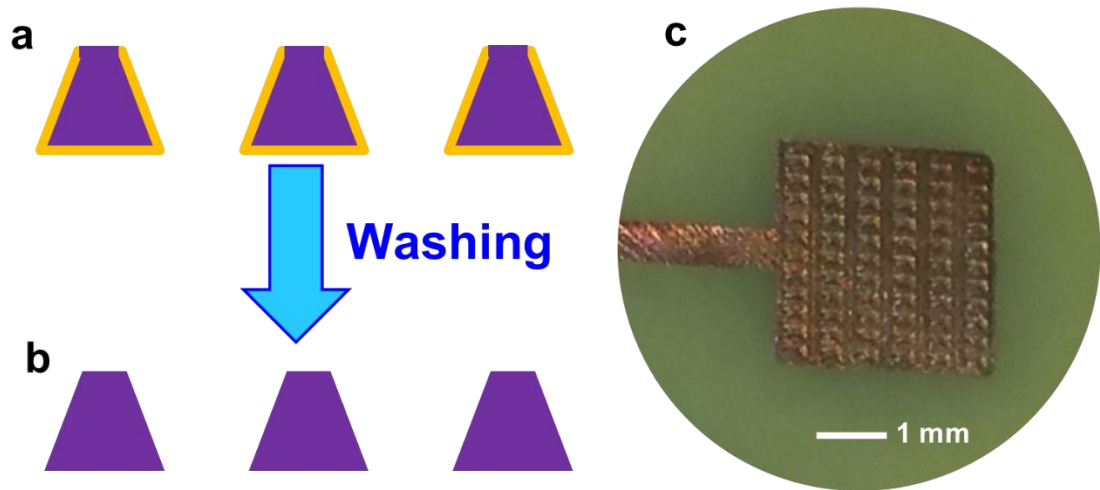


Figure 6.10: a.) Schematic showing the side view of the printed mould with cured PDMS_CB filling b.) Schematic showing a cured PDMS_CB moulding after the mould is washed away with DI water droplets c.) Photo of the cured PDMS_CB mouldings on a copper electrode on PCB, forming the microstructured dielectric layer of the capacitive pressure sensor

This technique allowed the micro pyramidal structured arrays to be printed in square based form (aspect ratio 1:1) again, since the vacuum chamber could remove the previously encountered problem of trapped air bubbles at the bottom of the square based pyramidal moulds. Arrays of varying sizes were printed ranging from 4 pyramids to 121 pyramids.

Figure 6.11 shows an overview of the main fabrication process adapted for the making of microstructured capacitive pressure sensors reported in this work.

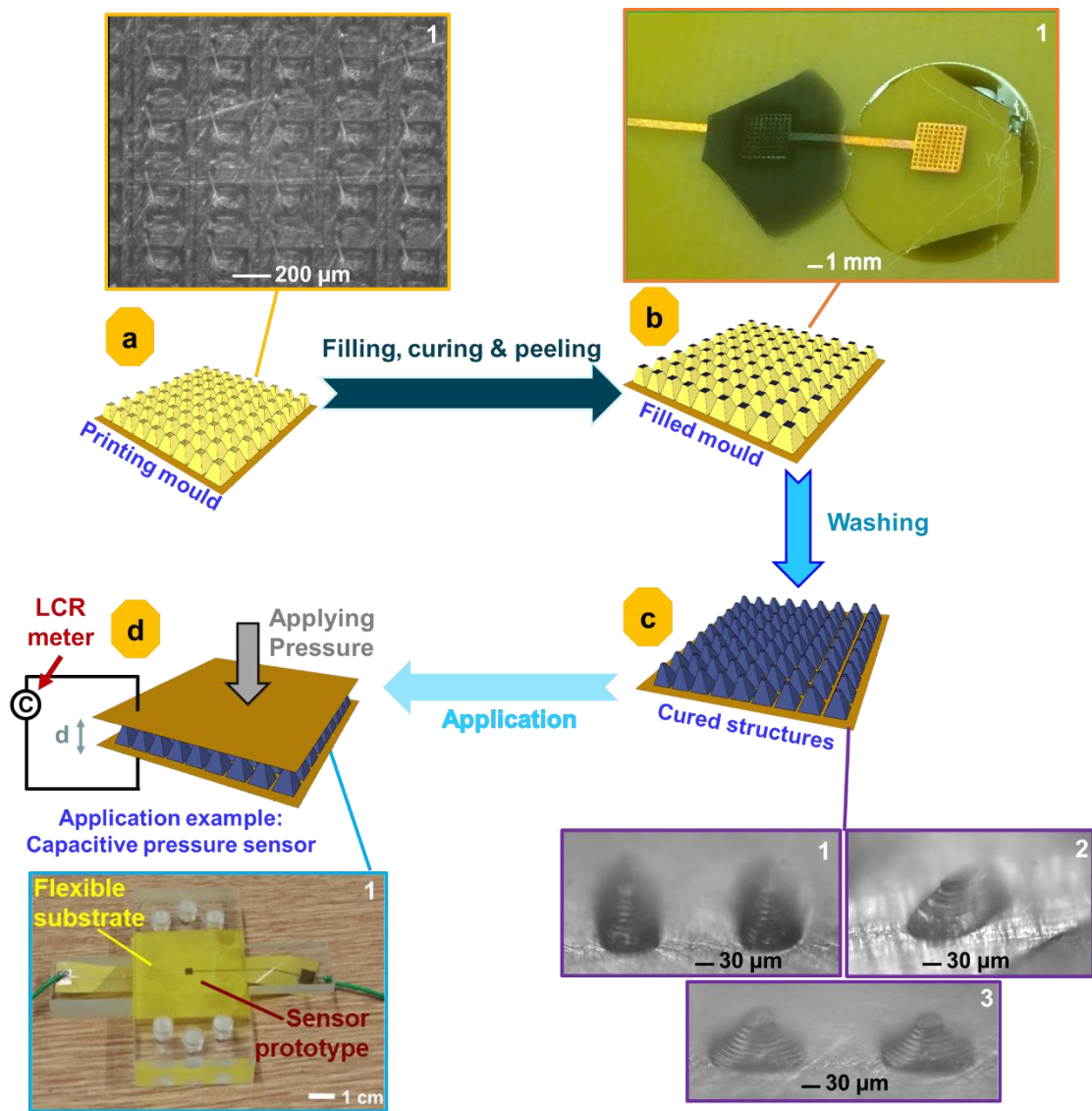


Figure 6.11: Overview of making an array of a pyramidal microstructured dielectric layer using direct-write printing for rapid prototyping water soluble micro moulds a.) Schematic showing a printed micro mould array on copper on a PCB: 1) Photo showing the top view of the mould on a copper PCB b.) Schematic showing filled mould: 1) Photo of peeled film and filled moulds on a copper PCB c.) Schematic showing cured structures with the PVP mould washed away: 1) Photo showing the side view of a cured rectangular based pyramidal moulding consisting of PDMS_CB(0.1%) and the 2) angled view. 3) Photo of a cured square based pyramid moulding consisting of PDMS d.) Schematic showing how the fabricated microstructured dielectric medium is incorporated in between two electrodes for capacitive pressure sensing, where a change in applied pressure represents a change in capacitance, which is measured using a LCR meter: 1) Photo of the Cjig measurement platform with flexible PCBs mounted

6.2 Results & Discussions

6.2.1 Structured dielectric

The effects of microstructuring the dielectric layer were demonstrated by comparing the relative capacitive change of an unstructured film dielectric layer and a microstructured dielectric layer both of 100 μm thickness. The electrode size was a 3 mm square. The (unstructured) film was made by printing a 100 μm high wall near the electrode edges, then filling with PDMS(10:1), curing at 125 °C for 20 minutes in oven, cooling down outside the oven for 10 minutes and then washing away the mould. The pyramid micro mould array consisted of 81 pyramids (9 by 9), where each pyramid mould had dimensions of 200 μm x 200 μm and 100 μm high. Then the PCB with the fabricated microstructured dielectric layer is mounted onto the Cjig and the capacitance changes with respect to the applied pressure (acrylic plates) are recorded as detailed in chapter 4.

Figure 6.12 shows the comparison of the relative capacitance change as a function of applied pressure for the unstructured and structured (micro pyramids) PDMS film. The structured sensor demonstrated a ~30-fold increase in sensitivity in comparison to the unstructured sensor in the low pressure region of <300 Pa, a ~9-fold increase for the medium pressure region of 0.3 - 1 kPa and a 5-fold increase for the high pressure region of >1 kPa. This is similar to Mannsfeld et al. (Mannsfeld et al., 2010) who reported a 30-fold increase in sensitivity (0.55 kPa^{-1}) when comparing structured and unstructured PDMS film. But this sensitivity was over a greater pressure range of up to 2 kPa. However, the sensor was bigger, where the electrode size was a 8 mm square, in contrast to the 3 mm square that was used in this work.

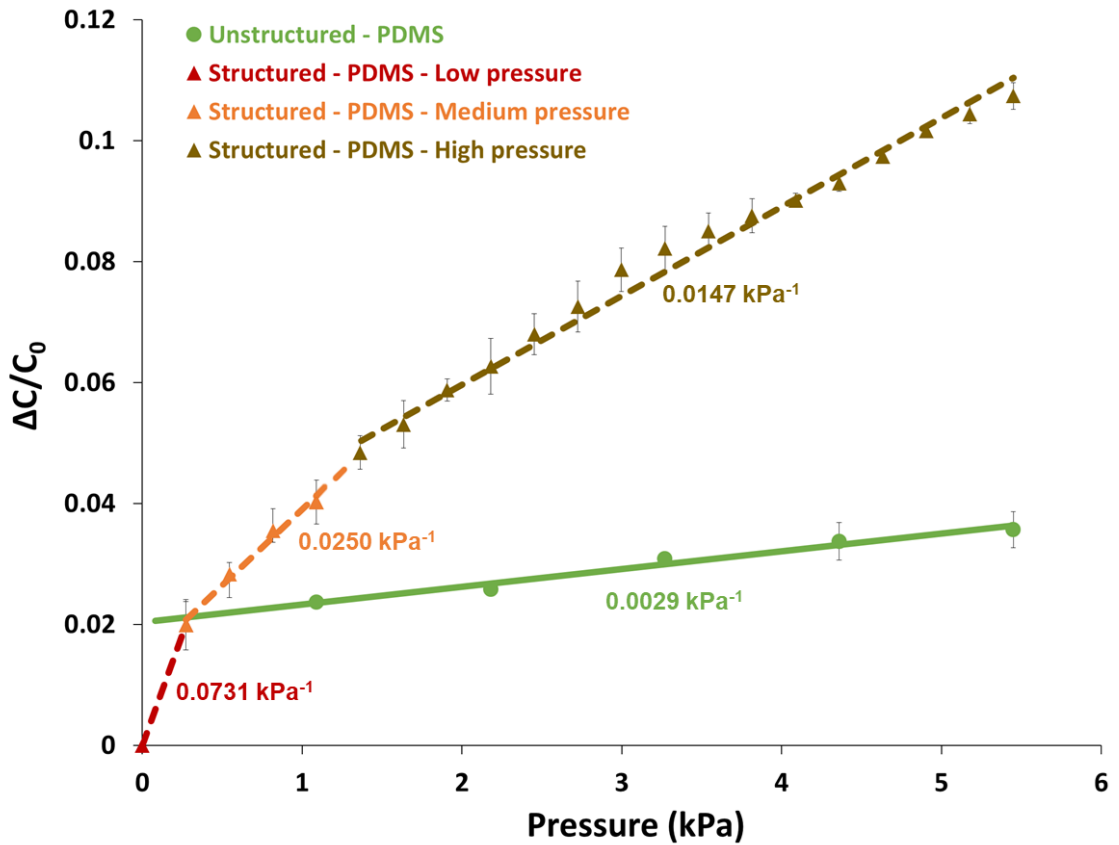


Figure 6.12: Comparison of sensor response for structured dielectric (81 pyramids, each $200\ \mu\text{m} \times 200\ \mu\text{m}$ and $100\ \mu\text{m}$ high) and unstructured dielectric (flat film, $100\ \mu\text{m}$ high) layer made up of PDMS(10:1)

6.2.2 Enhancement of base capacitance via carbon black nanoparticles

The relative permittivity of polymer media have been reported to become enhanced by incorporating conductive nanoparticle fillers - like carbon nanoparticles – below their percolation threshold (Achour et al., 2008; Chen et al., 2018; Jang et al., 2016; Matchawet et al., 2016; Nanodomains et al., 2017; Wolff and Wang, 1993). The importance of a good dispersion of nanofillers in the polymer matrix has also been highlighted (Tan et al., 2012). However, incorporating them into an elastomeric matrix is expected to reinforce the matrix and consequently increase its overall Young's modulus, effectively reducing its deformability. A reduction in deformability would reduce the sensitivity of the sensor.

In this work it was tested that, if by introducing a small amount of <1 wt% carbon nanoparticles (~40 nm particle size) into a PDMS matrix, it was possible to benefit from the nanoparticle fillers in terms of enhanced relative permittivity – resulting in a higher base capacitance – while preserving a similar effective Young's modulus and not significantly impacting on the deformability of the elastomer. For this a small amount of carbon black nanoparticles (0.1 wt%) was dispersed into PDMS as described in chapter 5 and microstructured into 81 pyramids with the same dimensions as mentioned in the previous section 6.2.1. The sensors were characterised repeatedly using the LCR meter (LCR-821, Iso-tech) and acrylic plates as detailed in chapter 4.

Figure 6.13 shows the sensor capacitance response for the microstructured dielectric layer consisting of pure PDMS pyramidal structures (200 μm x 200 μm each) that were 100 μm high in contrast to the exact same structures with additionally 0.1 wt% carbon black nanoparticles incorporated into the PDMS microstructures, highlighting the impact of incorporating nanoparticles into PDMS on the base capacitance. The base capacitance increased from 1.6 pF (just PDMS microstructure) to 1.8 pF (12% increase) for the PDMS_CB microstructure. However, the PDMS_CB had a higher standard deviation sensitivity than the pure PDMS microstructures. This could be attributed to the nanoparticles relocating and impeding with formed elastomeric chains when a strain is applied to the sensor, so that when the pressure is removed and reapplied to the sensor, the deformation is not the same as the first deformation.

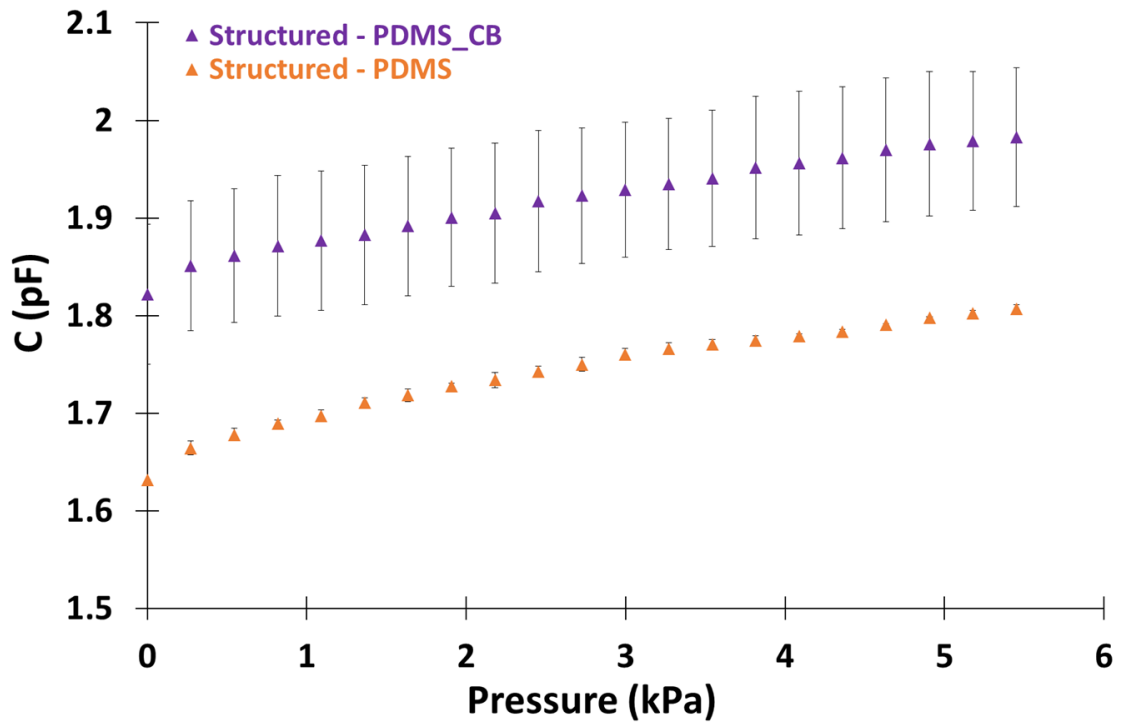


Figure 6.13: Comparison of sensor response for the pure PDMS structured dielectric (81 pyramids, 100 μm high)

Figure 6.14 shows the relative capacitance as a function of pressure for both sensors, highlighting the mechanical impact of incorporating carbon black nanoparticles into a PDMS matrix. The sensitivities of the PDMS_CB sensor are almost the same as the pure PDMS sensor for all three pressure regions (low, medium and high). This shows that the mechanical properties of the PDMS_CB composite microstructure are similar to the pure PDMS microstructure. However, it should be noted that increasing the carbon black nanoparticle concentration will result in a higher effective Young's modulus, which will reduce the deformability and hence reduce the overall sensitivity of such a sensor. Additionally, an increase in nanoparticles will not only result in a higher base capacitance but will also result in a reduced amount of repeatability. This was because the nanoparticles can agglomerate more and can impede or reduce viscoelasticity (Roland, 2011; Wolff and Wang, 1993), or potentially even break

elastomeric chains – permanently deforming the structures – making the pressure sensor unusable.

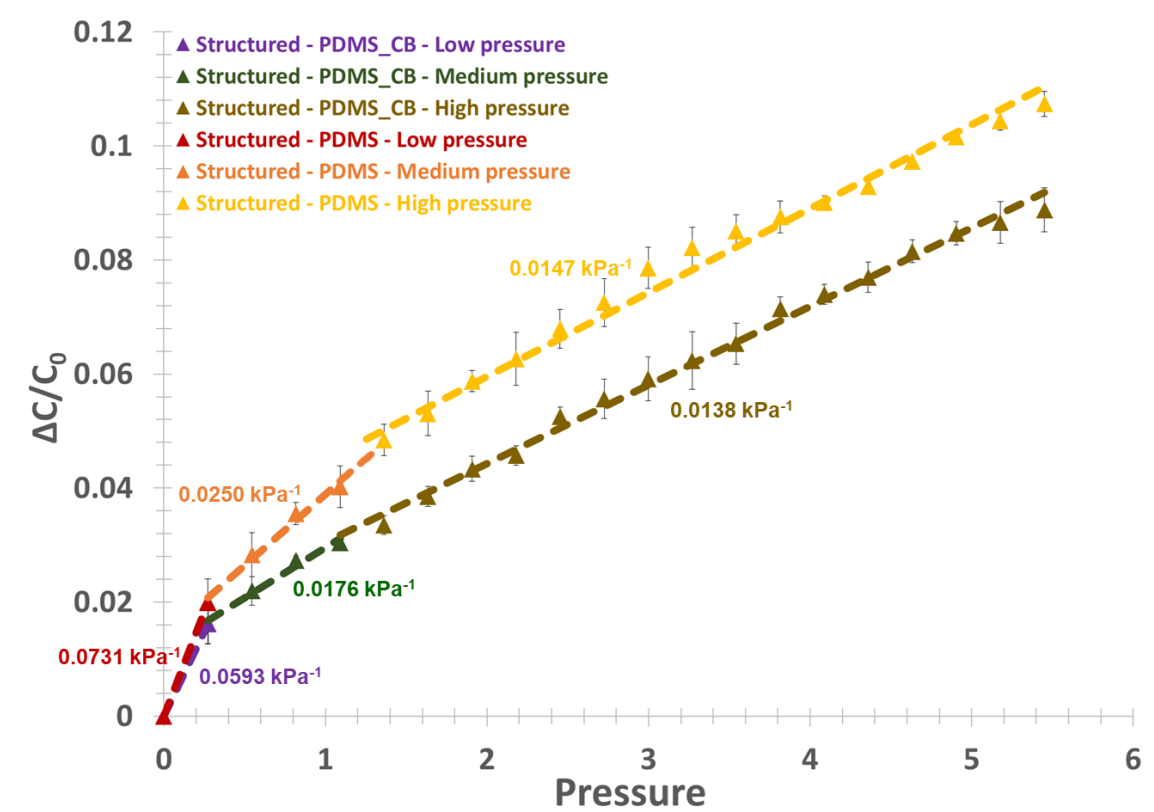


Figure 6.14: Comparison of sensor response for a pure PDMS structured dielectric (81 pyramids, 100 μm high) and a PDMS with CB (0.1% filler concentration, 81 pyramids, 100 μm high)

In order to completely benefit from incorporating CB nanofillers and maintain a low standard deviation across measurements, the dispersion of the fillers has to be improved as suggested by other groups (Xu et al., 2004).

6.2.3 Higher structures for a bigger sensing range

The sensing range of microstructured capacitive pressure sensors is limited by the thickness and Young's modulus of the dielectric medium (height and material of the pyramidal mouldings). Thus in order to increase the sensing range, higher pyramidal moulds (array of 2 x 2) were printed on 3 mm square copper electrode on FR4 (Figure 6.15a). The sidewall angle was programmed in PIMikroMove to be at 54.7°, which is the pre-dominantly reported side wall angle for microstructured capacitive pressure sensors made via photolithography (Clementine M Boutry et al., 2015; Mannsfeld et al., 2010; Tee et al., 2014; Yang et al., 2019). The pyramidal moulds each consisted of a square base of 800 µm and a height of 650 µm. The moulds are then filled with PDMS(10:1), cured and washed away. The scanning electron microscope (SEM) images of the resulting cured PDMS mouldings are shown in Figure 6.15b (top view) and Figure 6.15c (angled side view). Acrylic plates (each weighing 1 g) were used to apply pressure on the developed sensor (Figure 6.15d). The relative capacitive pressure change as a function of applied pressure was compared to the dielectric layer consisting of 81 PDMS pyramidal structures that were ~100 µm high (Figure 6.15e - red line) and the dielectric layer consisting of 4 higher (~650 µm) pyramidal structures (Figure 6.15e - green line). The sensing range for the higher (~650 µm) PDMS structured sensor was 4 times greater (0 to 21.8 kPa) than the ~100 µm PDMS structured sensor (0 to 5.45 kPa).

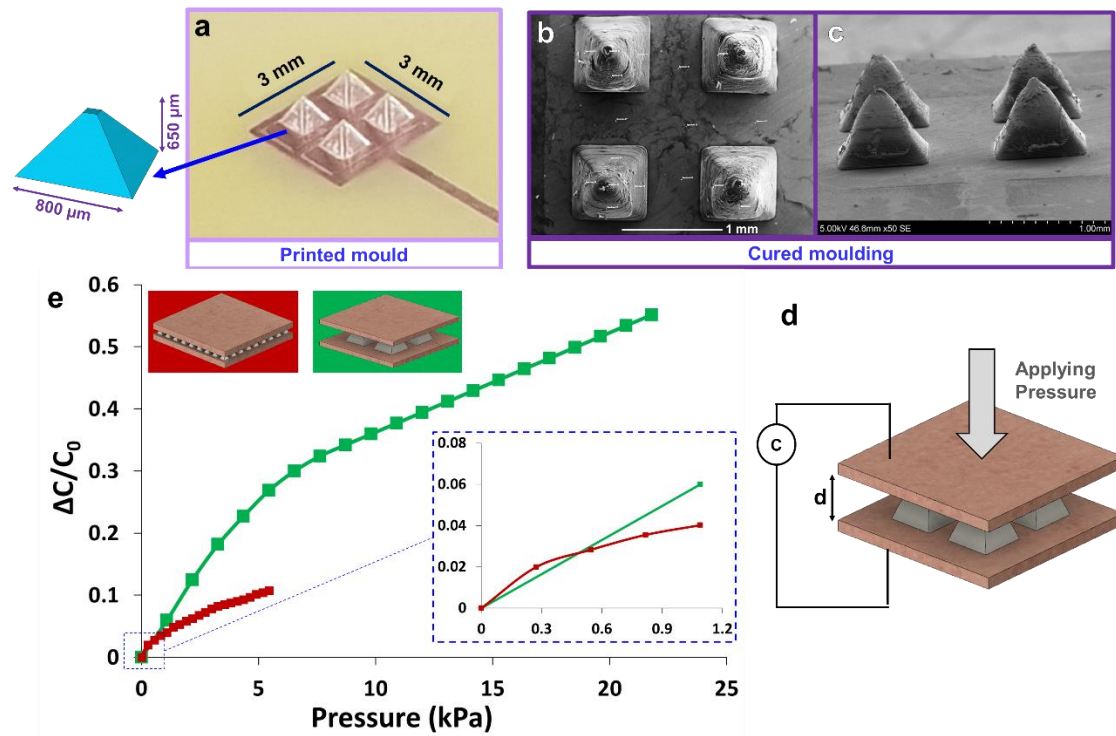


Figure 6.15: Higher structures for the bigger sensing range a.) Photo of 4 printed pyramidal moulds of dimensions 800 μm square base and height of 650 μm on 3 mm square copper electrode on top of FR4 (PCB). b.) SEM image of moulding top view and c.) angled view. d.) Schematic of capacitive pressure sensing with a 2 x 2 pyramid array e.) Relative capacitive pressure change as a function of applied pressure for dielectric layer consisting of 81 pyramidal structures that are ~100 μm high (red line) and a dielectric layer consisting of 4 higher (~650 μm) pyramidal structures (green line) Inset: Showing an expanded view of the graph for <1 kPa.

6.2.4 Increased electrode area for enhanced sensitivity

In order to enhance the sensitivity of the sensors and test the repeatability of the manufacturing approach, 4 identical pyramid moulds were printed on to the corners of 3 electrode sizes (49 mm², 25 mm² and 9 mm²) (Figure 6.16a). The moulds were filled with PDMS(10:1), cured and washed away, leaving behind the PDMS moulding (Figure 6.16b) as described previously.

Next, the sensors were characterised following the same procedure as described previously, where square acrylic plates (1 g and 0.25 g) are used to

apply pressure on the sensors and the corresponding capacitance reading is recorded from the LCR meter (Figure 6.16c).

The relative capacitance response of the three developed sensors with respect to the pressure experienced by the pyramid structures is compared in Figure 6.16d and the corresponding gradient values of all three sensor responses for 2 regions of applied mass ≤ 0.5 g (≤ 12 kPa) and ≤ 2.5 g (≤ 50 kPa) is shown Figure 6.16e. When the applied pressure is ≤ 12 kPa and ≤ 50 kPa, the gradients across all three sensors are the same 0.004 kPa^{-1} and 0.002 kPa^{-1} , respectively. This was expected since the structures for all three sensors were fabricated with the same dimensions, so that the pressure experienced by the structures across all three sensors is the same, leading to the same gradient. Additionally, it should be noted that for the ≤ 12 kPa region the gradient is higher than the ≤ 50 kPa region, because of the higher deformations/per kPa experienced in the top layers of the pyramid structures. This also shows that our approach of micro moulding pyramids is reproducible, since the measurements were taken across 3 different electrode sizes (49 mm^2 , 25 mm^2 and 9 mm^2) but each of them had 4 pyramids with a square base of $332 \text{ }\mu\text{m}$ and height of $250 \text{ }\mu\text{m}$.

Using the same data, the relative capacitance response of the three developed sensors with respect to the pressure experienced by the sensor is shown in Figure 6.16f. The sensing range is different for each of the sensors, despite the exact same mass – 0 to 2.5 g in increments of 0.25 g acrylic plates - being applied to all three sensors. This is because of the effective area of the sensors being different from each other. So that even with the same force being applied to all three sensors, the pressures the sensors experience are different (9 mm^2

→ 0 to 2.7 kPa, 25 mm² → 0 to 0.98 kPa and 49 mm² → 0 to 0.5 kPa). The corresponding sensitivity (gradient) values of all three sensor responses for the 2 regions of applied mass (≤ 0.5 g and ≤ 2.5 g) are shown in Figure 6.16g. The sensitivities increase with increase in electrode area for both regions of applied mass (≤ 0.5 g and ≤ 2.5 g), as expected. Thus the sensor consisting of the 7 mm square electrode and 4 pyramids (332 μ m square base and 250 μ m high) was used to test the response time and relaxation time (section 6.2.5).

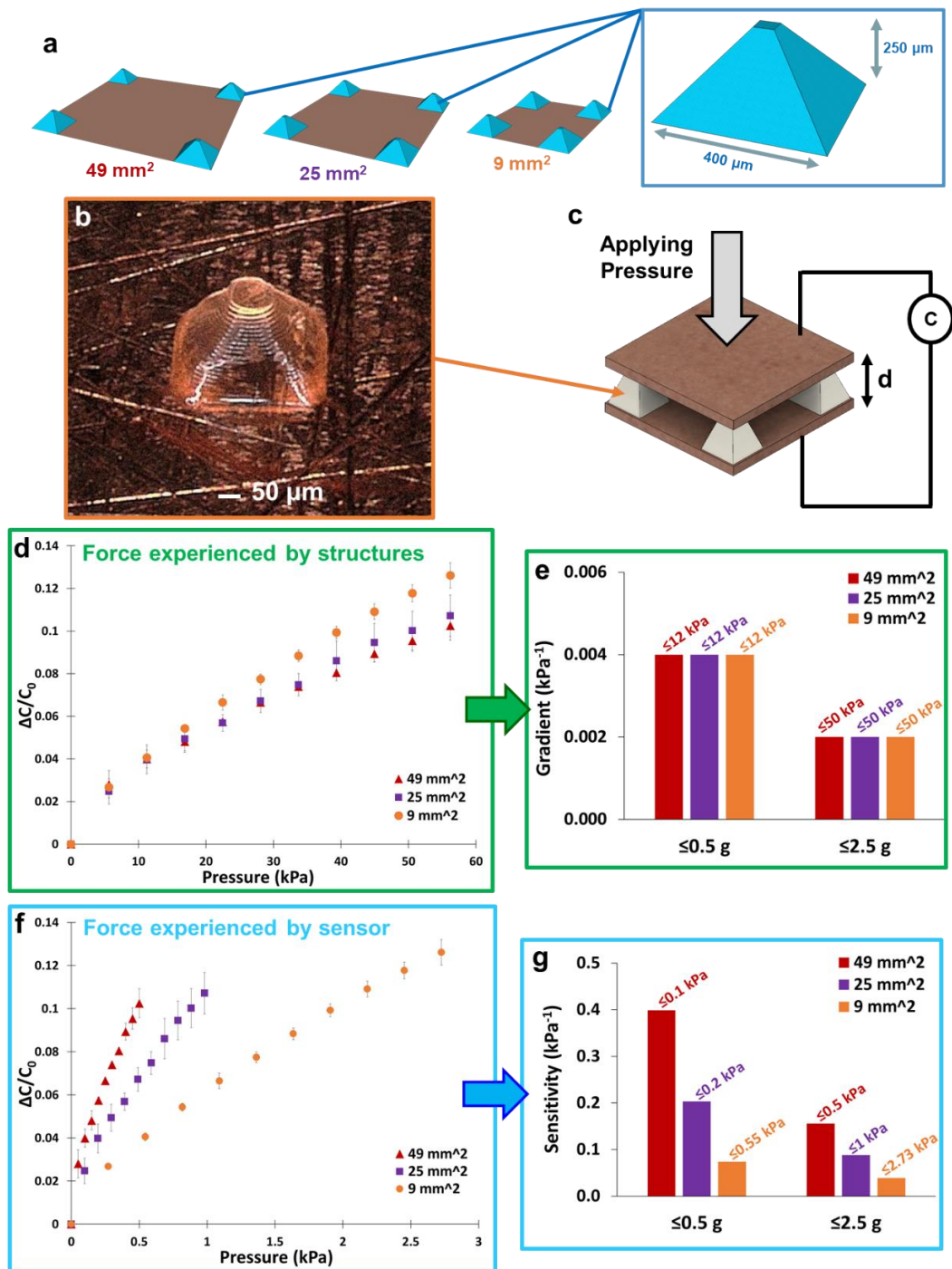


Figure 6.16: Effect of varying electrode area a.) Schematic illustrating 4 identical pyramid moulds printed on the corners of each of the electrodes, which are of varying size of 49 mm² (7 mm square), 25 mm² (5 mm square) and 9 mm² (3 mm square) b.) Microscopic image of individual PDMS moulding on one of the corners of the 7 mm square electrode c.) Schematic illustrating capacitive pressure sensing concept for the developed sensor d.) Relative capacitance response of the three developed sensors with respect to the pressure experienced by the pyramidal structures e.) Corresponding gradient values of all three sensor responses for 2 regions of applied mass (≤0.5 g and ≤2.5 g) f.) Relative capacitance response of the three developed sensors with respect to the pressure experienced by the sensor g.) Corresponding gradient values of all three sensor responses for 2 regions of applied mass (≤0.5 g and ≤2.5 g)

6.2.5 Response and relaxation time

To characterise the response time of the developed W:7 mm x L:7 mm x H:250 μm sensor (with 4 pyramids (332 μm square base and 250 μm high), one on each corner), the sensor was connected to a semiconductor device analyser (B1500a Semiconductor Device Analyzer (SDA), Keysight technologies), which was calibrated and the error was compensated by following the steps in the supplier manual, that can be found in the appendix (A.5 Calibration of Keysight Semiconductor Device Analyser B1500a) (Keysight, 2019).

The response time is usually measured by placing an object onto the sensor and observing the time taken by the sensor to achieve 90% of the stable capacitance output (Huang et al., 2019). However, while placing the object onto the sensor it is challenging to avoid any vibrational interference. Thus in order to avoid this, water droplets of $\sim 10\text{ }\mu\text{l}$ each were used to apply pressure onto the sensor. A micropipette was set to 10 μl and was subsequently loaded with DI water. The loaded micropipette was held $\sim 3\text{ cm}$ above the sensor and a $\sim 10\text{ }\mu\text{l}$ droplet was pipetted onto the sensor (Figure 6.17a). The capacitance change over time was observed on the SDA and the response time was obtained as $\sim 20\text{ ms}$.

Similarly, to characterise the relaxation time, a whiteboard marker pen ($\sim 12\text{ g}$) was placed on the sensor. The white board marker pen was then knocked off the sensor by hand and the capacitance drop was observed on the SDA. The relaxation time obtained was $\sim 30\text{ ms}$.

Figure 6.17b summarises the response and relaxation times of some recently reported microstructured capacitive pressure sensors in comparison to our developed 7 mm sensor with 4 pyramids. Human touch (~15 ms) (Chortos et al., 2016b), auditory (~284 ms) and visual (~331 ms) (Shelton and Kumar, 2010) response times have been included to contrast the sensors' responses and relaxation times.

For most capacitive pressure sensors, it can be seen that the response time is the same or very similar to their respective relaxation time. It can be seen for the porous pyramid sensor developed by (Yang et al., 2019), the relaxation time (~100 ms) is double the response time (~50 ms). This ~50 ms difference could also be attributed to the porous surface texture of the pyramidal mouldings. When a force is applied onto the sensor, the air voids can easily collapse and compress, but upon removal of the force from the sensor the air voids can take longer to return into their original form of open air voids.

Similarly, in the case of our sensor the relaxation time was 10 ms slower than the response time. This could be attributed to the line indented surface of the pyramid mouldings, where the printed lines of the moulds left behind an imprint/indentation on the PDMS moulding.

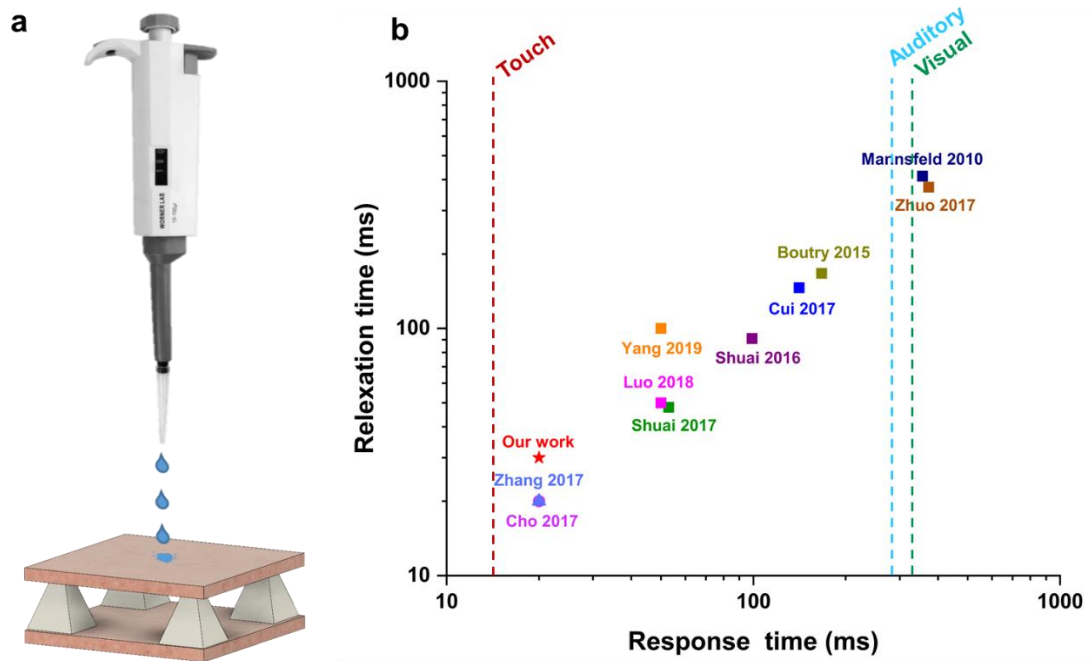


Figure 6.17: Response and relaxation time of the developed capacitive pressure sensor (Sensor size of 7 mm square base and 250 μm height) a.) Schematic illustrating water droplets being released from a micropipette ("Adjustable Micropipette 1 – 5 ml," 2018), where each water droplet is set to be 10 μl , thereby applying a pressure of 2 Pa to the sensor b.) Graph of relaxation time VS response time for the developed sensor and other reported capacitive pressure sensors (Clementine M Boutry et al., 2015; Cho et al., 2017; Cui et al., 2017; Luo et al., 2018; Mannsfeld et al., 2010; Shuai et al., 2017a, 2016; Yang et al., 2019; Zhang et al., 2017; Zhuo et al., 2017). Response times of human touch (Chortos et al., 2016a), auditory and visual response (Shelton and Kumar, 2010) are shown for comparison

However, our sensor is from amongst the sensors that have the shortest response and relaxation times, despite it having only 4 pyramid structures, which take up an area of less than 1% of the dielectric medium, the rest (99%) being air. This can attributed to the high ratio (S) - centre to centre pyramid spacing : pyramid base width – of 20.08 and the relatively high pyramid height of 250 μm of our sensor as demonstrated in Figure 6.18. In the case of the reported sensors, the number of pyramids exceeds our sensor's pyramid number of 4 by at least 1 order of magnitude. Additionally, for the reported sensors, the spacing between the pyramids is limited due to the risk of not providing enough support for the relatively low height pyramids ($\sim <40 \mu\text{m}$).

However, for our sensor, it was possible to limit the pyramid number to 4 due to increasing the pyramid dimensions – including the height - such that there is more spacing between the pyramids (due to the low pyramid number) without the fear of lack of support (due to higher pyramid dimensions). It should be noted that the increase in pyramid height – the thickness of the dielectric layer - leads to a decrease of base capacitance, which in turn leads to the need for more complex readout circuitry. However, in the case of our sensors, the base capacitance was still within the picoFarad range, just like the other reported sensors.

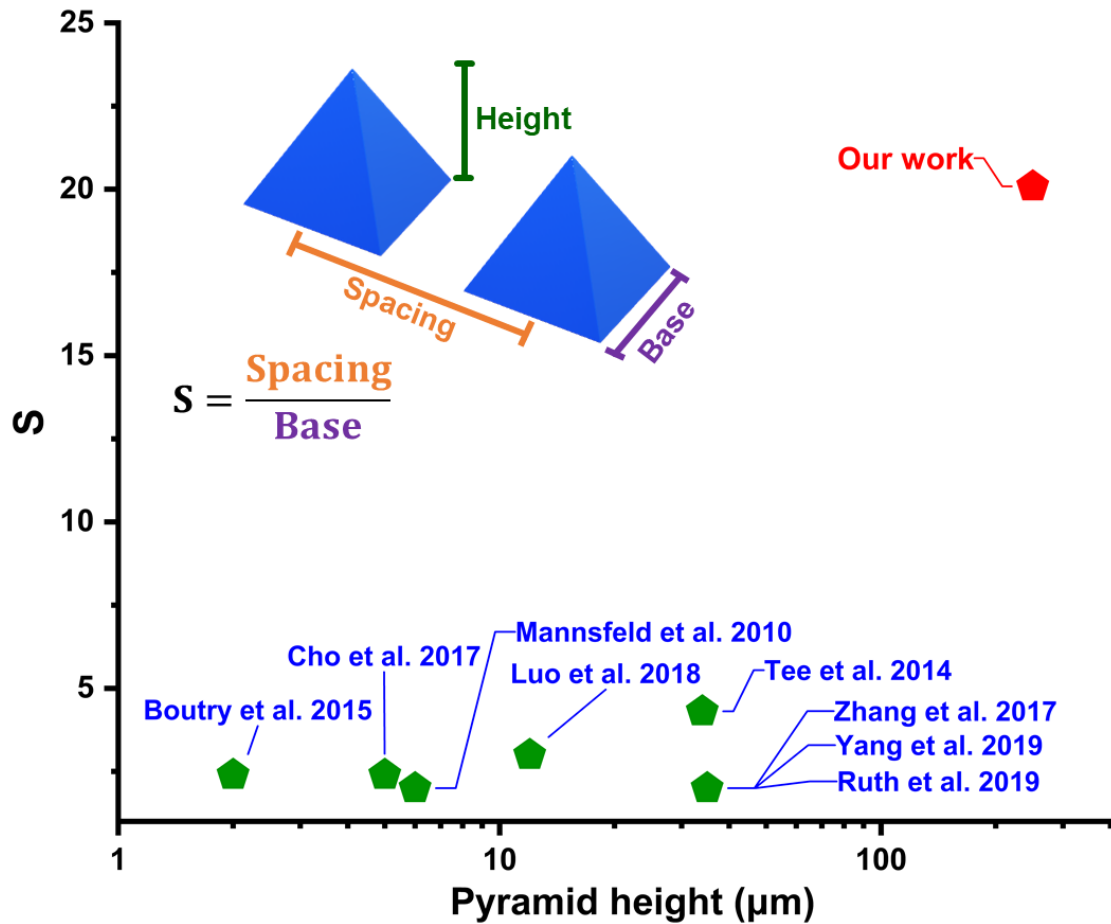


Figure 6.18: Ratio 'S' as a function of pyramid height for recently reported pyramid structured capacitive pressure sensors (Clementine M Boutry et al., 2015; Cho et al., 2017; Luo et al., 2018; Mannsfeld et al., 2010; Ruth et al., 2019; Tee et al., 2014; Yang et al., 2019; Zhang et al., 2017) and our sensor (red)

6.2.6 A pressure sensing ring

A 6 sided 'pressure sensing ring' prototype was designed as a potential medical device for doctors and surgeons to wear and use. This ring potentially can hold up to 5 miniaturised sensors – one on each side - and a wireless (Bluetooth low energy) readout circuitry on the 6th side to transmit the data to a phone.

The first prototype was developed for proof of concept and consisted of a 9 mm² capacitive pressure sensor containing a dielectric medium made up of an array of 2 x 2 PDMS pyramids (each pyramid having a 332 µm square base and being 250 µm high) – one in each corner - glued on to a 3D printed ring. It should be noted that the 4 pyramids only used up ~5% of the dielectric medium and the rest (~95%) of the dielectric medium was air.

The 2 x 2 pyramid array was direct-write printed on a 32 µm (12 µm copper and 20 µm FR4) thin flexible PCB (Espanex, Holders Technology). In order to level this thin flexible PCB for printing, a few water droplets (~40 µl) were placed between a glass slide and the flexible PCB. The printed moulds were then filled with PDMS(10:1) via vacuum filling and cured at 125 °C for 20 minutes. The film is peeled off and the mould washed away so that the 4 structured PDMS mouldings remain behind on the flexible PCB. The flexible PCB is wrapped and glued onto a 3D printed (UP mini 2 ES, Tiertime) hexagonal ring (A.6 Hexagonal ring design) with the help of adhesives (Figure 6.19a). Flexible wires are fixated with copper tape to the bottom of the ring where the electrical traces that connect to the square electrodes end. The exposed electrode traces and copper tape patches are covered with insulating tape to avoid any parasitic interferences (Figure 6.19b). The flexible wires are extended via SMB male to male coaxial cable – for better signal quality – and connected to an evaluation board (EVAL-AD7745/46EB, ANALOG DEVICES) which is connected to a

laptop with the associated evaluation software (AD7745/AD7746 Evaluation Software, ANALOG DEVICES) (Figure 6.19c). The pressure sensing ring was worn on the little finger and the sensor containing side of the ring was pressed onto a volunteer's (29 year old male) arm above the radial artery (Figure 6.19d-e). The sensor was able to provide a real-time pulse signal of the radial artery (Figure 6.19f). The signal does show some drift, especially during the 1.2 to 2.6 s time frame. This could be due to human errors such as small wrist movements, which are difficult to avoid. However, the close-up of a single pulse signal (Figure 6.19g) was able to distinguish between the percussion wave (P-wave), the tidal wave (T-wave) and the diastolic wave (D-wave). The digital volume pulse time ($t_{R1}-t_{R2}$), radial augmentation index (R_2/R_1) and diastolic augmentation index (R_3/R_1) were calculated to be 0.186 s, 0.586 and 0.278, respectively. These values can be used to test for arterial stiffness (Nichols, 2005). The resting heartbeat of the volunteer according to the measurements is at ~80 beats/min, which lies within the healthy resting heart rate region of 60 to 100 beats/min for adults (MacGill, 2017).

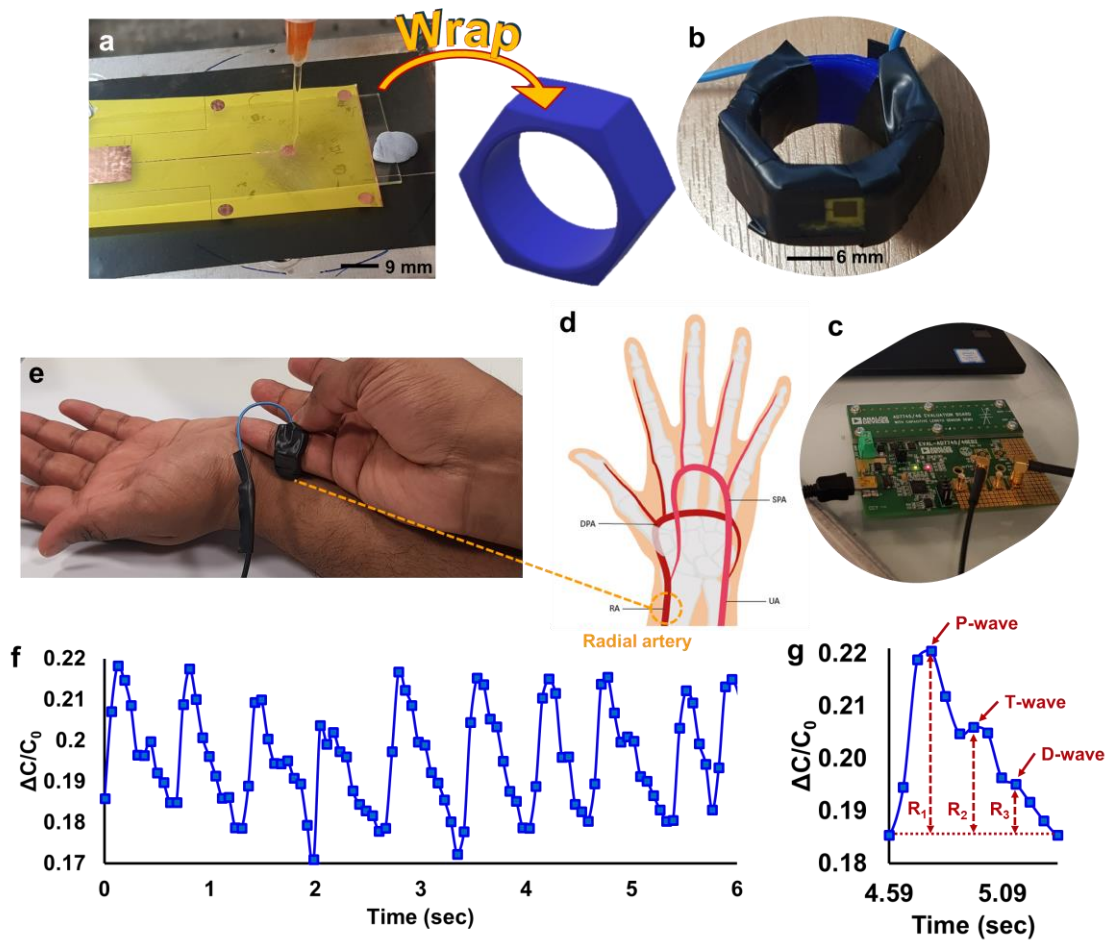


Figure 6.19: Fabricating the prototype of a pressure sensing ring a.) Direct-write printing pyramidal mould array 2 x 2 (each element having a 400 μm square base and being 250 μm high) on a 3 mm square electrode on a flexible PCB (Espanex, Holders Technology). In order to level the flexible PCB, a few water droplets ($\sim 40 \mu\text{l}$) were placed between the glass slide and the flexible PCB. The printed moulds are then filled with PDMS(10:1) via vacuum filling and cured at 125 $^{\circ}\text{C}$ for 20 minutes. The film is peeled off and the mould is washed away so that the structured PDMS moulding remains behind on the flexible PCB. The flexible PCB is wrapped onto a 3D printed (UP mini 2 ES, Tiertime) hexagonal ring with the help of adhesives. b.) Image showing the complete sensor package integrated on one side of the hexagonal ring and the electrode trace paths being covered with black insulating tape to avoid external interferences. c.) Attached using copper tape to the ring are flexible wires and SMB coaxial cables leading to readout circuitry (Evaluation Board EVAL-AD7745/46EB, ANALOG DEVICES) d.) Schematic of the left hand showing the location of the radial artery (Roh and Lee, 2018) e.) Image showing the pressure sensing ring being employed on a wrist f.) to provide a real-time pulse signal from the radial artery. g.) Close-up of measured and detailed single pulse

6.2.7 Change in dimensions from mould to moulding

The change in structural dimensions from the user programmed dimensions in PIMikroMove to the dimensions of the resulting PDMS mouldings were characterised for the pyramid array of 81 pyramids, where each pyramid mould was programmed with a square base of 200 μm and height of 100 μm . The moulds were printed with a 15 μm nozzle. Figure 6.20a is an SEM image of the array of 81 pyramid mouldings of PDMS(10:1) on top of a PCB (3 mm square electrode on top of FR4), where Figure 6.20b is an SEM image of one of these pyramidal mouldings. The red dashed trapezoid drawing represents an exemplar measurement of pixel dimensions of a pyramidal moulding. This was repeated across all of the 81 pyramids and converted into micrometre dimensions. Figure 6.20c summarises the mean measured values of the top, bottom and height of the mouldings. The top part of the moulding ($51.18 \pm 5.07 \mu\text{m}$) differs $\sim 48 \mu\text{m}$ from the program (100 μm) and the bottom part of the moulding ($145.93 \pm 6.02 \mu\text{m}$) differs $\sim 54 \mu\text{m}$ from the program (200 μm). Based on 1000s of print runs, a rule of thumb for the printed filament size is that it is equal to the nozzle aperture $\times 1.5$, due to surface wetting, etc. (see chapter 3). So for the case of a 15 μm nozzle, the expected filament size is $\sim 23 \mu\text{m}$. This would mean that the difference between the program and the moulding should be $\sim 23 \mu\text{m}$ as well. However, the difference is at 48 and 54 μm , which is more than double $\sim 23 \mu\text{m}$. This is due to the accumulation of ink on the nozzle over the printout (Figure 6.20d), which results in more ink being drawn out of the nozzle, leading to bigger filaments being printed. This narrows the printed mould, smudges the edges of the pyramid mould and results in conical pyramid moulds. This can be overcome by reducing the ink wetting of the printing nozzle, which is detailed in chapter 7.

The height reduces by only $\sim 7 \mu\text{m}$ from mould (100 μm) to moulding ($92.80 \pm 6.91 \mu\text{m}$). This reduction is much lower than the other dimensions because the height of the mould and its filling level are very similar. The height of the moulding is slightly lower due to slight sagging of the initial mould layers, which is because of the weight the printed lines exert on the bottom layers. However, the standard deviation of the moulding height values was highest ($\pm 6.91 \mu\text{m}$) in comparison to the top part ($\pm 5.07 \mu\text{m}$) and the base ($\pm 6.02 \mu\text{m}$) of the pyramidal moulding. This can be attributed to the difficulty in controlling the exact breaking point of the cured PDMS layer during peel off.

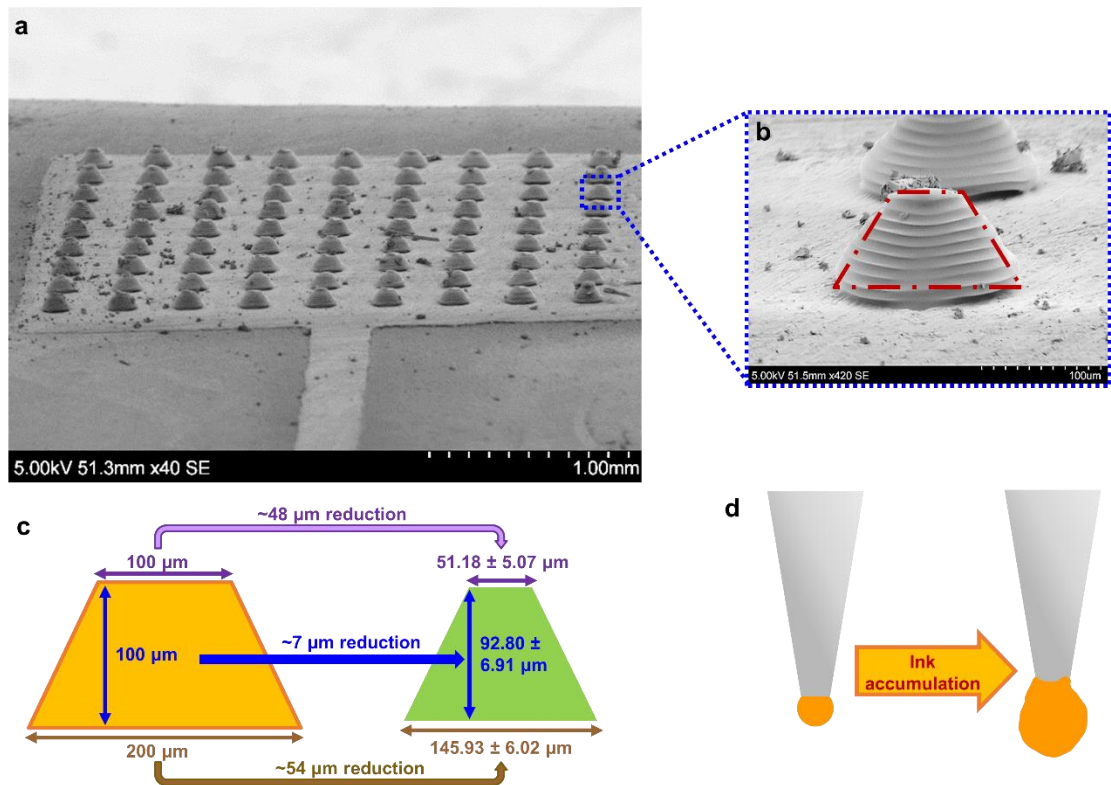


Figure 6.20: 81 pyramid mouldings a) SEM image of the angled side view of the microstructured PDMS(10:1) dielectric moulding layer (81 pyramids, each 200 μm x 200 μm , 100 μm high) on top of 3 mm square copper electrode on FR4 (PCB) b) SEM image of the angled side view of an individual pyramid moulding c) Schematic demonstrating the change in dimensions from the user programmed structure to the actual mean dimensions of the top, bottom and height of a trapezoidal pyramid measured across the 81 pyramid mouldings d.) Schematic demonstrating ink accumulation on the nozzle over printing duration

6.3 Conclusions

- 2.5D hexagonal mould structure arrays of 9 hexagons were printed, filled and moulded. It was observed that due to ink accumulation on the printing nozzle over the print duration, the printed mould suffered many discrepancies such that the mouldings were oval structures instead of hexagonal structures. Additionally, 3D pyramid mould square based structure arrays of 25 were printed, but suffered from air getting trapped in the bottom of the micro moulds during the filling process.
- This was overcome by printing higher aspect ratio pyramids ($1:n$, $n>1$) with one new nozzle per new structure. These rectangular pyramids gave the trapped air room to escape the mould during the filling process.
- In order to fill all moulds in parallel, vacuum filling was used, where the filler ink was deposited above the printed mould and desiccated so that the moulds were filled through vacuum action and the air leaves the moulds.
- The developed approach in this project introduces more control to alter the dielectric medium, where the gaps between the pyramids can be filled with another high relative permittivity material. This is not possible with photolithography, because a base layer was a mandatory by-product of photolithography. This extra base layer also reduces the overall base capacitance, because capacitance is inversely proportional to the distance between the electrodes. The base layer is non-existent in our developed approach and thus the dielectric medium is limited to the height of the pyramids and the space in between the pyramids can be filled with other high relative permittivity materials.
- A structured sensor with an array of 81 pyramids (100 μm high) was compared to an unstructured sensor (100 μm high). The structured sensor

gave an enhanced sensitivity as previously reported (Mannsfeld et al., 2010).

- The base capacitance was enhanced by filling the moulds with PDMS_CB(0.1 %) nanocomposite, without significantly affecting the sensitivity
- The pyramid structure heights were increased to 650 μm to enable a bigger sensing range of up to $\sim 22\text{kPa}$
- The effect of varying the electrode area was demonstrated by fabricating 4 pyramids onto 9 mm^2 , 25 mm^2 and 49 mm^2 electrode areas. The sensor with the biggest area (49 mm^2) demonstrated the highest sensitivity. Repeatability of the fabricated sensors was demonstrated by comparing the relative capacitance of the sensors as a function of the force experienced by the structures instead of the force experienced by the sensor.
- The response and relaxation time of the 49 mm^2 sensor were characterised to be $\sim 20\text{ ms}$ and $\sim 30\text{ ms}$, respectively. These times are amongst the fastest response and relaxation times reported (Clementine M Boutry et al., 2015; Cho et al., 2017; Cui et al., 2017; Luo et al., 2018; Mannsfeld et al., 2010; Ruth et al., 2019; Shuai et al., 2017a, 2016; Tee et al., 2014; Yang et al., 2019; Zhang et al., 2017). This was attributed to the high ratio 'S' which was made possible due to the increased pyramid structure dimensions. Additionally, it should be noted that the 4 pyramids use up less than 1% of the area of the dielectric medium, the rest (99%) being air. Our approach is an effective way to minimise planar space, which is highly valued in the microelectronics industry (Liu et al., 1999).
- A pressure sensing ring prototype was developed that could potentially be worn by doctors and surgeons for real-time pressure monitoring of patients.

The sensor on the ring was 9 mm² in size and was able to successfully monitor the radial pulse signal of a 29 year old male.

- It was shown that the changes from the user programmed PIMikroMove code to the final physical moulding demand an improvement in print resolution of the pyramid mould arrays via reducing the wetting of the nozzle. The next chapter addresses some ways of improving the print resolution.

Chapter 7 - Improving print resolution

This chapter demonstrates certain ways of improving the print resolution of previously reported (Ahn and Lewis, 2014) silver inks and in particular the developed PVP ink for better print resolution, which would also lead to better mould quality as highlighted in the previous chapter.

This is primarily achieved by reducing the amount of nozzle wetting during the printout. A polymer blend ink is also developed to reduce nozzle wetting and achieve higher resolution ($<10\text{ }\mu\text{m}$) 3D direct-write printing without wetting the nozzle. The ink is characterised rheologically and the chapter concludes with exemplar structures that were printed with the developed polymer blended ink.

7.1 Experimental procedure

7.1.1 Silver nanoparticle ink

Walker and Lewis (Walker and Lewis, 2012) demonstrated their unique reactive silver ink formulations, which were stable and worked well for direct-write printing. The reactive silver inks in this project were prepared in the same way, but the duration of mixing and settling conditions were different. In this project, 1 g of silver acetate is stirred using stir bar and hot plate mixer into 2.5 ml of ammonium hydroxide for 1 minute at room temperature. In order to reduce the silver ions to silver particles, 0.2 ml of Formic acid is added to the solution one drop at a time. This solution is then left overnight (12 h) in a refrigerator so that the larger particles settle to the bottom of the vial. The supernatant solution is filtered using a 0.2 μm syringe filter, one drop at a time into another vial. The filtered reactive silver ink is then ready for printing.

7.1.2 PVP/PVDF ink

The PVP ink developed and detailed in chapter 5 is a hydrophilic ink that readily wets the nozzle during array printing as highlighted in the previous chapter. In order to reduce the wetting on the nozzle, a hydrophobic ink was blended with PVP (Mw 360,000 Da, Sigma Aldrich) in a mutual solvent. The hydrophobic polymer used was Poly(vinylidene fluoride) (PVDF) (Mw ~530,000 Da, Sigma Aldrich) and the solvent was N,N-Dimethylformamide (DMF) (N,N-Dimethylformamide anhydrous 99.8%, Sigma Aldrich). The polymer blend was prepared by weighing out 70 wt% of DMF in a vial with a magnetic stir bar, then the 30 wt% polymer content was added in a ratio of 3:2 (PVP:PVDF). The content was left to stir on the hot plate at 60 °C and 350 rpm for 6 days (144h hours), after which the polymer blend (PVP/PVDF) was ready for printing.

7.2 Results & Discussions

7.2.1 Nozzle functionalisation

When printing with silver ink, after the initial fluid contact was made with the surface, the applied back pressure was removed by setting the pressure to 0 bar. This was done to avoid over wetting (Figure 7.1a), which occurred even for very small pressures of 0.01 bar. However, during the printout, the ink started to accumulate above the nozzle (Figure 7.1b) affecting the print resolution and quality of the printed S - pattern (Figure 7.1c). The line width was about 27 μm across the S - pattern, even though with a ~5 μm nozzle a line width of ~8 μm was expected. The accumulated ink on the nozzle made the 'effective printing nozzle' bigger than the actual nozzle aperture.

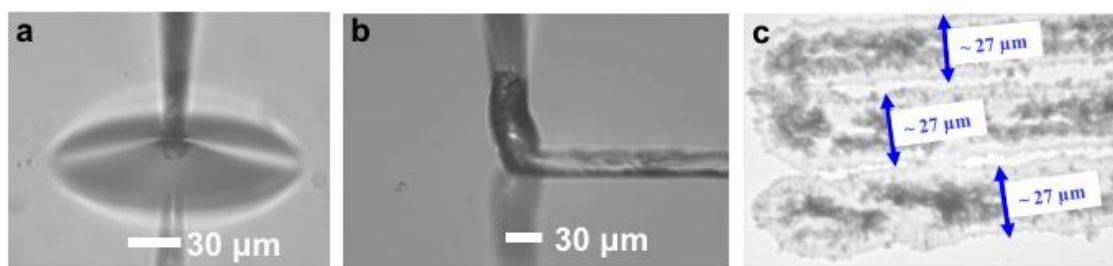


Figure 7.1: Ag ink printing: a.) Applied back pressure leading to over wetting b.) Ag ink accumulating above the nozzle while printing thus affecting resolution c.) Printed S- pattern ~27 μm line width

In order to overcome this, the nozzle had to be functionalised, so that the Ag ink would not wet the nozzle but rather the substrate. In order to test the suitability of the hydrophobic silicone polymer based product RainX (Rain-X Rain Repellent, Kraco Car Care International) for nozzle functionalisation, a glass slide was treated with RainX. Another 4 glass slides were prepared for comparison by treating one with ethanol, another one with isopropanol, another with acetone and one slide with no treatment at all. An Ag ink droplet was pipetted on each of the 5 slides (Figure 7.2a). The ink wets the untreated slide and the acetone pre-treated glass slides the most. The Ag ink for the RainX treated glass slide almost remained as a bead due to minimal wetting. Another Ag ink droplet was placed after one hour onto the RainX treated slide and it was still minimally wetting the slide and maintaining the bead form overall (Figure 7.2b). This suggested that RainX was very suitable for treating the glass nozzles that are used for printing, where the ink accumulation at the nozzle has to be minimised.



Figure 7.2: Ag ink droplet on pre-treated glass slides: a.) Wetting of Ag ink droplet on glass substrates pre-treated with different solvents b.) Ag ink droplet placed on the RainX pre-treated substrate after 1 hour

A simple setup was constructed (Figure 7.3a) in order to functionalise the nozzles that would be used for printing. The nozzle was attached to an empty syringe barrel, which was attached to a nitrogen supply and this was inserted into a vial full of RainX using a stage with incremental movements in the *millimetre* range. The amount of pressure applied for the functionalisation process varied according to the nozzle size. The ‘right amount of’ pressure was based on the pressure needed for the nozzle to just start producing bubbles inside the RainX solution. For nozzle sizes 1-3 μm , a pressure of 1 bar was applied. For nozzle sizes 4 - 10 μm , 0.8 bar was applied, whereas for nozzle sizes 11 – 20 μm only 0.2 bar was needed. For nozzles larger than 20 μm , a pressure of 0.1 bar was applied. In all cases, the nozzle was functionalised by applying back pressure and ‘bubbling’ the nozzle inside the RainX solution for 2 minutes. The effects of this functionalisation were very evident from the printing, such that the Ag ink could be printed without any accumulation on the printing nozzle (Figure 7.3b, c). This even enabled the printing of an array of S – patterns with one single functionalised nozzle (Figure 7.3d). However, this was achieved on glass substrates, whereas for printed flexible sensors, the potential

Ag interconnects would need to be printed on to flexible substrates such as PET (polyethylene terephthalate) sheets, OHP (overhead projector) sheets or polyamide films.

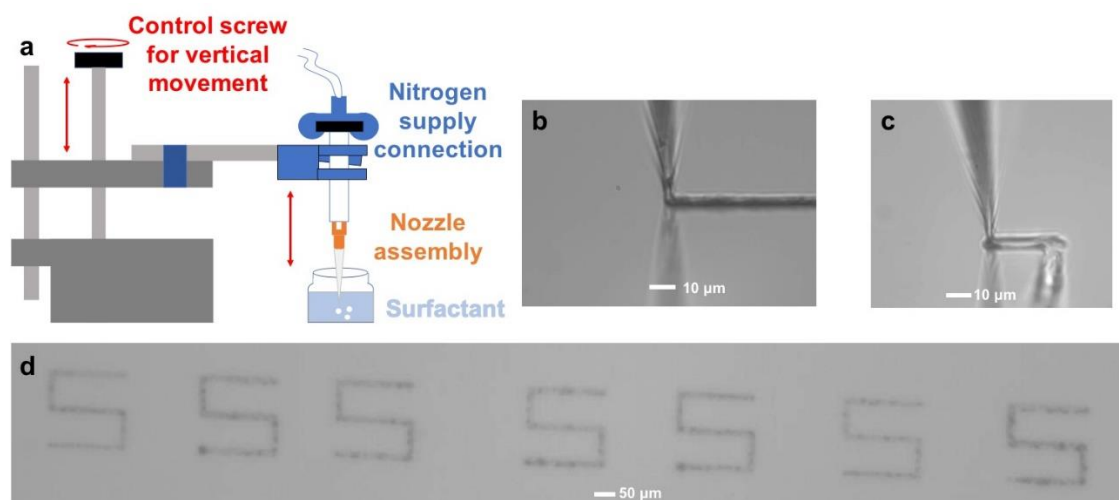


Figure 7.3: Ag ink printing with the functionalised nozzle: a.) Nozzle functionalisation setup b.) stable printing achieved by removing the back pressure and functionalizing the nozzle with RainX c.) ink is not accumulating on the nozzle even after printing corners d.) S-pattern repeatedly printed with a single functionalized nozzle with 0 bar back pressure

The same functionalised (with RainX) nozzles were used to print the developed PVP ink, but the ink kept wetting and fracturing the nozzle. This was the case even after bubbling in RainX for 10 minutes. Functionalisation of the nozzle with RainX was ineffective in preventing the printing nozzle from becoming wetted and fractured with PVP ink. Another approach was needed. Figure 7.4 demonstrates that using DI water droplets at the side of the substrate as nozzle cleaning stations, where the PVP ink accumulated nozzle (Figure 7.4b) would move away from the main print area and into a DI water droplet and then return via a different path back to the main printout with some of the previously accumulated ink having been washed away in the water droplet (Figure 7.4c). This approach did reduce the accumulated ink, but did not eliminate all of the accumulated ink.

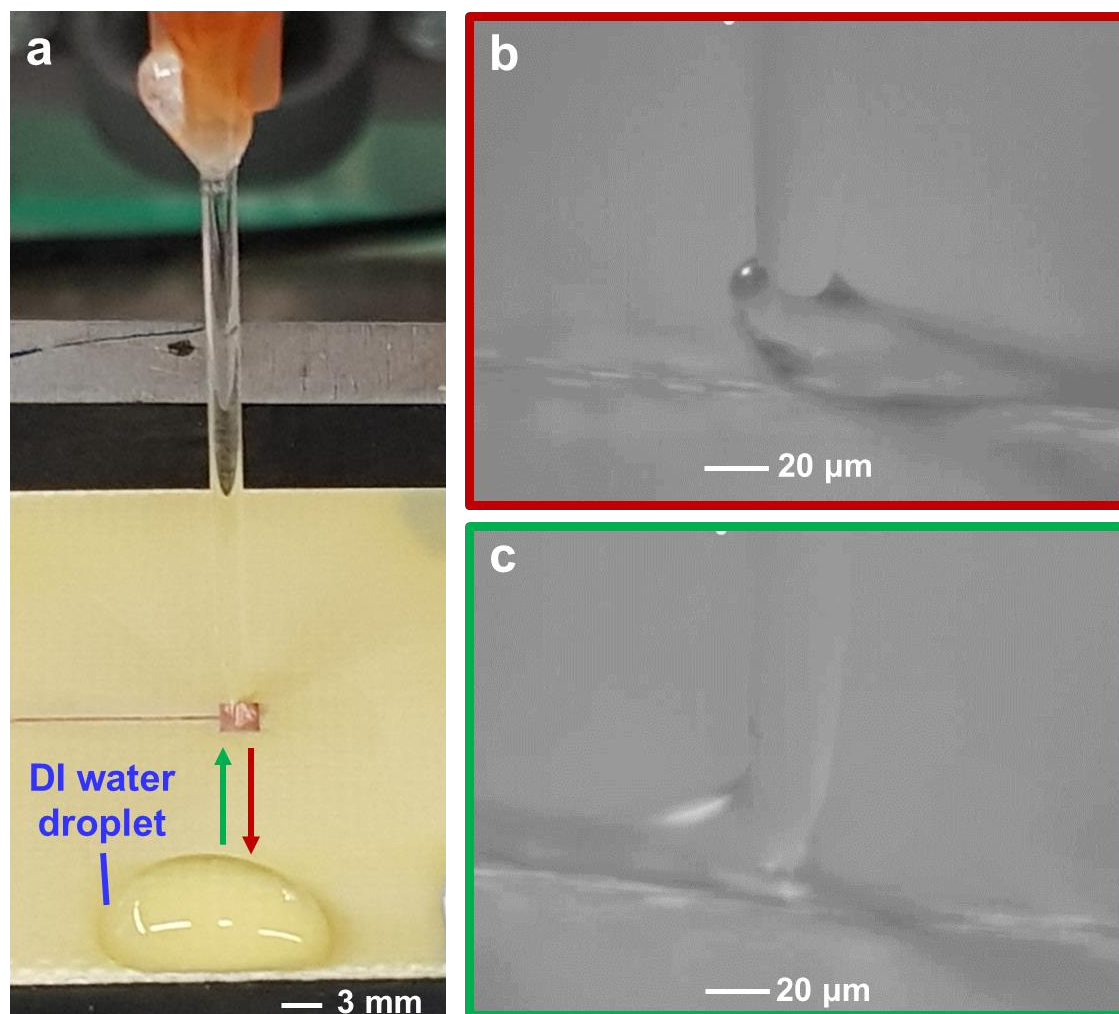


Figure 7.4: Nozzle cleaning stations: a.) nozzle printing on FR4 with a DI water droplet at the side of the substrate b.) PVP ink accumulated nozzle moving into a water droplet c.) printing nozzle after moving out of the water droplet

7.2.2 Rheology of PVP/PVDF blend

The developed PVP/PVDF blend was characterised rheologically to obtain the viscosity and viscoelasticity using the same rheometer setup and test parameters as described in chapter 5. Figure 7.5a shows the viscosity of the developed 30 wt% PVP ink and PVP/PVDF blended ink as a function of shear rate. The PVP/PVDF blended ink has a higher zero shear viscosity (112 Pa.s) than the 30 wt% PVP ink, as expected, since there was an increase in molecular weight (Wang et al., 2014). For low shear rates ($<0.1 \text{ s}^{-1}$), the PVP/PVDF ink also shows some shear thickening (as do 20 and 30 wt% PVP),

which can be attributed to intermolecular entanglements that can form during low shear rates (Vrahopoulou and McHugh, 1987). These entanglements are destroyed during the higher shear rates ($>0.1 \text{ s}^{-1}$), leading to a reduced viscosity (shear thinning). The standard deviation in the shear rate region of 2 to 8 s^{-1} is higher than the other regions. This could be due to a human error such as uneven ink loading on the Peltier of the rheometer during rheology studies. Uneven ink loading would result in different viscosity readings for the same shear rate.

Figure 7.5b demonstrates the viscoelastic properties of the polymer blend, where in comparison to the 20 wt% PVP ink, the G' has increased from $\sim 3 \text{ Pa}$ to $\sim 233 \text{ Pa}$, and the G'' has increased from $\sim 22 \text{ Pa}$ to $\sim 400 \text{ Pa}$. Since the PVP/PVDF ink has a higher molecular weight than PVP alone, an increase in storage and loss modulus is expected (Oser and Marvin, 1963). The polymer blend has more strength (G') and could easily break the nozzle if it was able to adhere to the nozzle when coming out of it. However, the hydrophobicity – low surface energy – of PVDF impedes the blend from accumulating at the nozzle. This enables higher resolutions ($<10 \text{ }\mu\text{m}$) 3D structures and arrays to be direct-write printed without wetting and fracturing the printing nozzle. Exemplar printed structures using the PVP/PVDF ink are shown in the next section.

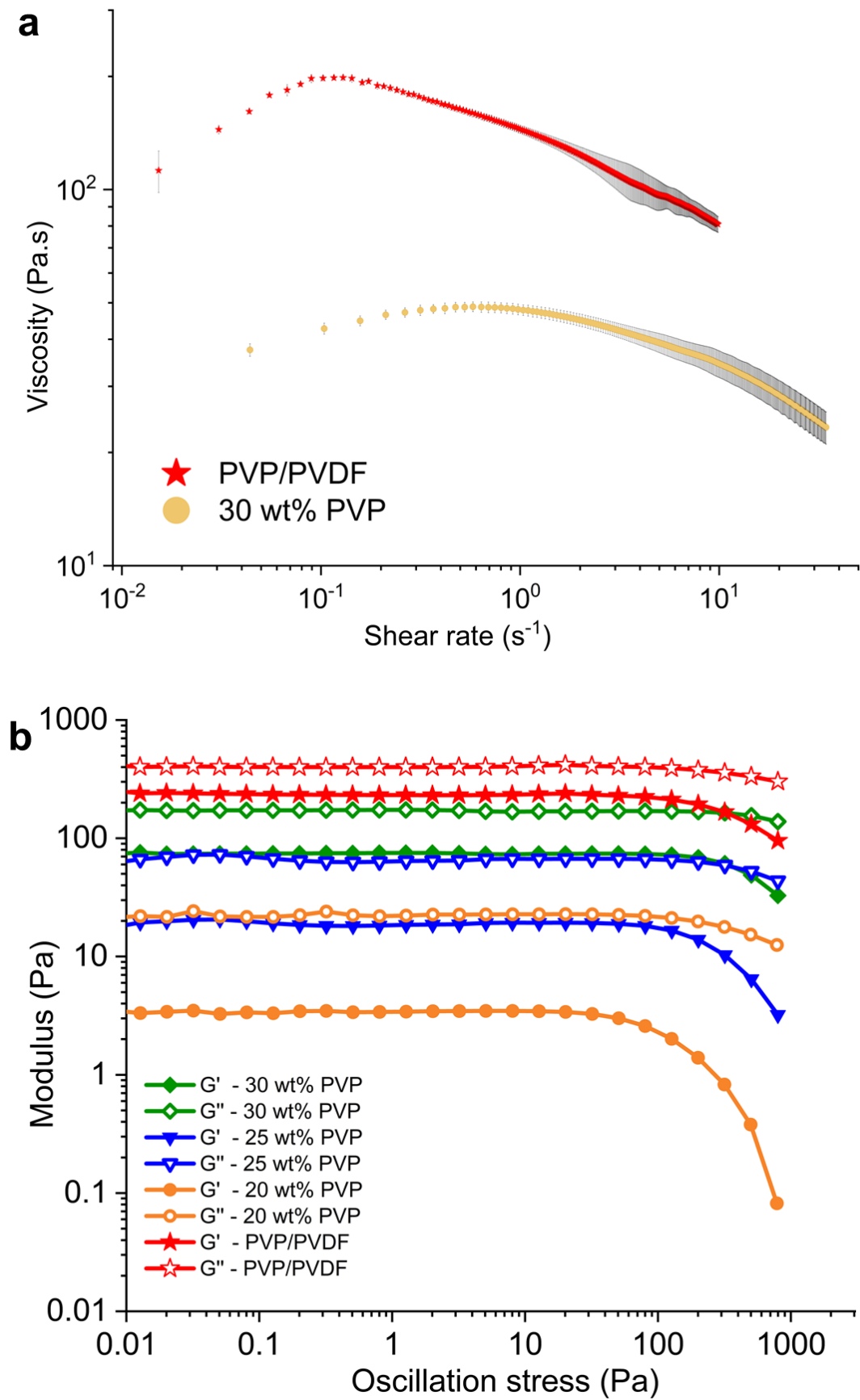


Figure 7.5: a) Viscosity as a function of shear rate and b.) G' and G'' as a function of oscillation stress for the PVP/PVDF and PVP inks

7.2.3 Exemplar prints

The developed PVP/PVDF ink was printed at the same speed of 0.2 mm/s. Figure 7.6a shows high-resolution lines $\sim 5\ \mu\text{m}$ printed in the shape of consecutive squares using a $5\ \mu\text{m}$ nozzle. The same pattern was reproduced on stainless steel foil with $100\ \mu\text{m}$ interline spacing and also $200\ \mu\text{m}$ interline spacing as shown below in Figure 7.6a,b.

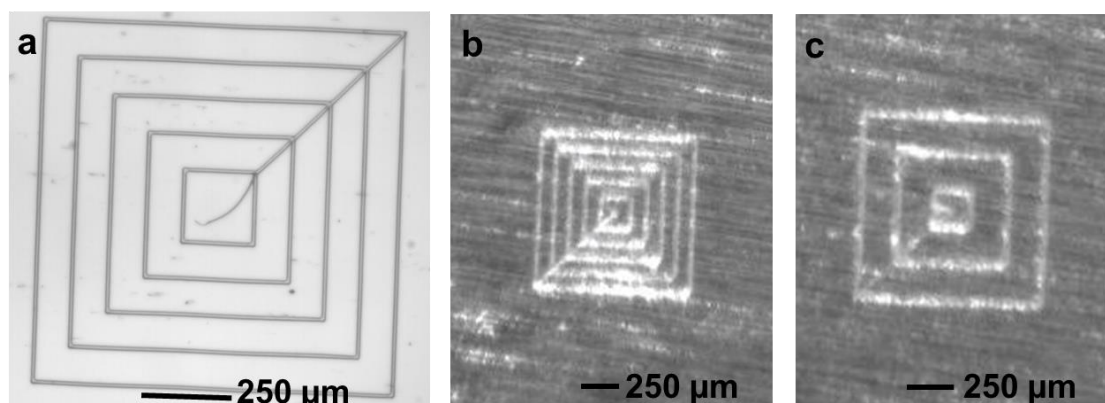


Figure 7.6: a.) A consecutive squares pattern printed with a $\sim 5\ \mu\text{m}$ nozzle on glass. b.) Same pattern printed on stainless steel with interline spacing of $100\ \mu\text{m}$ and c.) with interline spacing of $200\ \mu\text{m}$

Other structures that were printed include the diamond pattern (Dpattern) as shown in Figure 7.7. The pattern starts and ends at the same point, facilitating the nozzle to start printing the next layer from the exact same starting point for each consecutive layer. The pattern was printed successfully on various substrates including polyimide, copper and stainless steel (Figure 7.7a-c). It was successfully able to build over 100 layers (Figure 7.7c-f). The corners of the structure (Figure 7.7e,f) demonstrate the improved printing quality, since the corners are clear and pointed and not rounded.

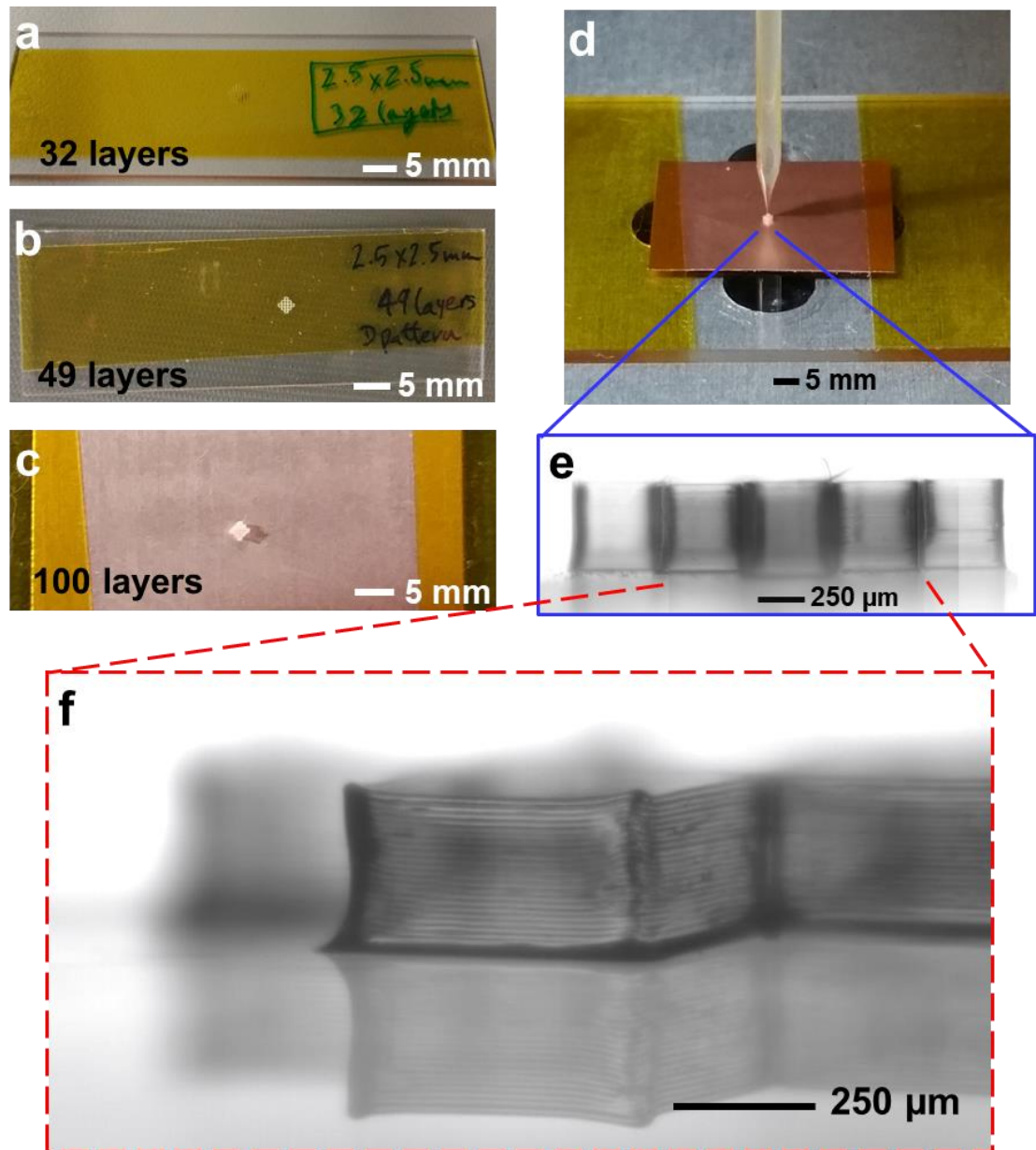


Figure 7.7: a-c.) A D-pattern printed on polyimide and copper for varying layers/heights d.) A D-pattern with 100 layers zoomed in while the nozzle is printing. e.) Side view of the printed D-pattern under the microscope and f.) an angled view.

A 30-layer high hexagonal structure was successfully printed with a 1-3 μm nozzle on polyimide as shown below in Figure 7.8a-c. The printed feature maintained its structure with the wall thickness uniformly being 3 μm wide even after 30 layers of printing, without any stringing.

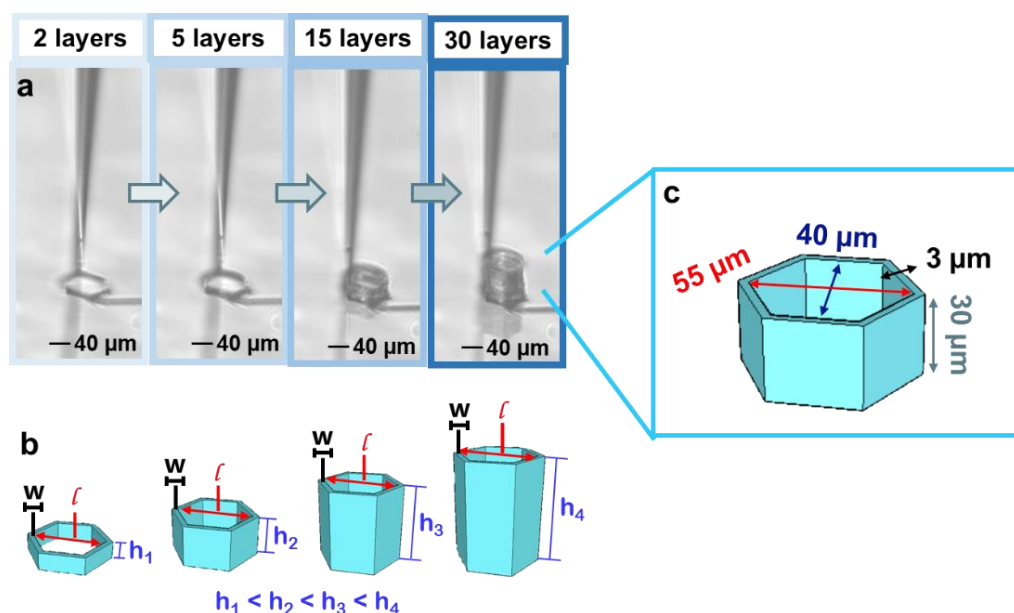


Figure 7.8: a.) Hexagonal structure printed on polyimide up to 30 layers b.) Schematic overview of the printout showing that wall thickness and the diameters of the hexagon remain constant throughout c.) Schematic of the resulting 30 µm high hexagon with a constant wall thickness of 3 µm

7.2.4 Array printing

Ink accumulating at the nozzle and either clogging up, fracturing the nozzle or reducing print resolution was problematic, especially for continuous array printing, where there would be no 'runway' to let the accumulated ink come off the nozzle. The PVP ink would struggle to complete more than 2-3 layers in continuous array printing, since it would accumulate ink and either clog up and break the filament or fracture the printing nozzle or not fracture, but reduce the print resolution (Figure 7.9a-d).

The developed PVP/PVDF ink was able to successfully overcome the ink accumulation problem and print >15 layers without any ink accumulating on the nozzle (Figure 7.9e-h). This was due to the hydrophobicity of the PVDF in the blend, which reduced the overall ink affinity to the printing nozzle.

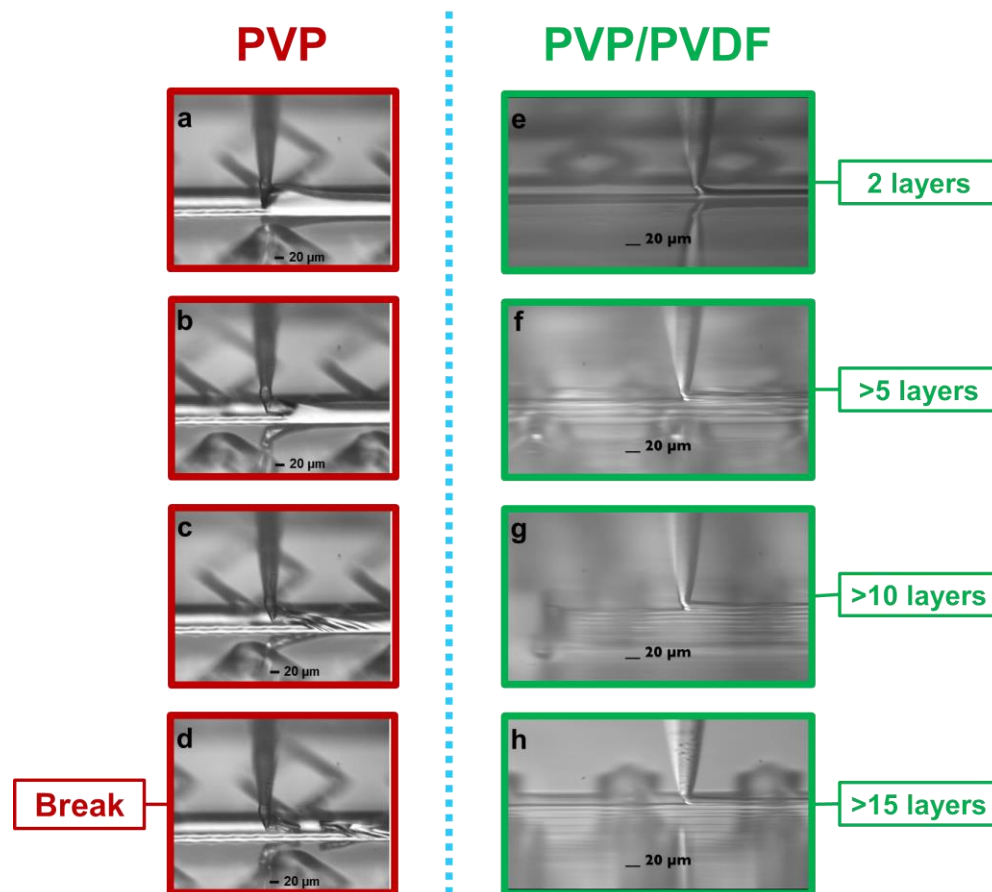


Figure 7.9: a-d.) Continuous array printing with PVP ink accumulating at the nozzle and clogging up the nozzle e-h.) Continuous array printing with PVP/PVDF ink successfully achieving >15 layers.

7.3 Conclusions

- Enhanced resolution of silver ink printing by functionalising a nozzle with RainX.
- Developed PVP/PVDF blended polymer ink was developed to reduce nozzle wetting during printing, especially during continuous array print runs.
- The developed PVP/PVDF ink was rheologically characterised and showed higher zero shear viscosity (112 Pa.s) than other PVP inks, as expected due to the increased molecular weight (Wang et al., 2014).
- Additionally, the G' and G'' of the PVP/PVDF ink were higher than the other PVP inks, as was also expected due to the increased molecular weight, which leads to more chain networks to be formed (Oser and Marvin, 1963).

- The developed PVP/PVDF ink was used with a 5 μm nozzle to print a pattern consisting of consecutive squares on glass slides. The same pattern was then printed on stainless steel with an interline spacing of 100 μm and again with an interline spacing of 200 μm . This pattern demonstrated that the ink was able to print fine corners without any delamination, which is a commonly encountered problem even in commercial 3D printers (Wang et al., 2007).
- The ink was then used to print diamond patterns a (D-pattern) on various substrates, including glass, polyimide, copper and stainless steel. The pattern showed the improved print quality, where the corners of the print out were visible and did not suffer from an ink accumulated nozzle, which would have made the corners of the printout less accurate/more rounded. The D-pattern was printed up to 100 layers high.
- A higher-resolution hexagonal structure was printed with a 1-3 μm nozzle 30 layers high without any ink accumulating at the nozzle. The wall size was maintained to be at 3 μm even after 30 layers, without suffering from any stringing. Additionally, it was observed that the printing nozzle benefitted from the increased flexibility it had for such a small tip aperture during printing such a polygon as structure.
- The ink was employed for printing a continuous array of 25 square pyramids and successfully printed >15 layers without any wetting of the nozzle. The printout was limited to 20 layers for this particular print, but in theory, since no ink was accumulating on the nozzle, the ink printing could have continued until the ink in the syringe barrel or the nitrogen supply would have depleted.

Chapter 8 – Summary of achievements & future work

This chapter contains the overall progress of the thesis and highlights the key achievements of this project. The chapter concludes with potential future work that can be developed from this thesis.

8.1 Summary of achievements

8.1.1 Decoupling printability from ink synthesis for rapid prototyping

- A range of safe, novel water based PVP inks have been developed to 3D direct-write printing water soluble micro moulds as an effective way to high-resolution ($<10\text{ }\mu\text{m}$) rapid prototyping, enabling simple 2.5D to more complex 3D micrometre structures to be fabricated with ease, outside the clean room.
- The novel inks have been characterised rheologically and the data can be used as a guide for the development of other potential direct-printable inks on the micrometre scale.
- The safe and simple PVP micro moulding approach enables otherwise difficult to structure materials like silicones (PDMS, Ecoflex) to be indirect AM fabricated, into self-standing structures, without the need for exhaustive formulation and optimisation of inks. The approach decouples ink formulation from precision prototyping.
- Our approach caters for a wide range of applications, especially in areas where micrometer scale structuring of ‘soft’ materials is needed.

8.1.2 Micro moulding approach for microstructured capacitive pressure sensors

- The developed water soluble micro moulding approach was successfully employed for rapid prototyping of PDMS pyramidal microstructured dielectric media for enhancing the sensitivity of capacitive pressure sensors. The structured dielectric media prior to this project – for almost a decade - have been fabricated in the clean room using photolithography or via toxic fume emitting, commercial 3D printers, that only work effectively in the millimetre range. Additionally, our approach does not suffer from the additional base layer – a mandatory side product of the fabrication process – that increases the dielectric layer thickness and consequently reduces the base capacitance.
- The approach of rapid prototyping via water soluble micromoulds was effectively used to fabricate minimally planar dielectric space occupying (<0.9 %) pyramidal structures (4 pyramids) that were relatively higher in height to facilitate a higher sensing range. Our approach is an effective way to miniaturise planar space, which is highly valued in the microelectronics industry (Liu et al., 1999).
- The developed 49 mm² sensor demonstrated response and relaxation times of ~20 ms and ~30 ms, respectively, which are amongst the highest reported. This was attributed to the high ratio of 'S' and high pyramid height of the developed sensors.
- A novel 6-sided pressure sensing ring prototype was implemented as a potential medical device, that could be worn by doctors and surgeons for measuring real-time pressure measurements. The pressure sensing ring was employed for the radial artery measurements of a 29 year old male

volunteer and demonstrated his heart rate of ~80 beats/min, which is within the healthy heart rate region of 60 to 100 beats/min for adults (MacGill, 2017).

8.1.3 Improving print resolution

- A novel PVP/PVDF blended ink was developed and rheologically characterised. The ink successfully reduced the wetting of the nozzle over the duration of the printouts, benefitting from the hydrophobicity of the PVDF.
- The developed polymer blend was able to successfully print high-resolution structures including 3 μm thick hexagonal walls maintained over 30 layers, 100 layers high D-patterns and >15 layers of continuous arrays, without any resolution reducing ink accumulation on the nozzles.

8.2 Future work

This section contains some potential work, that could build on the progress made in this thesis.

8.2.1 Moulding flexible interconnects and microfluidic channels

The developed water soluble micro moulding approach can be potentially used to fabricate flexible micro interconnects. A raster pattern (Figure 8.1a,b) was printed with a 25 μm nozzle and the PVP 30 wt% ink on a glass slide. Next, PDMS could be poured over this pattern and cured. After curing, the PDMS film could be peeled off with the indented raster pattern in it. This 'master' can be filled with otherwise difficult to print conductive inks so that flexible micro

interconnects can be fabricated without any oxidation, which is a big hurdle particularly for copper ink.

Separately, this 'master' could be attached to a flat layer of PDMS or glass via corona treatment and made into a microfluidic channel. The velocity profiles of microfluidic channels can be studied with respect to different printing nozzle apertures and different printing velocities.

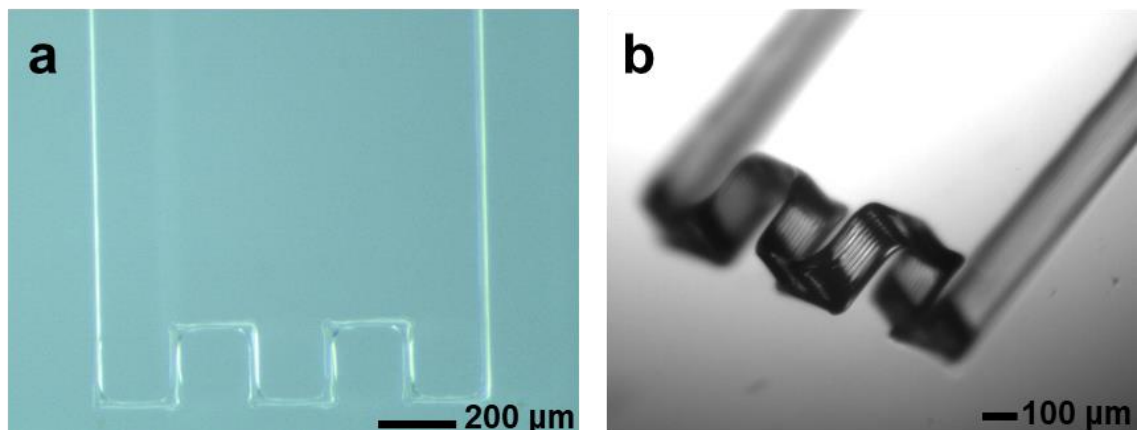


Figure 8.1: Printed raster pattern on glass a.) top view and b.) angled side view

8.2.2 Improving carbon black nanoparticle dispersion in elastomer matrix

Improving the dispersion of CB in an elastomeric matrix like PDMS, leads to better repeatability. One of the ways of improving carbon black nanoparticle dispersion is mixing for a longer period of time (Wolff and Wang, 1993). For our approach – probe sonicating CB into the curing agent – this could translate into probe sonication for a longer time, which would require a higher amount of curing agent due to an increase in evaporation (over a longer time).

Additionally, the container with the CB and curing agent should be kept at low temperature by using ice around the container so that the increased heat that is introduced with longer periods of probe sonication is counteracted. Similarly,

studying the effect of the initial particle size on the resulting dispersion quality is also important.

8.2.3 Effect of altering carbon black nanoparticle concentration

Enhancing the relative permittivity of polymers like PDMS with nanofillers such as carbon black nanoparticles has been investigated for a long time (Achour et al., 2008; Jang et al., 2016). However, an increase in nanoparticle concentration in a polymer matrix would also mean an increase in the Young's modulus of the polymer composite, which is generally undesirable for flexible pressure sensors.

Thus, another study that is yet to be done, includes varying the carbon nanoparticle concentration and finding a balance between the enhancement of the dielectric medium and the deformability of the dielectric medium.

8.2.4 Inter-pyramid material

The space between the fabricated pyramidal moulds is currently just air (inter-pyramid material), which has a dielectric constant of ~ 1 (Figure 8.2a). With photolithography it was the same material that the pyramids consisted of (mainly PDMS).

Our approach has opened the way to replacing the inter-pyramid material irrespective of the pyramid material. So it is possible for a high dielectric constant material to be filled in between the PDMS pyramids, resulting in a higher base capacitance (Figure 8.2b). However, it should be noted that the filling should only fill a small fraction of the height of the pyramids, which is yet

to be studied and determined. This is so that the filling will not interfere with the deformation of the sensor when a load is applied. The filling should only enhance the base capacitance without affecting the deformability of the dielectric layer.

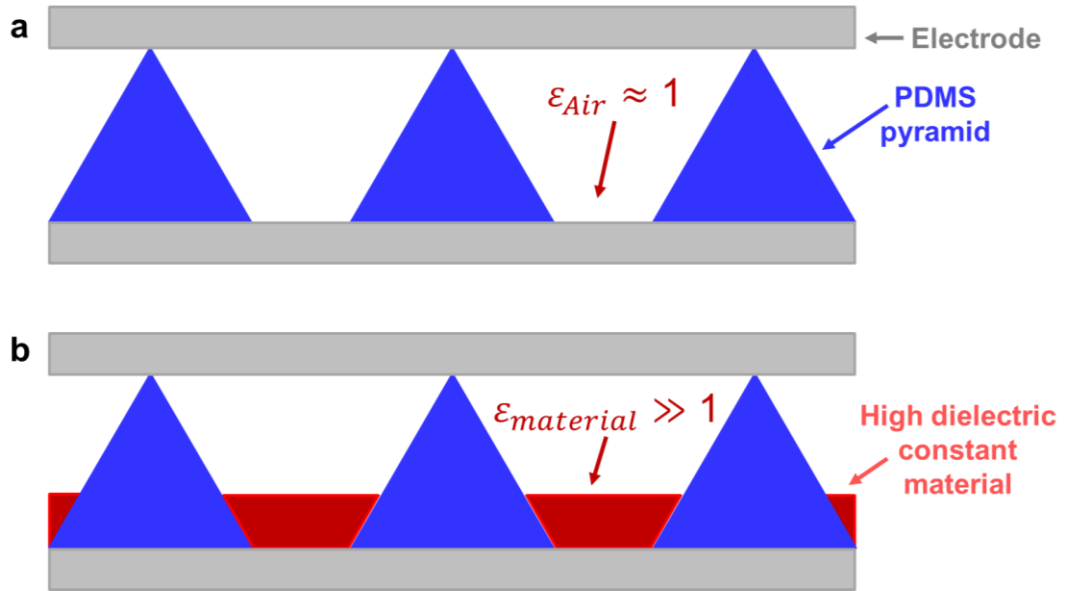


Figure 8.2: Varying inter-pyramid material concept schematics. a.) Schematic showing side view of PDMS pyramids with air as the inter-pyramid material and b.) schematic showing side view of PDMS pyramids with a high dielectric constant material as the inter-pyramid material

8.2.5 Going wireless with the pressure sensing ring

The developed pressure sensing ring in this project is currently using only one of the 6 sides and the sensor response is read via attached flexible wires to connect to the read out circuitry.

The next steps would be to utilise all sides of the ring by fabricating other miniaturised sensors, like temperature sensors, humidity sensors, etc. on it. Additionally, the wires would be removed and a small wireless readout circuitry would be integrated onto one side of the ring, so that the sensor data are transmitted wirelessly to a smartphone or a laptop (Figure 8.3).

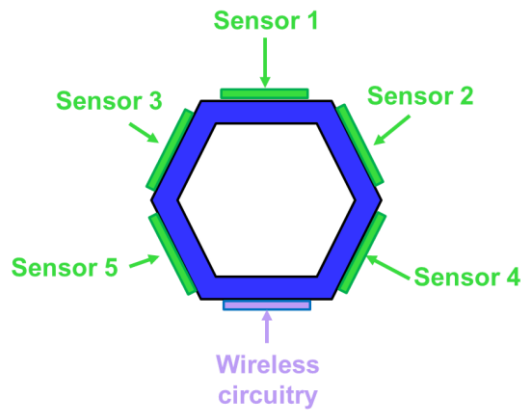


Figure 8.3: The next version of the pressure sensing ring consisting of 5 sensors and a wireless readout circuit

8.2.6 Simulating micropylramid deformation

Various groups have simulated capacitive pressure sensors and their responses with respect to different microstructures (Deng et al., 2016), different pyramid sizes and inter-pyramid spacing (Tee et al., 2014; Zhang et al., 2019).

However, with our developed novel approach of fabricating micropylramids via direct-write printing, we obtain novel microwave-texture surfaced micropylramids (Figure 8.4a, b). Simulating and studying the effect of these microwave-texture surfaced micropylramids on the overall deformation of the dielectric medium under an applied load – sensor performance – and comparing this to non-textured micropylramids is yet to be done.

This can further be correlated to the nozzle size used to print the initial micro moulds, so that the effective Young's modulus of the dielectric medium can be tuned from the size of the nozzle aperture.

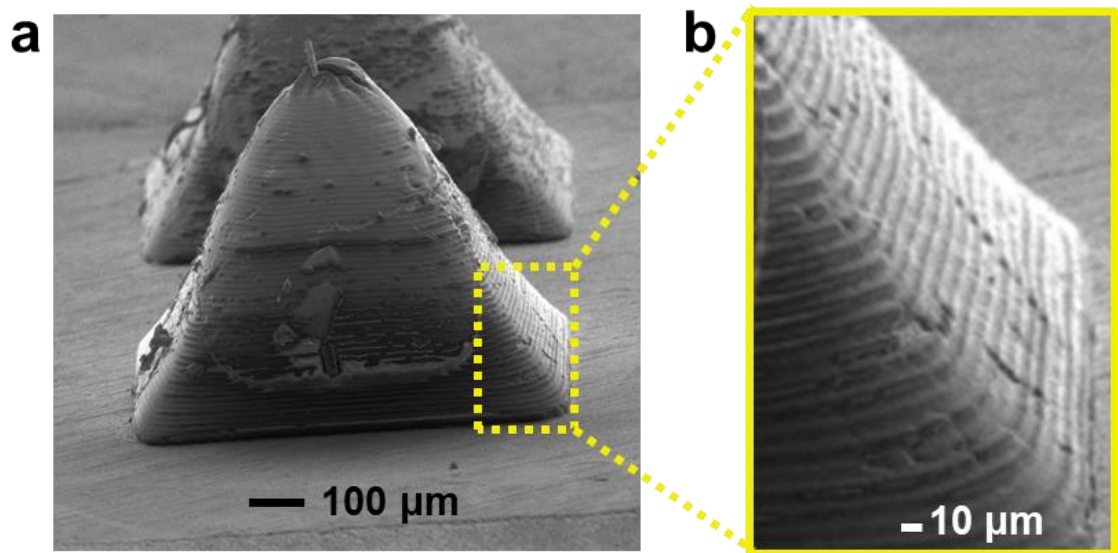


Figure 8.4: Microwave-surface textured micropyramids a.) SEM image of micropyramid b.) Scaled SEM image showing the microwave-textured surface

8.2.7 Filling micro moulds with different elastomers

Another study that is yet to be done consists of printing multiple identical micropyramid arrays – each array forming the dielectric medium of a capacitive pressure sensor – and filling them with varying elastomers (different Young's modulus). The Young's modulus of PDMS can be varied by changing the amount of curing agent during the mixing stage. The various sensors – each only differing in terms of their Young's modulus of the dielectric medium – can be characterised to relate the Young's modulus of the dielectric medium to the sensor response.

8.2.8 Varying sidewall angle of the pyramids

The fabrication of pyramidal microstructured dielectric media has been predominantly achieved with photolithographically etching silicone wafers (Clementine M Boutry et al., 2015; Ruth et al., 2019; Tee et al., 2014; Zhang et al., 2017). This approach limits the side wall angle of the pyramids to be 54.7°.

However, with the help of simulation, reducing the sidewall angle has shown to reduce the effective Young's modulus of the dielectric medium (Figure 8.5a, b) which in turn enhances the sensitivity of the capacitive pressure sensors (Tee et al., 2014). Using the direct-write approach, the side wall angle can be varied and in particular reduced to below 54.7°.

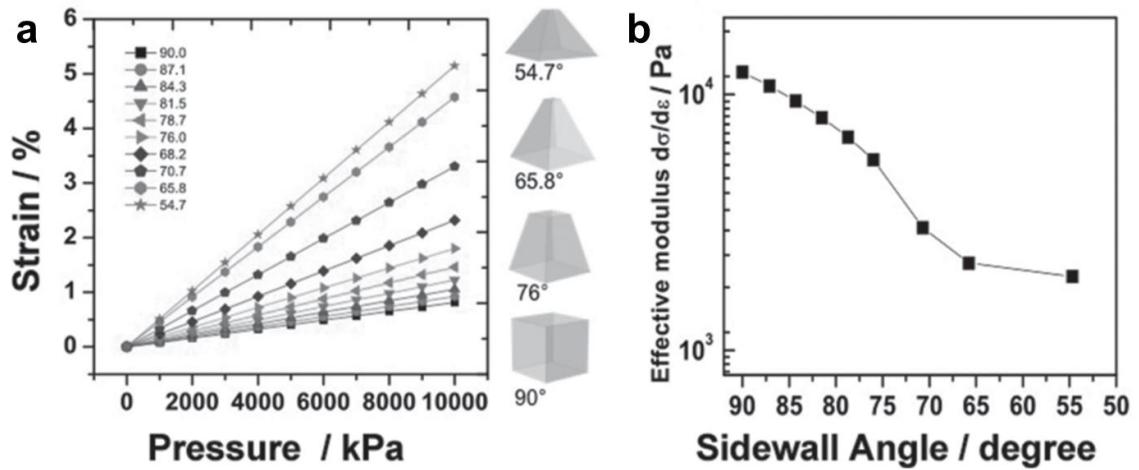


Figure 8.5: Simulation data showing a.) predicted stress-strain relationship for different sidewall angled micropyramids and b.) predicted effective modulus of the micropyramids as a function of the sidewall angle (Tee et al., 2014)

8.2.9 Imaging the micropyramids during deformation

The direct-write printed pyramidally microstructured dielectric media are to be imaged with a microscope from the sides of the sensors while a force is applied onto the sensors. This is so that the applied force (on the capacitive pressure sensors) and the amount of deformation (of the dielectric media) can be correlated.

8.2.10 Dynamic studies of the developed capacitive pressure sensors

The developed capacitive pressure sensors are to be tested dynamically to resemble real-time applications. This would be achieved by using a force gauge and stepper motor to apply a known force at fixed intervals onto the sensors.

Appendix

A.1 Rheometer setup and procedures

The manometer behind the instrument should be checked to ensure that the right air pressure of 30 psi is supplied to the instrument. The rheometer (Discovery Hybrid Rheometer, DHR-3, TA instruments) is setup and the Peltier plate is mounted onto the base of the instrument (Figure A.1a). The TRIOS software (TA Instruments) is initialised on the PC.

A 40 mm flat stainless steel sandblasted geometry (Stainless Steel, sandblasted, 40 mm Plate, model: 519400.905, TA instruments) is mounted onto the instrument (Figure A.1b). The sandblasted parallel plate geometry was used to avoid any apparent wall slip (Mendes et al., 2014).

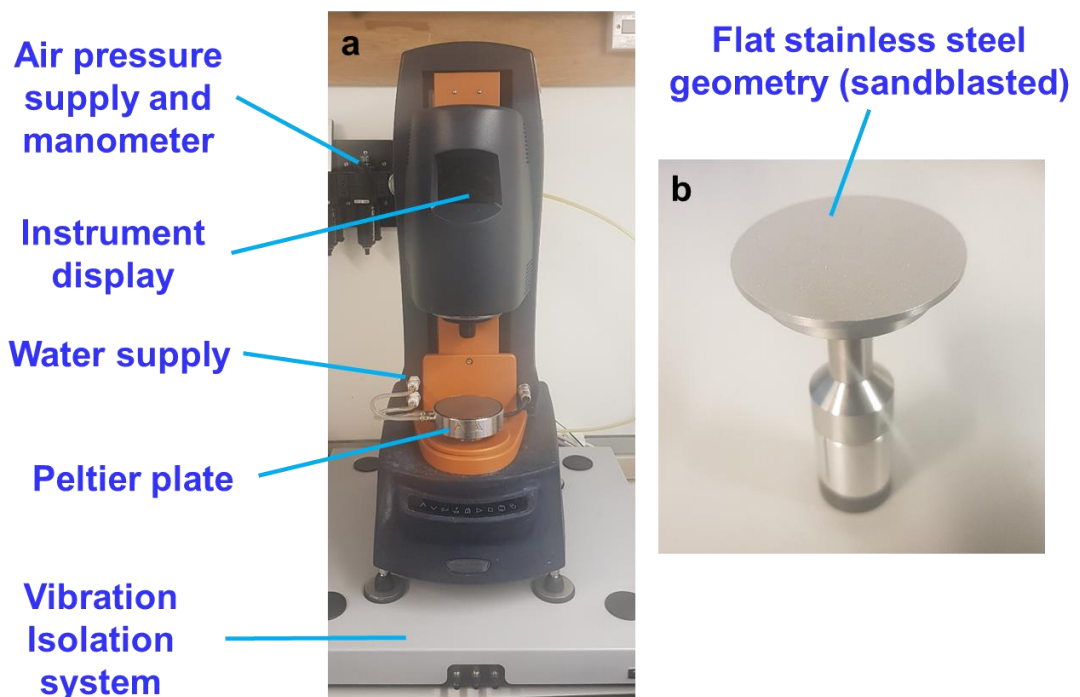


Figure A.1: Overview of rheometer a.) DHR-3 rheometer from TA instruments with mounted Peltier plate b.) Sandblasted flat stainless steel geometry from TA instruments

The TRIOS software detects the geometry automatically. The software is used to 'tare/zero' the gap between the geometry and the Peltier plate. The sample/loading gap is to be set to 500 μm .

A syringe with the ink to be characterised (PVP, PVDF/PVP, etc.) is loaded to the volume calculated by the TRIOS software (calculations are based on loading gap). It should be noted that during the filling process, potential air bubbles in the ink of the syringe are avoided by filling the syringe slowly. The ink from the filled syringe is then slowly emptied onto the centre of the Peltier plate. Again, this is to be done without trapping any air bubbles in the ink on the Peltier plate.

Then the inks were subjected to a flow ramp (steady state response) and oscillatory amplitude sweep following previously reported protocols (M'Barki et al., 2017; Valentine et al., 2017).

The flow ramp was performed over a torque range of 1 to 10,000 $\mu\text{N.m}$ for a duration of 300 s at a sampling interval of 1 s/pt and at RT. Similarly, the amplitude sweep was performed at a frequency of 1 Hz over a torque range of 0.1 to 10,000 $\mu\text{N.m}$ at 5 points per decade.

A.2 P-1000 Sutter Instrument parameter programs

a	1 - 3 μm nozzle					
	Line	Heat	Pull	Vel	Delay	Pressure
	1x1	521	0	21	1	600
	2x1	521	0	21	1	
	3x1	521	0	21	1	
	4x1	521	0	21	1	
		Ramp		521		
		Heating filament		FB225B		
		Capillary		1.5x0.86mmx7.5cm		

b	10 μm nozzle					
	Line	Heat	Pull	Vel	Delay	Pressure
	1x1	496	0	21	1	600
	2x1	496	0	21	1	
	3x1	496	0	17	1	
	4x1	496	0	15	1	
		Ramp		521		
		Heating filament		FB225B		
		Capillary		1.5x0.86mmx7.5cm		

c	20 μm nozzle					
	Line	Heat	Pull	Vel	Delay	Pressure
	1x1	496	0	21	1	600
	2x1	496	0	21	1	
	3x1	496	0	14	1	
	4x1	-	-	-	-	
		Ramp		521		
		Heating filament		FB225B		
		Capillary		1.5x0.86mmx7.5cm		

d	30 μm nozzle					
	Line	Heat	Pull	Vel	Delay	Pressure
	1x1	496	0	21	1	600
	2x1	496	0	21	1	
	3x1	496	0	13	1	
	4x1	496	0	12	1	
		Ramp		521		
		Heating filament		FB225B		
		Capillary		1.5x0.86mmx7.5cm		

Figure A.2: P-1000 Sutter Instrument parameter programs for a.) 1-3 μm nozzle, b.) 10 μm nozzle, c.) 20 μm nozzle and d.) 30 μm nozzle

A.3 PCB design software DipTrace

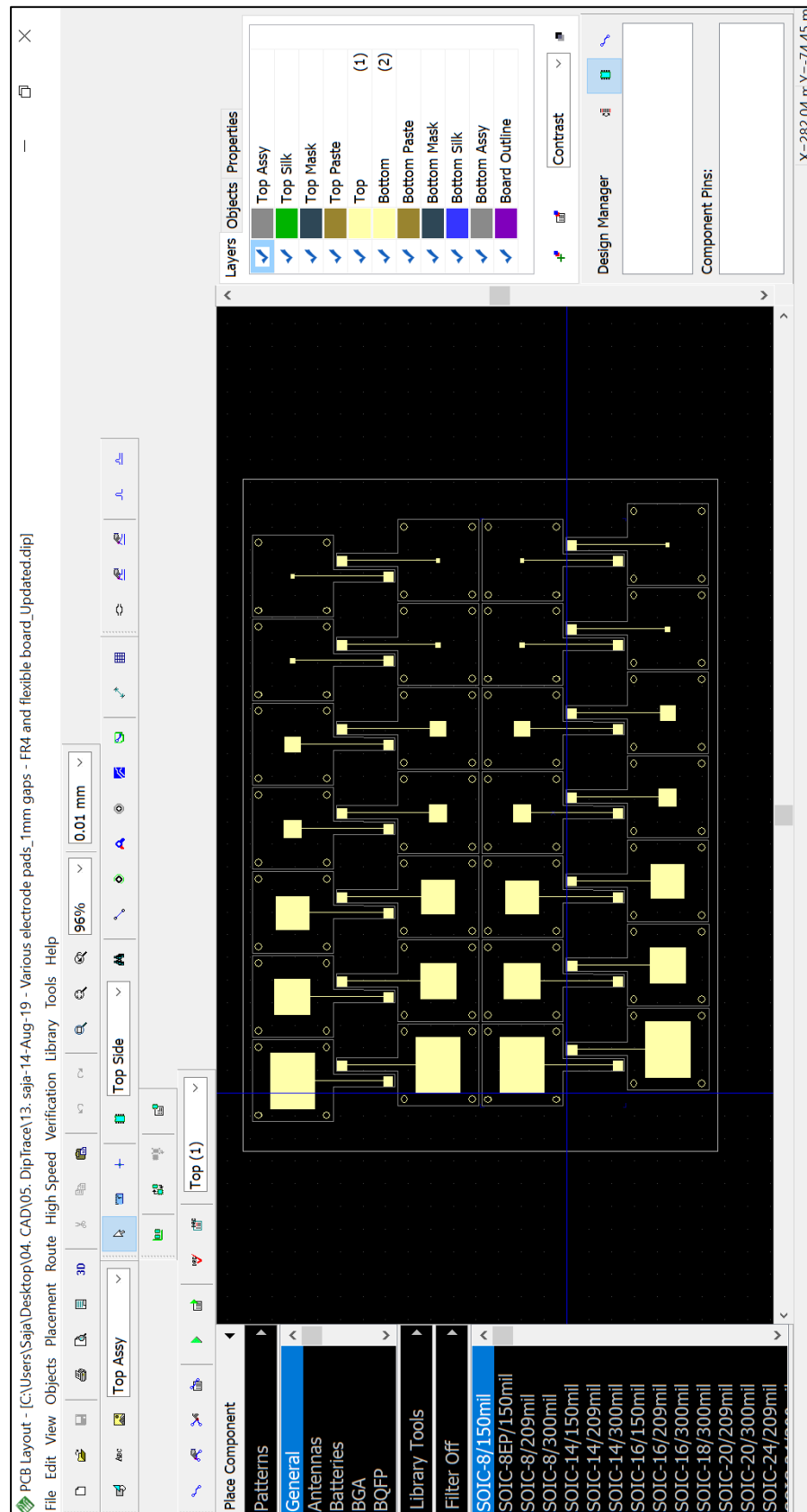


Figure A.3: PCB design software (DipTrace) screenshot showing various designed PCBs

A.4 Calibration steps of LCR-821

<p>LCR-800 Series User Manual</p> <hr/> <h3>4. OPERATION</h3> <h4>4-1. Connects to DUT</h4> <p>The LCR Meters utilize the structure of four wires measurement which allows accurate, easy, and stable measurements and avoids mutual inductance and interference from measurement signals, noise and other factors inherent with other types of connections. For the accuracy of measurement, GOODWILL produces the cable set and test fixture (option) for connection directly to the front panel BNC connectors.</p> <h4>4-2. Start-Up</h4> <p>Connects the power cord of the LCR Meters to the mains socket-outlet. Presses the POWER button of front panel to apply the AC power to the LCR Meters.</p> <h4>4-3. Zeroing</h4> <p>In order to eliminate strayed capacitance and impedance of test cable during the measurement, the LCR Meters should be zeroed to correct for test cable and/or test fixture errors before taking measurements. The corrections are calculated and stored in memory of the LCR Meters during the zeroing process. Open and short circuit zeroing should be done for test cable and/or test fixture. For the best accuracy, the test cable and/or test fixture should be zeroed once per day at least and each time test cable or test fixture is changed in general.</p> <p>The zeroing process of open and short circuits are following:</p> <h5>Open Circuit</h5> <ul style="list-style-type: none"> • The test cable or test fixture should be open with no component connected. • Press MENU key. • Press F1 key to select "OFFSET" menu. • Press F1 key to select open circuit zeroing (the "CAP OFFSET" is indicated on the adjacent LCD monitor.) 	<p>LCR-800 Series User Manual</p> <hr/> <ul style="list-style-type: none"> • After the BAR at the bottom of LCD monitor is filled to the full, the zeroing process is done. • If the zeroing process is successful, a message of "OK" will appear on the LCD monitor. If failed, a message of "FAIL" will appear on the LCD monitor. <h5>Short Circuit</h5> <ul style="list-style-type: none"> • The test cable should be connected or test fixture shorted (using a clean copper wire, as short as possible). • Press MENU key. • Press F1 key to select "OFFSET" menu. • Press F2 key to select short circuit zeroing (the "R/L OFFSET" is indicated on the adjacent LCD monitor.) • After the BAR at the bottom of LCD monitor is filled fully, the zeroing process is done. • If the zeroing process is successful, a message of "OK" will appear on the LCD monitor. If failed, a message of "FAIL" will appear on the LCD monitor. <h5>Test Condition:</h5> <p>Test voltage=According to the actual test voltage. Test speed = According to the actual test speed. R.H = OFF C.V = According to the actual test status.</p> <p>For the summary, the zeroing menu can be chosen through menu selection as shown in Figure 4-1 above.</p> <p>NOTE: The "Open Circuit" and "Short Circuit" have to pass the test, otherwise, the accuracy of the LCR Meters will become worse.</p>
<p>LCR-800 Series User Manual</p> <hr/>	<p>LCR-800 Series User Manual</p> <hr/>

Figure A.4: Calibration steps of LCR-821 in supplier manual ("LCR-800 Series User Manual," 1998)

A.5 Calibration of Keysight Semiconductor Device Analyser B1500a

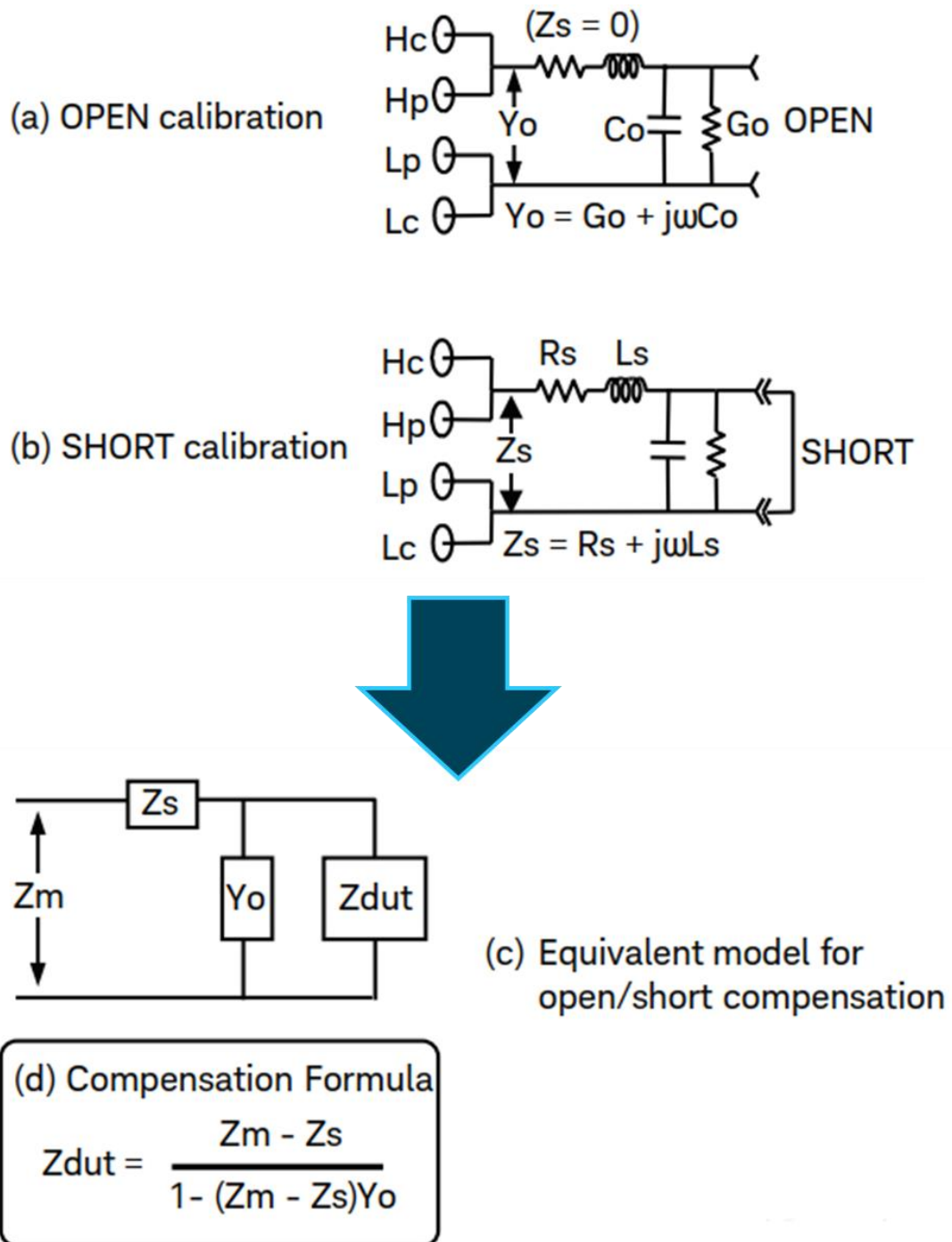


Figure A.5: Overview of Open/Short compensation of semiconductor device analyser B1500a (Keysight, 2019)

A.6 Hexagonal ring design

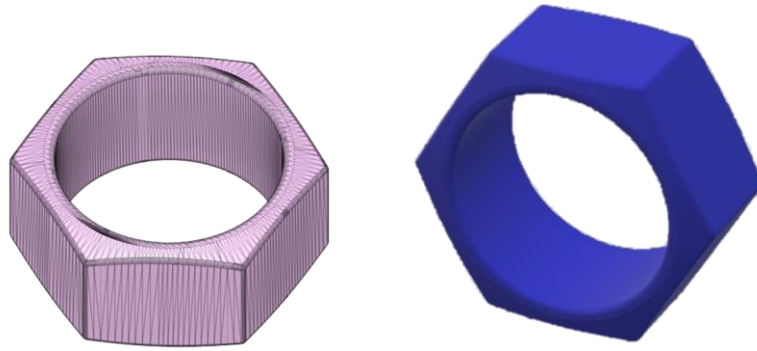


Figure A.6: CAD drawing of hexagonal ring for the pressure sensing ring prototype

References

- Abraham, M.H., Helvajian, H., 2004. Laser direct write for release of SiO₂ MEMS and nano-scale devices 543–550. <https://doi.org/10.1117/12.596553>
- Achour, M.E., Mdarhri, A., Carmona, F., Lahjomri, F., Oueriagli, A., 2008. Dielectric properties of carbon black-epoxy resin composites studied with impedance spectroscopy. *Spectrosc. Lett.* 41, 81–86. <https://doi.org/10.1080/00387010801943848>
- Adjustable Micropipette 1 – 5 ml [WWW Document], 2018. URL <https://www.vapecrew.co.nz/wp-content/uploads/2019/02/DIY-E-Liquid-E-Juice-and-Nicotine-Adjustable-Micropipette-1—5ml.png> (accessed 9.20.10).
- Ahn, B.Y., Duoss, E.B., Motala, M.J., Guo, X., Park, S. Il, Xiong, Y., Yoon, J., Nuzzo, R.G., Rogers, J.A., Lewis, J.A., 2009. Omnidirectional printing of flexible, stretchable, and spanning silver microelectrodes. *Science* (80-.). 323, 1590–1593. <https://doi.org/10.1126/science.1168375>
- Ahn, B.Y., Lewis, J.A., 2014. Amphiphilic silver particles for conductive inks with controlled wetting behavior. *Mater. Chem. Phys.* 148, 686–691. <https://doi.org/10.1016/j.matchemphys.2014.08.035>
- Akiyama, M., Morofuji, Y., Kamohara, T., Nishikubo, K., Tsubai, M., Fukuda, O., Ueno, N., 2006. Flexible piezoelectric pressure sensors using oriented aluminum nitride thin films prepared on polyethylene terephthalate films. *J. Appl. Phys.* 100. <https://doi.org/10.1063/1.2401312>
- Andelin, J., Curlin, J.W., 1991. Miniaturization Technologies. Congr. United States, Off. Technol. Assess. [https://doi.org/10.1016/0141-6359\(92\)90042-U](https://doi.org/10.1016/0141-6359(92)90042-U)
- Antiretroviral, T., Cohort, T., 2008. Life expectancy of individuals on combination antiretroviral therapy in high-income countries: a collaborative analysis of 14 cohort studies. *Lancet* 372, 293–9. [https://doi.org/10.1016/S0140-6736\(08\)61113-7](https://doi.org/10.1016/S0140-6736(08)61113-7)
- Ashton, K., 2010. That “Internet of Things” Thing. RFID J.
- Atalay, O., Atalay, A., Gafford, J., Walsh, C., 2018. A Highly Sensitive Capacitive-Based Soft Pressure Sensor Based on a Conductive Fabric and a Microporous Dielectric Layer. *Adv. Mater. Technol.* 3. <https://doi.org/10.1002/admt.201700237>
- Boutry, Clementine M., Nguyen, A., Lawal, Q.O., Chortos, A., Rondeau-Gagné, S., Bao, Z., 2015. A Sensitive and Biodegradable Pressure Sensor Array for Cardiovascular Monitoring - Supporting information. *Adv. Mater.* 27, 6954–6961. <https://doi.org/10.1002/adma.201502535>
- Boutry, Clementine M., Nguyen, A., Lawal, Q.O., Chortos, A., Rondeau-Gagné, S., Bao, Z., 2015. A Sensitive and Biodegradable Pressure Sensor Array for Cardiovascular Monitoring. *Adv. Mater.* 6954–6961. <https://doi.org/10.1002/adma.201502535>
- Buechley, L., Eisenberg, M., 2009. Fabric PCBs, electronic sequins, and socket buttons: Techniques for e-textile craft. *Pers. Ubiquitous Comput.* 13, 133–150. <https://doi.org/10.1007/s00779-007-0181-0>
- Bunde, R.L., Jarvi, E.J., Rosentreter, J.J., 1998. Piezoelectric quartz crystal biosensors. *Talanta* 46, 1223–1236. [https://doi.org/10.1016/S0039-9140\(97\)00392-5](https://doi.org/10.1016/S0039-9140(97)00392-5)
- Chen, J., Wang, X., Yu, X., Yao, L., Duan, Z., Fan, Y., Jiang, Y., Zhou, Y., Pan, Z., 2018. High dielectric constant and low dielectric loss poly(vinylidene fluoride) nanocomposites *via* a small loading of two-dimensional Bi₂Te₃@Al₂O₃ hexagonal nanoplates. *J. Mater. Chem. C* 19–21. <https://doi.org/10.1039/C7TC04758D>
- Chen, L.Y., Tee, B.C.-K., Chortos, A.L., Schwartz, G., Tse, V., J Lipomi, D., Wong, H.-S.P., McConnell, M. V, Bao, Z., 2014. Continuous wireless pressure

- monitoring and mapping with ultra-small passive sensors for health monitoring and critical care. *Nat. Commun.* 5, 5028. <https://doi.org/10.1038/ncomms6028>
- Chen, S., Zhuo, B., Guo, X., 2016. Large Area One-Step Facile Processing of Microstructured Elastomeric Dielectric Film for High Sensitivity and Durable Sensing over Wide Pressure Range. *ACS Appl. Mater. Interfaces* 8, 20364–20370. <https://doi.org/10.1021/acsami.6b05177>
- Cho, S.H., Lee, S.W., Yu, S., Kim, H., Chang, S., Kang, D., Hwang, I., Kang, H.S., Jeong, B., Kim, E.H., Cho, S.M., Kim, K.L., Lee, H., Shim, W., Park, C., 2017. Micropatterned Pyramidal Ionic Gels for Sensing Broad-Range Pressures with High Sensitivity. *ACS Appl. Mater. Interfaces* 9, 10128–10135. <https://doi.org/10.1021/acsami.7b00398>
- Chong, C.Y., Kumar, S.P., 2003. Sensor networks: Evolution, opportunities, and challenges. *Proc. IEEE* 91, 1247–1256. <https://doi.org/10.1109/JPROC.2003.814918>
- Chortos, A., Liu, J., Bao, Z., 2016a. Pursuing prosthetic electronic skin. *Nat. Mater.* <https://doi.org/10.1038/nmat4671>
- Chortos, A., Liu, J., Bao, Z., 2016b. Pursuing prosthetic electronic skin. *Nat. Mater.* 1–14. <https://doi.org/10.1038/nmat4671>
- Clarfield, A.M., 2017. Healthy Life Expectancy Is Expanding. *J. Am. Geriatr. Soc.* 66, 200–201. <https://doi.org/10.1111/jgs.15165>
- Cui, J., Zhang, B., Duan, J., Guo, H., Tang, J., 2017. A micro-pressure sensing method based on the micropatterned electrodes filled with the microspheres. *Materials (Basel)*. 10. <https://doi.org/10.3390/ma10121439>
- Dabbling, J.G., Filatov, A., Wheeler, J.W., 2012. Static and Cyclic Performance Evaluation of Sensors for Human Interface Pressure Measurement, in: 34th Annual International Conference of the IEEE EMBS.
- Dagdeviren, C., Su, Y., Joe, P., Yona, R., Liu, Y., Kim, Y.S., Huang, Yongan, Damadoran, A.R., Xia, J., Martin, L.W., Huang, Yonggang, Rogers, J.A., 2014. Conformable amplified lead zirconate titanate sensors with enhanced piezoelectric response for cutaneous pressure monitoring. *Nat. Commun.* 5. <https://doi.org/10.1038/ncomms5496>
- Dang, Z.M., Yuan, J.K., Zha, J.W., Zhou, T., Li, S.T., Hu, G.H., 2012. Fundamentals, processes and applications of high-permittivity polymer-matrix composites. *Prog. Mater. Sci.* 57, 660–723. <https://doi.org/10.1016/j.pmatsci.2011.08.001>
- Daoud, W.A., Xin, J.H., Szeto, Y.S., 2005. Polyethylenedioxythiophene coatings for humidity, temperature and strain sensing polyamide fibers. *Sensors Actuators, B Chem.* 109, 329–333. <https://doi.org/10.1016/j.snb.2004.12.067>
- Definition of Sensor by Lexico [WWW Document], 2019. . Lexico Dictionaries | English. URL <https://www.lexico.com/en/definition/sensor> (accessed 1.1.18).
- Deng, W., Huang, X., Chu, W., Chen, Y., Mao, L., Tang, Q., Yang, W., 2016. Microstructure-Based Interfacial Tuning Mechanism of Capacitive Pressure Sensors for Electronic Skin. *J. Sensors* 2016. <https://doi.org/10.1155/2016/2428305>
- Dias, D., Cunha, J.P.S., 2018. Wearable health devices—vital sign monitoring, systems and technologies. *Sensors (Switzerland)* 18. <https://doi.org/10.3390/s18082414>
- Dow corning, 2014. Sylgard 184 Silicone Elastomer.
- Eijkel, J.C.T., van den Berg, A., 2005. Nanofluidics: What is it and what can we expect from it? *Microfluid. Nanofluidics* 1, 249–267. <https://doi.org/10.1007/s10404-004-0012-9>
- Engler, O., Schäfer, C., Brinkman, H.J., Brecht, J., Beiter, P., Nijhof, K., 2016. Flexible rolling of aluminium alloy sheet - Process optimization and control of materials properties. *J. Mater. Process. Technol.* 229, 139–148.

<https://doi.org/10.1016/j.jmatprotec.2015.09.010>

- Fang, Feihuang and Aabith, S., Homer-Vanniasinkam, S., Tiwari, M.K., 2017. High-resolution 3D printing for healthcare underpinned by small-scale fluidics, 3D Printing in Medicine. <https://doi.org/10.1016/B978-0-08-100717-4.00023-5>
- Fiorito, S., Serafino, A., Andreola, F., Togna, A., Togna, G., 2006. Toxicity and biocompatibility of carbon nanoparticles. *J. Nanosci. Nanotechnol.* <https://doi.org/10.1166/jnn.2006.125>
- García-Tuñón, E., Feilden, E., Zheng, H., D'Elia, E., Leong, A., Saiz, E., 2017. Graphene Oxide: An All-in-One Processing Additive for 3D Printing. *ACS Appl. Mater. Interfaces.* <https://doi.org/10.1021/acsami.7b07717>
- Gibson, I., Srinath, A., 2015. Simplifying Medical Additive Manufacturing: Making the Surgeon the Designer. *Procedia Technol.* 20, 237–242. <https://doi.org/10.1016/j.protcy.2015.07.038>
- Gross, R., 1992. Life expectancy. *Med. Decis. Mak.* 12, 307–311. <https://doi.org/10.4054/DemRes.2011.24.11>
- Gubbi, J., Buyya, R., Marusic, S., Palaniswami, M., 2013. Internet of Things (IoT): A vision, architectural elements, and future directions. *Futur. Gener. Comput. Syst.* 29, 1645–1660. <https://doi.org/10.1016/j.future.2013.01.010>
- Guo, Yuxiong, Xu, J., Yan, C., Chen, Y., Zhang, X., Jia, X., Liu, Y., Wang, X., Zhou, F., 2019a. Direct Ink Writing of High Performance Architected Polyimides with Low Dimensional Shrinkage - SI. *Adv. Eng. Mater.* <https://doi.org/10.1002/adem.201801314>
- Guo, Yuxiong, Xu, J., Yan, C., Chen, Y., Zhang, X., Jia, X., Liu, Y., Wang, X., Zhou, F., 2019b. Direct Ink Writing of High Performance Architected Polyimides with Low Dimensional Shrinkage. *Adv. Eng. Mater.* <https://doi.org/10.1002/adem.201801314>
- Guo, Ying, Zhong, M., Fang, Z., Wan, P., Yu, G., 2019. A Wearable Transient Pressure Sensor Made with MXene Nanosheets for Sensitive Broad-Range Human-Machine Interfacing. *Nano Lett.* 19, 1143–1150. <https://doi.org/10.1021/acs.nanolett.8b04514>
- Hector, L.G., Schultz, H.L., 1936. The dielectric constant of air at radiofrequencies. *J. Appl. Phys.* 7, 133–136. <https://doi.org/10.1063/1.1745374>
- Hendee, W.R., 1989. Cross Sectional Medical Imaging: A History.
- Hlinka, J., 2019. Doubling up piezoelectric performance. *Science* (80-.). 364, 228–229. <https://doi.org/10.1126/science.aax0693>
- Huang, W.D., Cao, H., Deb, S., Chiao, M., Chiao, J.C., 2011. A flexible pH sensor based on the iridium oxide sensing film. *Sensors Actuators, A Phys.* 169, 1–11. <https://doi.org/10.1016/j.sna.2011.05.016>
- Huang, X., Yeo, W.H., Liu, Y., Rogers, J.A., 2012. Epidermal differential impedance sensor for conformal skin hydration monitoring. *Biointerphases* 7, 1–9. <https://doi.org/10.1007/s13758-012-0052-8>
- Huang, Y., Fan, X., Chen, S.C., Zhao, N., 2019. Emerging Technologies of Flexible Pressure Sensors: Materials, Modeling, Devices, and Manufacturing. *Adv. Funct. Mater.* 29. <https://doi.org/10.1002/adfm.201808509>
- Hussain, M., Choa, Y.-H., Niihara, K., 2001. Conductive rubber materials for pressure sensors. *J. Mater. Sci. Lett.* 20, 525–527.
- Jang, H., Yoon, H., Ko, Y., Choi, J., Lee, S.-S., Jeon, I., Kim, J.-H., Kim, H., 2016. Enhanced performance in capacitive force sensors using carbon nanotube/polydimethylsiloxane nanocomposites with high dielectric properties. *Nanoscale* 8, 5667–5675. <https://doi.org/10.1039/C5NR07958F>
- Janna, W.S., 2010. Introduction to Fluid Mechanics, 4th edition, 4th ed. CRC Press.
- Jeong, J.W., Kim, M.K., Cheng, H., Yeo, W.H., Huang, X., Liu, Y., Zhang, Y., Huang,

- Y., Rogers, J.A., 2014. Capacitive epidermal electronics for electrically safe, long-term electrophysiological measurements. *Adv. Healthc. Mater.* 3, 642–648. <https://doi.org/10.1002/adhm.201300334>
- Jina, A., Tierney, M.J., Tamada, J.A., McGill, S., Desai, S., Chua, B., Chang, A., Christiansen, M., 2014. Design, development, and evaluation of a novel microneedle array-based continuous glucose monitor. *J. Diabetes Sci. Technol.* 8, 483–487. <https://doi.org/10.1177/1932296814526191>
- Jog, N.K., 2013. *Electronics in Medicine and Biomedical Instrumentation*.
- Johnston, I.D., McCluskey, D.K., Tan, C.K.L., Tracey, M.C., 2014. Mechanical characterization of bulk Sylgard 184 for microfluidics and microengineering. *J. Micromechanics Microengineering* 24, 035017. <https://doi.org/10.1088/0960-1317/24/3/035017>
- Kang, M.K., Park, J.H., Lee, K. Il, Cho, J.W., Bae, J., Ju, B.K., Lee, C.S., 2015. Fully flexible and transparent piezoelectric touch sensors based on ZnO nanowires and BaTiO₃-added SiO₂ capping layers. *Phys. Status Solidi Appl. Mater. Sci.* 212, 2005–2011. <https://doi.org/10.1002/pssa.201431829>
- Kehoe, B., Kahn, G., Mahler, J., Kim, J., Lee, Alex, Lee, Anna, Nakagawa, K., Patil, S., Boyd, W.D., Abbeel, P., Goldberg, K., 2014. Autonomous multilateral debridement with the Raven surgical robot, in: *Proceedings - IEEE International Conference on Robotics and Automation*. pp. 1432–1439. <https://doi.org/10.1109/ICRA.2014.6907040>
- Keum, H., McCormick, M., Liu, P., Zhang, Y., Omenetto, F.G., 2011. RESEARCH ARTICLES Epidermal Electronics. *Science* (80-.). 333, 838–844. <https://doi.org/10.1126/science.1206157>
- Keysight, 2019. Application note - Capacitance Measurement Basics for Device/Material Characterization Using Keysight B1500A Semiconductor Device Analyzer.
- Khan, Y., Ostfeld, A.E., Lochner, C.M., Pierre, A., Arias, A.C., 2016. Monitoring of Vital Signs with Flexible and Wearable Medical Devices. *Adv. Mater.* <https://doi.org/10.1002/adma.201504366>
- Kim, H., Ahn, J.H., 2017. Graphene for flexible and wearable device applications. *Carbon N. Y.* 120, 244–257. <https://doi.org/10.1016/j.carbon.2017.05.041>
- Kim, J., Campbell, A.S., de Ávila, B.E.F., Wang, J., 2019. Wearable biosensors for healthcare monitoring. *Nat. Biotechnol.* 37, 389–406. <https://doi.org/10.1038/s41587-019-0045-y>
- Klein, F., Richter, B., Striebel, T., Franz, C.M., Freymann, G. Von, Wegener, M., Bastmeyer, M., 2011. Two-component polymer scaffolds for controlled three-dimensional cell culture. *Adv. Mater.* 23, 1341–1345. <https://doi.org/10.1002/adma.201004060>
- Knite, M., Teteris, V., Kiploka, A., Kaupuzs, J., 2004. Polyisoprene-carbon black nanocomposites as tensile strain and pressure sensor materials. *Sensors Actuators, A Phys.* 110, 142–149. <https://doi.org/10.1016/j.sna.2003.08.006>
- Kolle, M., Lethbridge, A., Kreysing, M., Baumberg, J.J., Aizenberg, J., Vukusic, P., 2013. Bio-inspired band-gap tunable elastic optical multilayer fibers. *Adv. Mater.* 25, 2239–2245. <https://doi.org/10.1002/adma.201203529>
- Kudo, H., Sawada, T., Kazawa, E., Yoshida, H., Iwasaki, Y., Mitsubayashi, K., 2006. A flexible and wearable glucose sensor based on functional polymers with Soft-MEMS techniques. *Biosens. Bioelectron.* 22, 558–562. <https://doi.org/10.1016/j.bios.2006.05.006>
- Kulkarni, G.U., Kiruthika, S., Gupta, R., Rao, K.D.M., 2015. Towards low cost materials and methods for transparent electrodes. *Curr. Opin. Chem. Eng.* <https://doi.org/10.1016/j.coche.2015.03.001>

- Kumbar, S., Laurencin, C., Deng, M., 2014. Natural and Synthetic Biomedical Polymers: .
- Kuroiwa, T., Miyagishi, T., Ito, A., 1995. *Sensor* 25, 692–695.
- Kwon, D., Lee, T.-I., Shim, J., Ryu, S., Kim, M.S., Kim, S., Kim, T.-S., Park, I., 2016a. Highly Sensitive, Flexible, and Wearable Pressure Sensor Based on a Giant Piezocapacitive Effect of Three-Dimensional Microporous Elastomeric Dielectric Layer. *ACS Appl. Mater. Interfaces* 8, 16922–16931. <https://doi.org/10.1021/acsami.6b04225>
- Kwon, D., Lee, T.I., Shim, J., Ryu, S., Kim, M.S., Kim, S., Kim, T.S., Park, I., 2016b. Highly Sensitive, Flexible, and Wearable Pressure Sensor Based on a Giant Piezocapacitive Effect of Three-Dimensional Microporous Elastomeric Dielectric Layer - SUPPLEMENTARY. *ACS Appl. Mater. Interfaces* 8, 16922–16931. <https://doi.org/10.1021/acsami.6b04225>
- Lam, E., Ngo, T., 2007. Manufacturing a PDMS microfluidic device via a Silicon Wafer Master. *Harvard-MIT Div. Heal. Sci. Technol. HST. J* 410.
- Lang, U., Rust, P., Dual, J., 2008. Towards fully polymeric MEMS: Fabrication and testing of PEDOT/PSS strain gauges. *Microelectron. Eng.* 85, 1050–1053. <https://doi.org/10.1016/j.mee.2008.01.051>
- LCR-800 Series User Manual, 1998.
- Lee, H.L.M., 2019. Advantages of a PCB Board [WWW Document]. URL <https://sciencing.com/advantages-pcb-board-8261204.html> (accessed 2.9.20).
- Lee, J., 2005. Intrinsic adhesion properties of poly(vinyl pyrrolidone) to pharmaceutical materials: Humidity effect. *Macromol. Biosci.* 5, 1085–1093. <https://doi.org/10.1002/mabi.200500146>
- Lee, Y.H., Kim, J.S., Noh, J., Lee, I., Kim, H.J., Choi, S., Seo, J., Jeon, S., Kim, T.S., Lee, J.Y., Choi, J.W., 2013. Wearable textile battery rechargeable by solar energy. *Nano Lett.* 13, 5753–5761. <https://doi.org/10.1021/nl403860k>
- Lewis, J., 2000. Colloidal processing of ceramics and composites. *J. Am. Ceram. Soc.* 83. <https://doi.org/10.1179/1743676111Y.0000000075>
- Lewis, J.A., Smay, J.E., Stuecker, J., Cesarano, J., 2006. Direct ink writing of three-dimensional ceramic structures. *J. Am. Ceram. Soc.* 89, 3599–3609. <https://doi.org/10.1111/j.1551-2916.2006.01382.x>
- Li, C., Han, J., Ahn, C.H., 2007. Flexible biosensors on spirally rolled micro tube for cardiovascular in vivo monitoring. *Biosens. Bioelectron.* 22, 1988–1993. <https://doi.org/10.1016/j.bios.2006.08.043>
- Li, J., Orrego, S., Pan, J., He, P., Kang, S.H., 2019. Ultrasensitive, flexible, and low-cost nanoporous piezoresistive composites for tactile pressure sensing. *Nanoscale* 11, 2779–2786. <https://doi.org/10.1039/c8nr09959f>
- Li, N., Chen, Z., Ren, W., Li, F., Cheng, H.-M., 2012. Flexible graphene-based lithium ion batteries with ultrafast charge and discharge rates. *Proc. Natl. Acad. Sci. U. S. A.* 109, 17360–5. <https://doi.org/10.1073/pnas.1210072109>
- Li, Y.C., Tjong, S.C., Li, R.K.Y., 2011. Dielectric properties of binary polyvinylidene fluoride/barium titanate nanocomposites and their nanographite doped hybrids. *Express Polym. Lett.* 5, 526–534. <https://doi.org/10.3144/expresspolymlett.2011.51>
- Liu, R., Pai, C.-S., Martinez, E., 1999. Interconnect technology trend for microelectronics.
- Liu, W., Liu, N., Yue, Y., Rao, J., Cheng, F., Su, J., Liu, Z., Gao, Y., 2018. Piezoresistive Pressure Sensor Based on Synergistical Innerconnect Polyvinyl Alcohol Nanowires/Wrinkled Graphene Film. *Small* 14. <https://doi.org/10.1002/sml.201704149>
- Liu, Y., Pharr, M., Salvatore, G.A., 2017. Lab-on-Skin: A Review of Flexible and

- Stretchable Electronics for Wearable Health Monitoring. *ACS Nano* 11, 9614–9635. <https://doi.org/10.1021/acsnano.7b04898>
- López-Naranjo, E.J., González-Ortiz, L.J., Apátiga, L.M., Rivera-Muñoz, E.M., Manzano-Ramírez, A., 2016. Transparent Electrodes: A Review of the Use of Carbon-Based Nanomaterials. *J. Nanomater.* <https://doi.org/10.1155/2016/4928365>
- Lungenschmied, C., Dennler, G., Neugebauer, H., Sariciftci, S.N., Glatthaar, M., Meyer, T., Meyer, A., 2007. Flexible, long-lived, large-area, organic solar cells. *Sol. Energy Mater. Sol. Cells* 91, 379–384. <https://doi.org/10.1016/j.solmat.2006.10.013>
- Luo, S., Yang, J., Song, X., Zhou, X., Yu, L., Sun, T., Yu, C., Huang, D., Du, C., Wei, D., 2018. Tunable-Sensitivity flexible pressure sensor based on graphene transparent electrode. *Solid. State. Electron.* 145, 29–33. <https://doi.org/10.1016/j.sse.2018.04.003>
- M'Barki, A., Bocquet, L., Stevenson, A., 2017. Linking Rheology and Printability for Dense and Strong Ceramics by Direct Ink Writing. *Sci. Rep.* <https://doi.org/10.1038/s41598-017-06115-0>
- MacGill, M., 2017. What should my heart rate be? [WWW Document]. URL <https://www.medicalnewstoday.com/articles/235710.php> (accessed 10.11.19).
- Mahmoud, W.E., El-Lawindy, A.M.Y., El Eraki, M.H., Hassan, H.H., 2007. Butadiene acrylonitrile rubber loaded fast extrusion furnace black as a compressive strain and pressure sensors. *Sensors Actuators, A Phys.* 136, 229–233. <https://doi.org/10.1016/j.sna.2006.11.017>
- Mannoor, M.S., Tao, H., Clayton, J.D., Sengupta, A., Kaplan, D.L., Naik, R.R., Verma, N., Omenetto, F.G., McAlpine, M.C., 2012. Graphene-based wireless bacteria detection on tooth enamel. *Nat. Commun.* 3. <https://doi.org/10.1038/ncomms1767>
- Mannsfeld, S.C.B., Tee, B.C.-K., Stoltenberg, R.M., Chen, C.V.H.-H., Barman, S., Muir, B.V.O., Sokolov, A.N., Reese, C., Bao, Z., 2010. Highly sensitive flexible pressure sensors with microstructured rubber dielectric layers. *Nat. Mater.* 9, 859–64. <https://doi.org/10.1038/nmat2834>
- Matchawet, S., Kaesaman, A., Bomlai, P., Nakason, C., 2016. Electrical, dielectric, and dynamic mechanical properties of conductive carbon black/epoxidized natural rubber composites. *J. Compos. Mater.* 50, 2191–2202. <https://doi.org/10.1177/0021998315602941>
- Mayer, P., Magno, M., Benini, L., 2019. Self-Sustaining Acoustic Sensor With Programmable Pattern Recognition for Underwater Monitoring. *IEEE Trans. Instrum. Meas.* 1–10. <https://doi.org/10.1109/tim.2018.2890187>
- McAlpine, M.C., Ahmad, H., Wang, D., Heath, J.R., 2007. Highly ordered nanowire arrays on plastic substrates for ultrasensitive flexible chemical sensors. *Nat. Mater.* 6, 379–384. <https://doi.org/10.1038/nmat1891>
- Melzer, M., Mönch, J.I., Makarov, D., Zabala, Y., Bermúdez, G.S.C., Karnaushenko, D., Baunack, S., Bahr, F., Yan, C., Kaltenbrunner, M., Schmidt, O.G., 2015. Wearable magnetic field sensors for flexible electronics. *Adv. Mater.* 27, 1274–1280. <https://doi.org/10.1002/adma.201405027>
- Mendes, P.R. de S., Alicke, A.A., Thompson, R.L., 2014. Parallel-plate Geometry Correction for Transient Rheometric Experiments. *Appl. Rheol.* 24.
- Mewis, J. & Wagner, N.J., 2012. *Colloidal Suspension Rheology*. Cambridge Univ Press.
- Michelle M. Schaper, R.D.T. & K.A.D.-O., 1994. Respiratory responses of mice exposed to thermal decomposition products from polymers heated at and above workplace processing temperatures. *Am. Ind. Hyg. Assoc. J.* 55, 924–934. <https://doi.org/10.1080/15428119491018420>
- Middleton, W.S., 2018. The Effect of Athletic Training on the Heart. *Am. Phys. Educ.*

- Rev. 20, 148–163. <https://doi.org/10.1080/23267224.1915.10651454>
- Miorandi, D., Sicari, S., De Pellegrini, F., Chlamtac, I., 2012. Internet of things: Vision, applications and research challenges. *Ad Hoc Networks* 10, 1497–1516. <https://doi.org/10.1016/j.adhoc.2012.02.016>
- Mitrakos, V., Macintyre, L., Denison, F., Hands, P., Desmulliez, M., 2017. Design, Manufacture and Testing of Capacitive Pressure Sensors for Low-Pressure Measurement Ranges. *Micromachines* 8, 41. <https://doi.org/10.3390/mi8020041>
- Mitsubayashi, K., Wakabayashi, Y., Tanimoto, S., Murotomi, D., Endo, T., 2003. Optical-transparent and flexible glucose sensor with ITO electrode. *Biosens. Bioelectron.* 19, 67–71. [https://doi.org/10.1016/S0956-5663\(03\)00130-1](https://doi.org/10.1016/S0956-5663(03)00130-1)
- Mojarad, N., Gobrecht, J., Ekinici, Y., 2015. Beyond EUV lithography: A comparative study of efficient photoresists' performance. *Sci. Rep.* 5, 1–7. <https://doi.org/10.1038/srep09235>
- Mortara, L., Hughes, J., Ramsundar, P.S., Livesey, F., Probert, D.R., 2009. Proposed classification scheme for direct writing technologies. *Rapid Prototyp. J.* 15, 299–309. <https://doi.org/10.1108/13552540910979811>
- Moser, Y., Gijs, M.A.M., 2007. Miniaturised flexible temperature sensor. *TRANSDUCERS EUROSENSORS '07 - 4th Int. Conf. Solid-State Sensors, Actuators Microsystems* 16, 2279–2282. <https://doi.org/10.1109/SENSOR.2007.4300624>
- Mu, Q., Yang, L., Davis, J.C., Vankayala, R., Hwang, K.C., Zhao, J., Yan, B., 2010. Biocompatibility of polymer grafted core/shell iron/carbon nanoparticles. *Biomaterials* 31, 5083–5090. <https://doi.org/10.1016/j.biomaterials.2010.03.020>
- Muhammad, H.B., Recchiuto, C., Oddo, C.M., Beccai, L., Anthony, C.J., Adams, M.J., Carrozza, M.C., Ward, M.C.L., 2011. A capacitive tactile sensor array for surface texture discrimination. *Microelectron. Eng.* 88, 1811–1813. <https://doi.org/10.1016/j.mee.2011.01.045>
- Nakamura, T., Inoue, Y., Kim, D., Matsuhisa, N., Yokota, T., Sekitani, T., Someya, T., Sekino, M., 2014. Basic characteristics of implantable flexible pressure sensor for wireless readout using MRI. *Conf. Proc. ... Annu. Int. Conf. IEEE Eng. Med. Biol. Soc. IEEE Eng. Med. Biol. Soc. Annu. Conf. 2014*, 2338–2341. <https://doi.org/10.1109/EMBC.2014.6944089>
- Nan, C.-W., Shen, Y., Ma, J., 2010. Physical Properties of Composites Near Percolation. *Annu. Rev. Mater. Res.* 40, 131–151. <https://doi.org/10.1146/annurev-matsci-070909-104529>
- Nanodomains, I.L., Wang, Y., Xing, C., Guan, J., Li, Y., 2017. Towards Flexible Dielectric Materials with High Dielectric Constant and Low Loss: PVDF Nanocomposites with both Homogenously Dispersed. <https://doi.org/10.3390/polym9110562>
- Nanto, H., Yokoi, Y., Mukai, T., Fujioka, J., Kusano, E., Kinbara, A., Douguchi, Y., 2000. Novel gas sensor using polymer-film-coated quartz resonator for environmental monitoring. *Mater. Sci. Eng. C* 12, 43–48. [https://doi.org/10.1016/S0928-4931\(00\)00156-9](https://doi.org/10.1016/S0928-4931(00)00156-9)
- Nichols, W.W., 2005. Clinical measurement of arterial stiffness obtained from noninvasive pressure waveforms. *Am. J. Hypertens.* 18, 3–10. <https://doi.org/10.1016/j.amjhyper.2004.10.009>
- Nobel Media AB, 2000. The Nobel Prize in Chemistry 2000 [WWW Document]. NobelPrize.org. URL <https://www.nobelprize.org/prizes/chemistry/2000/press-release> (accessed 7.3.19).
- Nokes, L.; Jennings, D.; Flint, T.; Turton, B., 1995. *Introduction to Medical Electronics Applications*.
- Oberdörster, G., Oberdörster, E., Oberdörster, J., 2005. Nanotoxicology: An emerging

- discipline evolving from studies of ultrafine particles. *Environ. Health Perspect.* <https://doi.org/10.1289/ehp.7339>
- Oesterle, A., 2017. Pipette Cookbook. SUTTER INSTRUMENT. <https://doi.org/10.1002/ejoc.201200111>
- Oh, J., Kim, Jin-Oh, Kim, Y., Choi, H.B., Yang, J.C., Lee, S., Pyatykh, M., Kim, Jung, Sim, J.Y., Park, S., 2019. Highly Uniform and Low Hysteresis Piezoresistive Pressure Sensors Based on Chemical Grafting of Polypyrrole on Elastomer Template with Uniform Pore Size. *Small* 1901744. <https://doi.org/10.1002/sml.201901744>
- Orloff, J., 1996. Fundamental limits to imaging resolution for focused ion beams. *J. Vac. Sci. Technol. B Microelectron. Nanom. Struct.* 14, 3759. <https://doi.org/10.1116/1.588663>
- Oser, H., Marvin, R.S., 1963. Effect of Molecular Weight on Viscoelastic Properties of Polymers as Predicted by a Molecular Theory. *J. Res. Natl. Bur. Stand. Math. Math. Phys.* 67.
- Pacurari, M., Lowe, K., Tchounwou, P.B., Kafoury, R., 2016. A review on the respiratory system toxicity of carbon nanoparticles. *Int. J. Environ. Res. Public Health.* <https://doi.org/10.3390/ijerph13030325>
- Park, J.-U., Hardy, M., Kang, S.J., Barton, K., Adair, K., Mukhopadhyay, D. kishore, Lee, C.Y., Strano, M.S., Alleyne, A.G., Georgiadis, J.G., Ferreira, P.M., Rogers, J.A., 2007. High-resolution electrohydrodynamic jet printing. *Nat. Mater.* 6, 782–789. <https://doi.org/10.1038/nmat1974>
- Park, J., Kim, J., Hong, J., Lee, H., Lee, Y., Cho, S., Kim, S.W., Kim, J.J., Kim, S.Y., Ko, H., 2018. Tailoring force sensitivity and selectivity by microstructure engineering of multidirectional electronic skins. *NPG Asia Mater.* 10, 163–176. <https://doi.org/10.1038/s41427-018-0031-8>
- Peng, S., Blanloeuil, P., Wu, S., Wang, C.H., 2018. Rational Design of Ultrasensitive Pressure Sensors by Tailoring Microscopic Features. *Adv. Mater. Interfaces.* <https://doi.org/10.1002/admi.201800403>
- Persano, L., Dagdeviren, C., Su, Y., Zhang, Y., Girardo, S., Pisignano, D., Huang, Y., Rogers, J. a, 2013. High performance piezoelectric devices based on aligned arrays of nanofibers of poly(vinylidene fluoride-co-trifluoroethylene). *Nat. Commun.* 4, 1633. <https://doi.org/10.1038/ncomms2639>
- Prentice, J.C., Pizer, S.D., 2007. Delayed access to health care and mortality. *Health Serv. Res.* 42, 644–662. <https://doi.org/10.1111/j.1475-6773.2006.00626.x>
- Pu, X., Liu, M., Chen, X., Sun, J., Du, C., Zhang, Y., Zhai, J., Hu, W., Zhong, †, Wang, L., 2017. Ultrastretchable, transparent triboelectric nanogenerator as electronic skin for biomechanical energy harvesting and tactile sensing. *Sci. Adv.* 3.
- Rashidi, B., Fung, C., Vu, T., 2014. RecDroid: A Resource Access Permission Control Portal and Recommendation Service for Smartphone Users. *Association for Computing Machinery (ACM)*, pp. 13–18. <https://doi.org/10.1145/2646584.2646586>
- Rogers, J.A., 2015. Electronics for the Human Body. *Jama* 313, 561. <https://doi.org/10.1001/jama.2014.17915>
- Roh, J.H., Lee, J.H., 2018. Distal radial approach through the anatomical snuff box for coronary angiography and percutaneous coronary intervention. *Korean Circ. J.* 48, 1131–1134. <https://doi.org/10.4070/kcj.2018.0293>
- Roland, C.M., 2011. Viscoelastic Behaviour of Rubbery Materials 332.
- Roser, M., 2019. Life Expectancy [WWW Document]. Our World Data. URL <https://ourworldindata.org/life-expectancy>
- Ruth, S.R.A., Beker, L., Tran, H., Feig, V.R., Matsuhisa, N., Bao, Z., 2019. Rational Design of Capacitive Pressure Sensors Based on Pyramidal Microstructures for

- Specialized Monitoring of Biosignals. *Adv. Funct. Mater.* 1903100. <https://doi.org/10.1002/adfm.201903100>
- Ryu, S., Lee, P., Chou, J.B., Xu, R., Zhao, R., Hart, A.J., Kim, S.G., 2015. Extremely Elastic Wearable Carbon Nanotube Fiber Strain Sensor for Monitoring of Human Motion. *ACS Nano* 9, 5929–5936. <https://doi.org/10.1021/acsnano.5b00599>
- Samsung, 2019. Samsung Galaxy Fold [WWW Document]. URL <https://www.samsung.com/uk/smartphones/galaxy-fold/> (accessed 7.3.19).
- Savino J.A., L.R., 2019. Hospital and Healthcare Transformation over Last Few Decades, in: *The Modern Hospital*. Springer, Cham. https://doi.org/https://doi.org/10.1007/978-3-030-01394-3_3
- Schneider, F., Fellner, T., Wilde, J., Wallrabe, U., 2008. Mechanical properties of silicones for MEMS, in: *Journal of Micromechanics and Microengineering*. <https://doi.org/10.1088/0960-1317/18/6/065008>
- Schoch RB, Han J, R.P., 2008. Transport phenomena in nanofluidics. *Rev Mod Phys* 80:839.
- Selimis, A., Mironov, V., Farsari, M., 2015. Direct laser writing: Principles and materials for scaffold 3D printing. *Microelectron. Eng.* <https://doi.org/10.1016/j.mee.2014.10.001>
- Senior M., 2014. Novartis sign up for Google smart lens. *Nat. Biotechnol.*
- Shelton, J., Kumar, G.P., 2010. Comparison between Auditory and Visual Simple Reaction Times. *Neurosci. Med.* 01, 30–32. <https://doi.org/10.4236/nm.2010.11004>
- Shirinov, A. V., Schomburg, W.K., 2008. Pressure sensor from a PVDF film. *Sensors Actuators, A Phys.* 142, 48–55. <https://doi.org/10.1016/j.sna.2007.04.002>
- Shitashima, K., Maeda, Y., Koike, Y., Ohsumi, T., 2008. Natural analogue of the rise and dissolution of liquid CO₂ in the ocean. *Int. J. Greenh. Gas Control* 2, 95–104. [https://doi.org/10.1016/S1750-5836\(07\)00092-8](https://doi.org/10.1016/S1750-5836(07)00092-8)
- Shuai, X., Zhu, P., Liang, X., Hu, Y., Zhang, Y., Guo, Q., Su, H., Sun, R., Wong, C., 2016. A Highly Sensitive Flexible Capacitive Pressure Sensor with Micro-array Dielectric Layer 289–294.
- Shuai, X., Zhu, P., Zeng, W., Hu, Y., Liang, X., Zhang, Y., Sun, R., Wong, C., 2017a. Highly Sensitive Flexible Pressure Sensor Based on Silver Nanowires- Embedded Polydimethylsiloxane Electrode with Microarray Structure. <https://doi.org/10.1021/acscami.7b05753>
- Shuai, X., Zhu, P., Zeng, W., Hu, Y., Liang, X., Zhang, Y., Sun, R., Wong, C., 2017b. Highly Sensitive Flexible Pressure Sensor Based on Silver Nanowires- Embedded Polydimethylsiloxane Electrode with Microarray Structure - SUPPLEMENTARY 1–4. <https://doi.org/10.1021/acscami.7b05753>
- Siddiqui, S.W., Unwin, P.J., Xu, Z., Kresta, S.M., 2009. Colloids and Surfaces A : Physicochemical and Engineering Aspects The effect of stabilizer addition and sonication on nanoparticle agglomeration in a confined impinging jet reactor 350, 38–50. <https://doi.org/10.1016/j.colsurfa.2009.08.031>
- Sotzing, G.A., Briglin, S.M., Grubbs, R.H., Lewis, N.S., 2000. Preparation and properties of vapor detector arrays formed from poly(3,4-ethylenedioxy)thiophene-poly(styrene sulfonate)/insulating polymer composites. *Anal. Chem.* 72, 3181–3190. <https://doi.org/10.1021/ac991079x>
- Su, P.G., Wang, C.S., 2007. Novel flexible resistive-type humidity sensor. *Sensors Actuators, B Chem.* 123, 1071–1076. <https://doi.org/10.1016/j.snb.2006.11.015>
- Sugimoto, A., Ochi, H., Fujimura, S., Yoshida, A., Miyadera, T., Tsuchida, M., 2004. Flexible OLED displays using plastic substrates. *IEEE J. Sel. Top. Quantum Electron.* 10, 107–114. <https://doi.org/10.1109/JSTQE.2004.824112>
- Tabeling, P., 2005. Introduction to microfluidics. Oxford University Press.

- Tan, D., Tuncer, E., Cao, Y., Irwin, P., 2012. Nanofiller dispersion in polymer dielectrics. *Annu. Rep. - Conf. Electr. Insul. Dielectr. Phenomena*, CEIDP 2013, 916–918. <https://doi.org/10.1109/CEIDP.2012.6378930>
- Tee, B.C.K., Chortos, A., Dunn, R.R., Schwartz, G., Eason, E., Bao, Z., 2014. Tunable flexible pressure sensors using microstructured elastomer geometries for intuitive electronics. *Adv. Funct. Mater.* 24, 5427–5434. <https://doi.org/10.1002/adfm.201400712>
- Tricoli, A., Nasiri, N., De, S., 2017. Wearable and Miniaturized Sensor Technologies for Personalized and Preventive Medicine. *Adv. Funct. Mater.* 27, 1–19. <https://doi.org/10.1002/adfm.201605271>
- Tseng, H.J., Tian, W.C., Wu, W.J., 2013. Flexible PZT thin film tactile sensor for biomedical monitoring. *Sensors (Switzerland)* 13, 5478–5492. <https://doi.org/10.3390/s130505478>
- Tuncer, E., Sauers, I., James, D.R., Ellis, A.R., Pace, M., More, K.L., Sathiyamurthy, S., Woodward, J., Rondinone, A.J., 2009. Nanodielectrics for cryogenic applications. *IEEE Trans. Appl. Supercond.* 19, 2354–2358. <https://doi.org/10.1109/TASC.2009.2018198>
- Uddin, A.S.M.I., Chung, G.S., 2016. A self-powered active hydrogen sensor based on a high-performance triboelectric nanogenerator using a wrinkle-micropatterned PDMS film. *RSC Adv.* 6, 63030–63036. <https://doi.org/10.1039/c6ra07179a>
- Urban, G., Jobst, G., Keplinger, F., Aschauer, E., Tilado, O., Fasching, R., Kohl, F., 1992. Miniaturized multi-enzyme biosensors integrated with pH sensors on flexible polymer carriers for in vivo applications. *Biosens. Bioelectron.* 7, 733–739. [https://doi.org/10.1016/0956-5663\(92\)85056-G](https://doi.org/10.1016/0956-5663(92)85056-G)
- Valentine, A.D., Busbee, T.A., Boley, J.W., Raney, J.R., Chortos, A., Kotikian, A., Berrigan, J.D., Durstock, M.F., Lewis, J.A., 2017. Hybrid 3D Printing of Soft Electronics. *Adv. Mater.* 1703817, 1703817. <https://doi.org/10.1002/adma.201703817>
- Van Noort, R., 2012. The future of dental devices is digital. *Dent. Mater.* 28, 3–12. <https://doi.org/10.1016/j.dental.2011.10.014>
- Volkert, C.A., Minor, A.M., 2007. Focused Ion Beam Microscopy and Micromachining. *MRS Bull.* 32, 389–399. <https://doi.org/10.1557/mrs2007.62>
- Vrahopoulou, E.P., McHugh, A.J., 1987. Shear-thickening and structure formation in polymer solutions. *J. Nonnewton. Fluid Mech.* [https://doi.org/10.1016/0377-0257\(87\)85041-3](https://doi.org/10.1016/0377-0257(87)85041-3)
- Walker, S.B., Lewis, J.A., 2012. Reactive Silver Inks for Patterning High-Conductivity Features at Mild Temperatures 1–6. <https://doi.org/10.1021/ja209267c>
- Wang, M., Fang, D., Wang, N., Jiang, S., Nie, J., Yu, Q., Ma, G., 2014. Preparation of PVDF/PVP core-shell nanofibers mats via homogeneous electrospinning. *Polymer (Guildf)*. 55, 2188–2196. <https://doi.org/10.1016/j.polymer.2014.02.035>
- Wang, Qi, Ling, S., Liang, X., Wang, H., Lu, H., Zhang, Y., 2019. Self-Healable Multifunctional Electronic Tattoos Based on Silk and Graphene. *Adv. Funct. Mater.* 29. <https://doi.org/10.1002/adfm.201808695>
- Wang, Qingtao, Zhang, Zhonghao, Zhang, Zhao, Zhou, X., Ma, G., 2019. Facile synthesis of MXene/MnO₂ composite with high specific capacitance. *J. Solid State Electrochem.* 23, 361–365. <https://doi.org/10.1007/s10008-018-4143-4>
- Wang, S., Li, M., Wu, J., Kim, D.-H., Lu, N., Su, Y., Kang, Z., Huang, Y., Rogers, J.A., 2012. Mechanics of Epidermal Electronics. *J. Appl. Mech.* 79, 031022. <https://doi.org/10.1115/1.4005963>
- Wang, T.M., Xi, J.T., Jin, Y., 2007. A model research for prototype warp deformation in the FDM process. *Int. J. Adv. Manuf. Technol.* 33, 1087–1096. <https://doi.org/10.1007/s00170-006-0556-9>

- Wang, X., Liu, Z., Zhang, T., 2017. Flexible Sensing Electronics for Wearable/Attachable Health Monitoring. *Small*. <https://doi.org/10.1002/sml.201602790>
- Wang, Y.R., Zheng, J.M., Ren, G.Y., Zhang, P.H., Xu, C., 2011. A flexible piezoelectric force sensor based on PVDF fabrics. *Smart Mater. Struct.* 20. <https://doi.org/10.1088/0964-1726/20/4/045009>
- Wang, Z.L., Chen, J., Lin, L., 2015. Progress in triboelectric nanogenerators as a new energy technology and self-powered sensors. *Energy Environ. Sci.* 8, 2250–2282. <https://doi.org/10.1039/c5ee01532d>
- Webster, J.G., 1978. *Medical Instrumentation-Application and Design*.
- Wei, W., Simaan, N., 2012. Modeling, Force Sensing, and Control of Flexible Cannulas for Microstent Delivery. *J. Dyn. Syst. Meas. Control* 134, 041004. <https://doi.org/10.1115/1.4006080>
- Whitesides, G.M., 2006. The origins and the future of microfluidics. *Nature* 442, 368–73. <https://doi.org/10.1038/nature05058>
- Williams, E.D., Ayres, R.U., Heller, M., 2002. The 1.7 kilogram microchip: Energy and material use in the production of semiconductor devices. *Environ. Sci. Technol.* 36, 5504–5510. <https://doi.org/10.1021/es025643o>
- Wolff, S., Wang, M.-J., 1993. Carbon Black Filler Reinforcement of Elastomers. *Carbon Black Sci. Technol.* 460.
- Woo, S.-J., Kong, J.-H., Kim, D.-G., Kim, J.-M., 2014. A thin all-elastomeric capacitive pressure sensor array based on micro-contact printed elastic conductors. *J. Mater. Chem. C* 2, 4415–4422. <https://doi.org/10.1039/C4TC00392F>
- World PCB Production in 2014 Estimated at \$60.2B [WWW Document], 2015. URL <http://www.icconnect007.com/index.php/article/92973/world-pcb-production-in-2014-estimated-at-602b/92976/?skin=pcb> (accessed 12.1.17).
- Xu, J.X.J., Wong, M., Wong, C.P., 2004. Super high dielectric constant carbon black-filled polymer composites as integral capacitor dielectrics. 2004 Proceedings. 54th Electron. Components Technol. Conf. (IEEE Cat. No.04CH37546) 1, 536–541. <https://doi.org/10.1109/ECTC.2004.1319391>
- Yamada, T., Hayamizu, Y., Yamamoto, Y., Yomogida, Y., Izadi-Najafabadi, A., Futaba, D.N., Hata, K., 2011. A stretchable carbon nanotube strain sensor for human-motion detection. *Nat. Nanotechnol.* 6, 296–301. <https://doi.org/10.1038/nnano.2011.36>
- Yang, J., Wei, D., Tang, L., Song, X., Luo, W., Chu, J., Gao, T., Shi, H., Du, C., 2015. Wearable temperature sensor based on graphene nanowalls. *RSC Adv.* 5, 25609–25615. <https://doi.org/10.1039/C5RA00871A>
- Yang, J.C., Kim, J.-O., Oh, J., Kwon, S.Y., Sim, J.Y., Kim, D.W., Choi, H.B., Park, S., 2019. Microstructured Porous Pyramid-Based Ultrahigh Sensitive Pressure Sensor Insensitive to Strain and Temperature. *ACS Appl. Mater. Interfaces* 11, 19472–19480. <https://doi.org/10.1021/acsami.9b03261>
- Yao, N., 2007. *Focused ion beam systems: basics and applications*. Cambridge University Press.
- Yeo, W.H., Kim, Y.S., Lee, J., Ameen, A., Shi, L., Li, M., Wang, S., Ma, R., Jin, S.H., Kang, Z., Huang, Y., Rogers, J.A., 2013. Multifunctional epidermal electronics printed directly onto the skin. *Adv. Mater.* 25, 2773–2778. <https://doi.org/10.1002/adma.201204426>
- Yeong, W.-Y., Chua, C.-K., Leong, K.-F., Chandrasekaran, M., 2004. Rapid prototyping in tissue engineering: challenges and potential. *Trends Biotechnol.* 22, 643–652. <https://doi.org/10.1016/j.tibtech.2004.10.004>
- Ying, M., Bonifas, A.P., Lu, N., Su, Y., Li, R., Cheng, H., Ameen, A., Huang, Y., Rogers, J.A., 2012. Silicon nanomembranes for fingertip electronics.

- Nanotechnology 23. <https://doi.org/10.1088/0957-4484/23/34/344004>
- Yu, H., Cheng, C., Wu, P., Li, S., 2017. Elastic Capacitive Tactile Array Pressure Sensor System 29, 885–895.
- Zanella, A., Bui, N., Castellani, A., Vangelista, L., Zorzi, M., 2014. Internet of things for smart cities. *IEEE Internet Things J.* 1, 22–32. <https://doi.org/10.1109/JIOT.2014.2306328>
- Zhai, Y., Lados, D.A., Lagoy, J.L., 2014. Additive Manufacturing: Making imagination the major Limitation. *JOM* 66, 808–816. <https://doi.org/10.1007/s11837-014-0886-2>
- Zhang, W., Sun, W., Xiao, W., Zhong, X., Wu, C., Guo, W., 2019. Numerical Simulation Analysis of Microstructure of Dielectric Layers in Capacitive Pressure Sensors. *IEEE Sens. J.* 19, 3260–3266. <https://doi.org/10.1109/JSEN.2019.2893336>
- Zhang, Y., Fang, Y., Li, J., Zhou, Q., Xiao, Y., Zhang, K., Luo, B., Zhou, J., Hu, B., 2017. Dual-Mode Electronic Skin with Integrated Tactile Sensing and Visualized Injury Warning. *ACS Appl. Mater. Interfaces* 9, 37493–37500. <https://doi.org/10.1021/acsami.7b13016>
- Zhuo, B., Chen, S., Zhao, M., Guo, X., 2017. High Sensitivity Flexible Capacitive Pressure Sensor Using Polydimethylsiloxane Elastomer Dielectric Layer Micro-Structured by 3-D Printed Mold. *IEEE J. Electron Devices Soc.* 5, 219–223. <https://doi.org/10.1109/JEDS.2017.2683558>
- Zitting, A., Savolainen, H., 1980. Effects of Single and Repeated Exposures to Thermo-Oxidative Degradation Products of Poly(Acrylonitrile-Butadiene-Styrene) (ABS) on Rat Lung, Liver, Kidney, and Brain. *Arch. Toxicol* 46, 295–304.